X-RAY EMISSION FROM INSTABILITY-GENERATED SHOCKS IN DYNAMICAL MODELS OF HOT-STAR WINDS

by

R. Glenn Cooper

A dissertation submitted to the Faculty of the University of Delaware in partial fulfillment of the requirements for the degree of Doctor of Philosophy in Physics

Summer 1994

© 1994 R. Glenn Cooper
All Rights Reserved

X-RAY EMISSION FROM INSTABILITY-GENERATED SHOCKS IN DYNAMICAL MODELS OF HOT-STAR WINDS

by

R. Glenn Cooper

Approved: ______________________________

James B. Mehl, Ph.D.
Chair of the Department of Physics and Astronomy

Approved: ______________________________

Carol E. Hoffecker, Ph.D.
Associate Provost for Graduate Studies

I certify that I have read this dissertation and that in my opinion it meets the academic and professional standard required by the University as a dissertation for the degree of Doctor of Philosophy.

Signed: ______________________________

Stanley P. Owocki, Ph.D.
Professor in charge of dissertation

I certify that I have read this dissertation and that in my opinion it meets the academic and professional standard required by the University as a dissertation for the degree of Doctor of Philosophy.

Signed: ______________________________

Joseph P. Cassinelli, Ph.D.
Member of dissertation committee

I certify that I have read this dissertation and that in my opinion it meets the academic and professional standard required by the University as a dissertation for the degree of Doctor of Philosophy.

Signed: ______________________________

James MacDonald, Ph.D.
Member of dissertation committee

I certify that I have read this dissertation and that in my opinion it meets the academic and professional standard required by the University as a dissertation for the degree of Doctor of Philosophy.

Signed: ______________________________

Dermott J. Mullan, Ph.D.
Member of dissertation committee

I certify that I have read this dissertation and that in my opinion it meets the academic and professional standard required by the University as a dissertation for the degree of Doctor of Philosophy.

Signed: ______________________________

David Seckel, Ph.D.
Member of dissertation committee

TABLE OF CONTENTS

LIST OF FIGURES

LIST OF TABLES

ABSTRACT

The radiatively-driven winds of massive stars have been known for fifteen years to emit large fluxes of X-rays, but the mechanisms and even the locations of X-ray emission remain uncertain. Because these winds are known to be unstable on both theoretical and observational grounds, the most likely source of X-rays is wind material heated by the shocks that result from this instability. However, testing this hypothesis requires a model of the amount of hot material in the wind, of emission from that material, and of the attenuation by overlying wind material. To date, models of X-ray emission have assumed the existence of shocks with specified characteristics, while models of the wind driving force and wind instabilities have treated the wind as isothermal. I have developed a more comprehensive model that treats both the development of shocks and the resulting X-ray emission within a single framework. This model extends the time-dependent dynamical models of Owocki, Castor, and Rybicki (1988) to include energy balance, in order to study the hot, X-ray emitting regions. It incorporates the current version of the thermal emission code of J. Raymond (Raymond and Smith 1977) to calculate radiative energy losses, and to calculate the X-ray spectrum emitted by the hot regions shown in the wind model. Finally, the model makes simple estimates of X-ray attenuation within the wind, using X-ray cross sections from Morrison and McCammon (1983).

I have modeled X-ray emission in a high density wind from a massive star such as that of ζ Pup (O4(n)f) and in a low density wind typical of a main sequence star such as τ Sco (B0 V) or μ Col (O9.5 V). In general, the instability of the wind line force generates many shocks, but only a small fraction of these are strong enough to heat shocked material to X-ray emitting temperatures. The modeled X-ray luminosity L_{x} can easily match, or even exceed, the observed value for the high density wind, since the emission measure inferred from observation is a small fraction of the entire wind. However, the observed L_{x} for the less dense winds of later-type main sequence stars is so high that a substantial fraction of the entire wind must be hot; this does not occur in the models unless the base of the wind undergoes large (25%) fluctuations in density or another parameter.

In this dissertation, I describe the development and testing of the model; in particular, I discuss difficulties that arise in trying to resolve the hot postshock cooling regions well, and

approaches I have chosen to get around this difficulty. I give results for models of low density winds and of high density winds, and compare model spectra to the observed spectra of τ Sco, μ Col, and ζ Pup.

Chapter 1

INTRODUCTION

Although the hottest (types O and B) stars are rare, they provide a significant fraction of the luminosity of the galaxy. They also play an important—in some areas, dominant—role in determining the structure and composition of the interstellar medium (Abbott 1982b; Miller and Cox 1993; Castor 1993). The stars' radiation fields heat and ionize their surroundings, and the stars have massive stellar winds which transport large fluxes of kinetic energy, momentum, and material into the ISM.

Studying the winds can be important in another way: they can serve as laboratories to test theories of fluid and plasma flow for other types of object, such as in protostellar jets, massive X-ray binaries, and quasars. Because O and B stars are so bright, and because some can be found relatively nearby, it is possible to obtain very high-resolution spectra over a wide range of wavelengths, which can test theories in ways that are not possible for more distant or more obscured objects.

I have developed models of X-ray production in hot star winds. X-ray observations of a number of hot stars are available, and X-ray spectra are available for a few. As I shall describe in this chapter, the most likely source of the X-rays appears to be shocks in the stellar winds. To date, models of X-ray emission by such shocks have fallen into two groups: a number of papers have *assumed* shocks with various characteristics, and calculated the spectra that would result; while dynamical models of how the shocks form have assumed an isothermal wind, and thus have not addressed the question of X-ray emission. My goal is to combine these two approaches. I have extended the model described in Owocki, Castor, and Rybicki (1988, hereafter OCR) to include energy balance, improve the resolution of shock-heated regions, and calculate the X-ray spectrum emitted by the modeled temperature and density structure. I have compared spectra predicted by the model with observed spectra for two types of hot stars.

In this chapter I will sketch the observational evidence that provides information about the various characteristics of hot star winds, and will describe some of the theoretical models proposed to explain these characteristics.

1.1 A Brief History

1.1.1 Evidence for Winds in Hot Stars

Early-type stars have been known for over 25 years (Morton 1967) to have extensive winds. Observations at radio, infrared, optical, ultraviolet, and X-ray wavelengths all provide evidence of dense winds.

The most direct evidence comes from the "P Cygni" spectral line profiles observed for some ultraviolet resonance lines in the spectra of hot stars. A P Cygni line shows an absorption trough on the blue side from wind material in the line of sight moving toward the observer, and an emission peak toward the red side from material surrounding the star and moving away from the observer or transverse to the line of sight.

Asymmetric P Cygni profiles appear in optical lines, but these lines are typically of subordinate transitions, and therefore the lines originate in the highest-density, lowest-lying part of the wind. As a result, the absorption component extends only to relatively low velocity, typically less than the escape velocity.

Much broader P Cygni profiles are seen in ultraviolet resonance lines of C, N, O, and other elements. Since resonance lines arise from the ground state, the population of absorbers is very large, and the profile can be observed out to high velocities, far out in the wind. The velocity of the blue edge of the absorption part of the profile provides an estimate of the wind terminal velocity. Also, by fitting model profiles (and making assumptions about abundances and ionization fractions), the same observations can provide estimates of mass loss rates. These lines were first observed from sounding rockets (Morton 1967), and later from satellites such as *Copernicus* (Snow and Morton 1976) and the *International Ultraviolet Explorer* (Howarth and Prinja 1989, and references therein).

At radio wavelengths, hot star winds are optically thick out to tens or hundreds of stellar radii, so that the area of the emitting surface is much larger than that of the photosphere. The result is greatly enhanced thermal continuum radio emission, which can provide a measure of the star's mass loss rate. (See, *e.g.,* Bieging, Abbott, and Churchwell 1989.)

Similarly, the infrared continua of hot stars show enhanced emission (an "infrared excess"), also a direct result of the larger effective photosphere (Castor and Simon 1983; Abbott, Telesco, and

Wolff 1984). However, results from infrared measurements suffer from several types of uncertainty, and thus have so far been most useful as a consistency check for observations in other wavelength ranges and for models, rather than as a means of directly obtaining mass loss rates.

The first X-ray observations of O and B stars also showed the influence of extensive winds. This was a surprise at the time, and will be discussed further in Section 1.1.4 below.

The radio and infrared observations show that hot stars lose mass to their winds at a prodigious rate. A typical O star loses on the order of 10^{-6} solar masses per year, escaping the star at velocities as high as $v_\infty \sim 3000$ km/s or more (Prinja, Barlow, and Howarth 1990). In contrast, the sun loses only about 10^{-14} $\dot{M}$/year to the solar wind, with a terminal velocity $v_\infty \sim (400 - 700)$ km/sec.

So the most obvious question raised by the existence of such dense winds is, what physical mechanism or mechanisms can accelerate this very large amount of mass to such high velocities?

1.1.2 The Physics of Driving Hot Star Winds

1.1.2.1 Steady-state models

This question has now been answered with a fair degree of confidence: the wind material is driven by radiation pressure from the very luminous O and B stars. Electron scattering of continuum radiation makes a considerable contribution, as much as 20% to 50% of the gravitational force. The remaining force required to reach escape velocity and beyond comes from scattering in spectral lines. As a parcel of wind material accelerates, the blue edges of its spectral lines are Doppler shifted to wavelengths that have not been shadowed by underlying material, so that a single line can sweep over a significant fraction, $\sim v_\infty/c \sim 0.01$, of the spectrum. So if the wind material has on the order of 100 strong absorption and scattering lines spread across the spectrum, it can absorb a large fraction of the total momentum flux $L_{\rm bol}/c$ of the star's radiation.

This mechanism was first outlined by Lucy and Solomon (1970), and was elaborated into a comprehensive model in the classic work by Castor, Abbott, and Klein (1975, hereafter CAK).

The total force $g_{\rm line}$ due to line scattering and absorption at position r in the wind is the sum of the contributions from individual spectral lines. In spherical symmetry, the force contribution from one line with opacity κ and line center frequency ν_0 is

$$g_{\rm line}{}^1(r) = \left(\frac{2\pi\kappa v_{\rm th}}{c^2}\right)\int_{-1}^{1} d\mu\,\mu \int_{-\infty}^{\infty} dx\,\phi(x-\mu u(r))I(x,\mu,r), \tag{1.1}$$

where ϕ is the line profile function; $x = (\nu - \nu_0)/\Delta\nu_{\rm D}$ is the frequency, measured from line center in units of the Doppler width $\Delta\nu_{\rm D} = \nu_0 v_{\rm th}/c$; $u(r) = v(r)/v_{\rm th}$ is the velocity in units of the thermal speed $v_{\rm th}$; and $I(x,\mu,r)$ is the specific intensity at frequency x, in a direction making an angle $\cos^{-1}\mu$ with the radial direction, at radial position r.

To perform this integral numerically for each of thousands of spectral lines, at every radial grid point in the wind and at every frequency grid point, for each time step, would require prohibitive amounts of computer time. Current methods used to calculate the line force follow the approach developed by CAK and by Abbott (1982a), who observed that the contributions from an extensive list of spectral lines can be represented by a power-law number distribution function $N(\kappa,\nu)$, where

$$dN(\kappa,\nu) \propto \kappa^{\alpha-2} d\kappa\, d\nu, \tag{1.2}$$

with $0<\alpha<1$. This method takes somewhat different forms in the steady-state models that use modified versions of the original CAK method, and in the time-dependent models used by OCR and in this work. I will describe these different forms below.

1.1.3 The CAK Method

Current steady-state models of hot star winds use modified versions of the model developed by CAK; see Cassinelli 1979 for an excellent description. These models use the approximation first made by Sobolev (1960), who pointed out that in an outflow with monotonically increasing velocity, the size of the region in which a photon can be resonantly scattered by a given line is characterized by a length now called the Sobolev length $L_{\rm Sob} \equiv v_{\rm th}/(dv/dr)$. For the highly supersonic winds found in hot stars, this means that radiative transfer in the wind is essentially local: photons scattered in one part of the wind can normally interact only with nearby parts of the wind, since the same spectral line at other locations is Doppler shifted many thermal widths away from the emitted frequency.

As shown by Lucy (1971) and Castor (1974a), this approximation simplifies Eq. 1.1 for the force due to a single line to

$$g_{\rm line} = \kappa \frac{\pi F_\nu}{c} \Delta\nu_{\rm D} \frac{[1-\exp(-\tau_{\rm Sob})]}{\tau_{\rm Sob}}, \tag{1.3}$$

where the Sobolev optical depth $\tau_{\rm Sob}$ is $\tau_{\rm Sob} = \kappa\rho v_{\rm th}/(dv/dr)$. This expression may be further simplified for a weak line to

$$g_{\rm line} \simeq \kappa \frac{\pi F_\nu}{c} \Delta\nu_{\rm D}, \quad \tau_{\rm Sob} \ll 1, \tag{1.4}$$

and for a strong line to

$$g_{\rm line} \simeq \frac{\pi F_\nu}{c} \frac{\Delta\nu_{\rm D}}{\rho v_{\rm th}} \frac{dv}{dr}, \quad \tau_{\rm Sob} \gg 1. \tag{1.5}$$

The last expression is independent of the line opacity κ, so the total force from all strong lines depends only on the *number* of strong lines.

To find the total line force resulting from all spectral lines would require evaluating Eq. 1.3 for each of the 10^5 or more lines that can contribute significantly to $g_{\rm line}$. Rather than sum the contribution of each line individually, CAK fit the total to a power law. Defining an effective column depth per unit line strength $t \equiv \sigma_e \tau_L / \kappa_L$, where σ_e is the electron scattering opacity, τ_L is the line optical depth, and κ_L is the line opacity, the total radiation force per unit mass $g_{\rm rad}$ may be expressed as the force due only to continuum (electron scattering) opacity, times a "force multiplier" $M(t)$:

$$g_{\rm rad} = \frac{\sigma_e F_*}{c} M(t), \tag{1.6}$$

where F_* is the total stellar flux. The power law of Eq. 1.2 leads to the form

$$M(t) = kt^{-\alpha} \tag{1.7}$$

for the force multiplier.

CAK estimated values for the parameters k and α using lines of C III as representative of all driving lines. Abbott (1982a) compiled an extensive set of atomic parameters, and found values of k and α for a grid of stellar parameters. He found that the line list also depends on the ratio n_e/W, where n_e is the electron density and W the dilution factor (Mihalas 1978, p. 120), so that the above equation becomes

$$M(t) = kt^{-\alpha} \left(\frac{n_e}{W}\right)^{\delta} \tag{1.8}$$

The initial CAK model has since been revised and improved, first in a series of papers by Abbott (1978, 1980, 1982a) and others (Friend and MacGregor 1984; Friend and Abbott 1986), and subsequently by the Munich group (Pauldrach, Puls, and Kudritzki 1986; Pauldrach 1987; Kudritzki *et al.* 1989; Kudritzki and Hummer 1990; Pauldrach *et al.* 1994).

The extended CAK model is remarkably successful at explaining global characteristics of hot star winds. Model values for the terminal velocity and mass-loss rate agree quite well with observed values for stars over a wide range of spectral types, and model line profiles can reproduce many features of the observed profiles.

1.1.3.1 Instability of the Line Force

Lucy and Solomon (1970) had already suggested that the line-driving mechanism is unstable to small perturbations. The wind is very optically thick in the driving lines, and the steady-state solution has a velocity profile that increases monotonically outward from the star. Thus for a particular parcel of wind material, the driving force comes primarily from photons within about a thermal width of the blue edge of each spectral line, since longer-wavelength photons are shadowed by the (slower-moving) underlying wind material. If the parcel is perturbed to slightly higher velocity, the blue edge shifts to slightly shorter wavelengths in the frame of the star, where it sees more unshadowed photons—accelerating the parcel more, so the line profile shifts farther, and so on.

A few years after the original CAK model was published, work by MacGregor, Hartmann, and Raymond (1979) and by Carlberg (1980) confirmed and quantified this instability. However, an analysis by Abbott (1980) came to the opposite conclusion: that the line-driving mechanism should be stable to perturbations.

Owocki and Rybicki (1984) showed that the two conclusions were both potentially correct, but they applied to different length scales: the line force is stable to perturbations with scales longer than the Sobolev length, but highly unstable to shorter-wavelength perturbations, with such a perturbation potentially growing by 100 e-folds. A series of subsequent papers (Owocki and Rybicki 1985, 1986, 1991; Rybicki, Owocki, and Castor 1990) extended this analysis to three dimensions, and to include scattering and other effects; these modify the growth rate of the instability, but leave the central conclusion unchanged.

Two important modifications to this instability can arise from the scattered radiation field. In general, the net dynamical effect of the scattered radiation on the gross wind properties should be small compared to the effect of the direct stellar radiation, because the scattered field is approximately fore-aft symmetric, so the forces from the forward and backward scattered radiation cancel. However, since the scattered radiation has an intensity comparable to the direct radiation, any asymmetry in the scattered radiation (as seen by a parcel of gas in the wind) can in principle create a significant net force. Such a *fore-aft asymmetry* in the scattered radiation field can exert a strong influence on the growth of instabilities in the wind, even when the time-averaged wind properties are little affected.

This asymmetry can have two important effects: a “line drag” force and a viscous force.

Lucy (1984) described the line drag effect, which is caused by the slight asymmetry in the radiation field as seen in the reference frame of a small velocity perturbation. (Thus, this effect is present even if the scattered radiation itself has perfect fore-aft symmetry.)

Consider a parcel of gas whose velocity is perturbed to a slightly higher velocity than that of the surrounding wind. In the absence of the line drag effect, such a perturbation will grow, because the driving spectral lines of the atoms in the parcel are blueshifted an extra amount and can scatter (or absorb) additional photons from the direct stellar radiation, unshadowed by the underlying wind. However, in the frame of the perturbed parcel, scattered radiation incident from higher in the wind will be slightly blueshifted, and scattered radiation traveling outward from lower in the wind will be slightly redshifted. Therefore the scattered radiation exerts a net *drag* force on the parcel, transferring more momentum in the downward direction than in the outward direction.

The Lucy drag effect is most important near the star, where the net force from the direct stellar radiation is reduced by the star's finite disk. Owocki and Rybicki (1985) found that the drag effect can completely cancel the instability of the direct radiation force at the base of the wind. Farther from the star, the direct photons become more nearly radial and the scattered radiation field becomes less intense because of spherical expansion, so that the drag effect is less important: for example, by $r = 1.5R_*$, the instability growth rate is half that of the very large rate in a pure absorption case, so that a perturbation can still grow by 50 e-folds.

The "radiative viscosity" effect (Owocki and Zank 1991) is caused by an asymmetry in the velocity gradients above and below a given point. The probability that a photon will escape the wind varies with the velocity gradient dv/dr, so an asymmetry in this gradient will result in an asymmetry in the scattered radiation field. The net force from the scattered field thus depends on the difference in velocity gradients, *i.e.,* on the second derivative of the velocity. This is just the scaling of a viscous force $g_{\rm vis} = \nu(d^2v/dr^2)$. In this case, the viscosity coefficient can be shown (Owocki 1994) to be $\nu \sim L_{\rm Sob}v$, where $L_{\rm Sob} \equiv v_{\rm th}/(dv/dr)$ is the Sobolev length.

The asymmetry in dv/dr is largest near the sonic point, where the wind changes from a state close to hydrostatic equilibrium (small dv/dr) to the very strong driving (large dv/dr) of the wind's acceleration zone. Poe, Owocki, and Castor (1990) showed that the presence of a viscous force term can break the degeneracy in wind solutions exhibited by pure-absorption models, and may therefore suppress the "intrinsic" (self-generating) instability seen in those models.

1.1.4 Evidence for Nonmonotonic Wind Structure

This theoretical evidence for instability fit, at least in general terms, with several pieces of observational evidence that the steady-state, monotonic CAK solution was incomplete:

- The ultraviolet spectra of many stars show strong "superionized" lines of species like N VI and O VI, anomalously high ionization stages which imply wind temperatures much higher than the temperatures inferred from other lines and the continuum (Lamers and Snow 1978).

- Time series of UV lines show small "discrete absorption components" (DAC's) superimposed on the absorption part of the P Cygni profile. The DAC's move blueward (*i.e.,* accelerate) on time scales of hours to days.

- Line profiles are often nearly black (*i.e.,* have effectively zero intensity) "over a substantial interval of wavelength" (Castor and Lamers 1979). A P Cygni profile from a monotonically expanding wind is black only at the blue edge, since photons at longer wavelengths can be scattered back into the line of sight by wind material outside the absorbing column.

- Of greatest application to this work, significant fluxes of X-rays were observed from hot stars. I discuss this result further below.

1.1.5 Observations of X-Rays from Hot Stars

Lamers and Morton (1976) accounted for the presence of superionized species in the spectrum of the O4(n)f supergiant ζ Pup with a "warm wind" model, in which the wind has an electron temperature $T_{\rm e}$ in the range $1.6 \times 10^5 < T_{\rm e} < 2.0 \times 10^5$ K, much higher than the stellar effective temperature $T_{\rm eff} \simeq 40,000$ K. Lamers and Rogerson (1978) found a similar result for τ Sco (B0 V).

On the other hand, it was also realized that the superionized species could be produced by the Auger ionization process, in which an X-ray photon is absorbed by a K-shell electron, and two electrons are ejected. Cassinelli and Olson (1979) used a "corona plus cool wind" model to estimate the X-ray flux that would be necessary to create the observed superionized species in the spectrum of ζ Pup, and predicted that stars like ζ Pup should have X-ray luminosity $L_{\rm x} \sim 10^{32}{\rm ergss}^{-1}$. (See Section 1.1.6 for further discussion of coronal models.)

The warm wind hypothesis became unnecessary when X-rays from O and B stars were detected by the *Einstein Observatory* (Harnden *et al.* 1979, Seward *et al.* 1979). X-ray emission was not predicted by the CAK model, since a steady-state CAK wind is assumed to remain near the stellar effective temperature $T_{\rm eff} \simeq 10^4$–5×10^4 K, far cooler than the roughly 10^6 K needed to produce an observable flux of X-rays. However, Cassinelli and Olson (1979) had proposed that photoionization by X-ray photons via the Auger process could explain the presence of superionized species in the wind, so the presence of X-rays was not a complete surprise.

Observations of O stars by the *Einstein* IPC detector are summarized in Chlebowski, Harnden, and Sciortino (1989), and observations of B stars in Grillo *et al.* (1992). Sciortino *et al.* (1990) find that in O stars the X-ray luminosity $L_{\rm x}$ is correlated with the bolometric luminosity $L_{\rm bol}$ and the wind kinetic energy flux $\dot{M}v_\infty{}^2$, but not very well with other stellar or wind properties such as $\dot{M}$, $T_{\rm eff}$, etc. The correlation with bolometric luminosity $L_{\rm bol}$ is given approximately by

$$L_{\rm x} \simeq 10^{-6.46} L_{\rm bol}. \tag{1.9}$$

Spectra obtained with the *Einstein* SSS detector are presented in Cassinelli (1984), Swank (1984), and Cassinelli and Swank (1985). More recently, spectra from the Broad-Band X-Ray Telescope (BBXRT) appear in Corcoran *et al.* (1993), and spectra from the ROSAT PSPC detector have appeared in Hillier *et al.* (1993) and Cassinelli *et al.* (1994). The *Einstein* spectra show evidence of spectral lines of iron and other elements.

The spectra may be approximately fit by emission from a single-temperature plasma, yielding the X-ray temperature $T_{\rm x}$ and emission measure EM. The results are $T_{\rm x} = 7 \times 10^6\,{\rm K},\ {\rm EM} = 5 \times 10^{55}\,{\rm cm}^{-3}$ for $\zeta\,$Pup (Corcoran *et al.* 1993); $T_{\rm x} = 2.3 \times 10^6\,{\rm K},\ {\rm EM} = 3 \times 10^{54}\,{\rm cm}^{-3}$ for $\mu\,$Col; and a two-temperature fit with $T_{\rm x} = 1.3 \times 10^6\,{\rm K},\ {\rm EM} = 8 \times 10^{54}\,{\rm cm}^{-3}$ and $T_{\rm x} = 8.6 \times 10^6\,{\rm K},\ {\rm EM} = 2.5 \times 10^{54}\,{\rm cm}^{-3}$ for $\tau\,$Sco (Cassinelli *et al.* 1994).

1.1.6 Models of Hot Material in Winds

Though X-rays were now known to be commonly present in hot star winds, the source of these X-rays was still not known. In this section I will summarize some previous models examining where the X-rays might originate and what the observable consequences might be.

1.1.6.1 Coronal models

By analogy to X-ray emission from cooler stars like the sun, one proposed source of X-rays in hot stars was a stellar corona, lying just above the stellar surface, and with a temperature of millions of degrees (Hearn 1975, Cassinelli and Olson 1979). A corona of the proper density and temperature could certainly produce the observed amounts of X-rays.

However, there is no independent evidence that hot stars have coronae, and the mechanisms that generate the solar corona probably are not present in hot stars. They do not have strong convection zones near the surface as the sun does, and large-scale magnetic fields have not been observed in most hot stars. Not only are heating mechanisms problematic, but the heat flux required would be far larger than is needed to keep the solar corona hot, since the density near the base of a hot star wind is orders of magnitude higher than the density in the solar corona. So a hot star corona would represent a much larger amount of thermal energy; in addition, rates for cooling processes are typically proportional to the square of the density, so such a corona would cool very rapidly.

Baade and Lucy (1987), improving on a test suggested by Nordsieck, Cassinelli, and Anderson (1981), looked for the 5303 Å Fe XIV line in ζ Pup, and did not detect it. (This is the "green line" seen in spectra of the hot solar corona.) Baade and Lucy were able to use this non-detection to set strong limits on the combination of temperature and emission measure in a corona, if it exists. The limits were strong enough that they essentially ruled out a corona as the primary source of X-rays.

Another test for coronal emission follows from the fact that, if the X-rays are emitted in a corona at the base of the wind, then the spectrum should show rather strong absorption effects from the overlying wind material. Observed spectra, in contrast, indicate relatively little absorption by the wind. In particular, the absorption edge due to the oxygen K shell has not been detected in most X-ray observations (*e.g.,* Cassinelli and Swank 1983). ROSAT observations of ζ Pup (O4(n)f) by Hillier *et al.* (1993) do not detect the edge directly. Hillier *et al.* do report evidence of attenuation by the wind, but their best-fit model shows significantly less attenuation than would be seen if the X-ray photons came from a corona and thus traveled through the entire wind. Corcoran *et al.* (1993) report detecting the oxygen absorption edge in the BBXRT spectrum of ζ Pup, but the inferred absorption column depth is again probably inconsistent with emission from a corona. This conclusion is generally confirmed by MacFarlane *et al.* (1993), who model both UV line profiles and X-ray spectra, and find that the best fit to observations of ζ Pup is obtained if X-rays originate relatively deep in the wind ($r \lesssim 2R_*$), but still well above its base.

Despite these difficulties, coronal models have not been conclusively ruled out. Waldron (1984) argued that the observed spectra available at that time did not exclude the possibility of coronal emission, when the effects of ionization of wind material by the X-rays were considered. Hillier *et al.* (1993) show a model, in which He III is assumed to recombine in the outer wind, which is consistent with coronal emission. Similarly, Corcoran *et al.* note that their estimate of the absorption column depth (and thus of the location of the X-ray emitting region) depends on the assumed ionization state of the wind. MacFarlane *et al.* (1993) find that X-ray spectra and UV line profiles modeled for coronal emission could fit observations if the mass loss rate of ζ Pup is a factor of five lower than the value deduced from radio observations.

Nevertheless, the current consensus does not support coronae as the most likely mechanism, because of the problems described above, and because of the appeal of models based on shocks in the wind.

1.1.6.2 Shock Models

In light of the theoretical results indicating that the line-driving force is unstable, Lucy and White (1980) suggested that wind material might be heated to X-ray emitting temperatures by the dissipation that limits the growth of this instability. Their model envisioned a series of periodic "blobs" radiatively driven through an ambient, non-driven component of the wind, with heating occurring at the bow shock on the leading edge of each blob. Since radiative cooling is very rapid in a dense wind, they assumed both the blobs and the ambient component to be isothermal, with the hot material confined to a thin region at each shock. By adjusting as free parameters the mass of a blob and the fraction of the wind in blobs, they found that the model could match the observed X-ray luminosity of ζ Pup (O4(n)f). For the thinner winds found in late O and B-type main sequence stars, such as τ Sco, the assumption of isothermality breaks down, so that this model could not predict the X-ray luminosity.

Lucy (1982b) adapted this model to represent a picture of *shocks*, again generated by the instability of the driving force. He assumed the shocks to be periodic at a fixed time interval. A shock occurs as faster radiatively driven material overtakes and sweeps up slower shadowed material. With some plausible assumptions about the radiative driving force and the velocity structure between shocks, the wind structure can be determined with a single free parameter ν, the velocity spacing between consecutive shocks in units of the sound speed. Lucy estimated the value of ν from physical arguments to be approximately 0.4, but found that to reproduce the observed $L_{\rm x}$ of several O stars (Long and White 1980) required $\nu \simeq 0.7$. Although the model with $\nu = 0.7$ now fit the observed total fluxes adequately, the model spectra were still too soft: the corresponding temperature of shocked material would be $T_x \sim 1 \times 10^6 K$, while the observations (Long and White 1980, Cassinelli *et al.* 1981) indicate $T_x \gtrsim 3 \times 10^6 K$. To account for this, Lucy made the additional conjecture that the wind might have a spectrum of shock strengths, with harder X-rays (*i.e.,* higher T_x) from stronger shocks. He included this idea in his shock model by adding a second free parameter ϵ, representing a (small) fraction of the wind volume in which the shocks have a larger spacing and thus are stronger; *e.g.,* for ζ Pup, Lucy used $\nu_1 = 2.1$, with a resulting postshock temperature $T_s \simeq 3.5 \times 10^6$ K. The bulk of the wind was still characterized by the original value $\nu_2 = 0.4$, with $T_s \simeq 6.8 \times 10^5$ K. Thus the adjusted model has free parameters corresponding to the strength and number of shocks in the wind. By adjusting the parameters ϵ and ν_1, Lucy obtained agreement with the observed X-ray flux and hardness ratio for τ Sco. A particularly important feature of the Lucy model (and of other shock models) is that, because the shocks propagate well out into the wind, self-absorption by the wind of soft X-ray photons is reduced, in agreement with observations—unlike coronal models, which normally predict significant absorption at energies less than 0.5 keV.

Cassinelli and Swank (1983) showed X-ray spectra for the three Orion belt stars ζ Ori A, ϵ Ori, and δ Ori A. They fit the Lucy model to the spectrum of ϵ Ori and got good agreement using $\nu_2 = 0.4$, $\nu_1 = 3.4$, with one shock in 200 having the higher value. Besides the departure from Lucy's physically estimated value $\nu = 0.4$, this has the difficulty that the strong shocks (which account for most of the X-rays) are so rare that the star "should be a variable X-ray source on hourly time scales"; Cassinelli *et al.* (1983) looked for and did not observe such variability.

Lucy (1982a) also argued that multiple scattering through a highly nonmonotonic wind can produce the broad, nearly black line profiles described in Sec. 1.1.4, providing strong evidence that these winds are in fact very nonmonotonic. For a simple version of the model with multiple scattering from N resonant layers, each optically thick, the residual intensity r_ν^N at frequency ν is

$$r_\nu^N = \begin{cases} \frac{2}{N+1} r_\nu^1 & \nu > \nu_0 \\ 1 + \frac{2N}{N+1}\left(r_\nu^1 - 1\right) & \nu < \nu_0 \end{cases} \tag{1.10}$$

where r_ν^1 is the residual intensity for a monotonic wind and ν_0 is the line center frequency. This shows that the intensity in the absorption part of the P Cygni profile (where $\nu > \nu_0$) is suppressed by multiple scattering, while the intensity in the emission part is enhanced. For ζ Pup, Lucy found that the observed profile of the N V line required $N \gtrsim 12$, and his shock model for ζ Pup predicts $N \simeq 22$.

Krolik and Raymond (1985) investigated more carefully the properties and spectrum of a shock in a hot star wind. They derived a series of analytic and approximate expressions for quantities of interest, such as the cooling column $N_{\rm cool}$. (See Eq. 3.11.) They argued that the radiation force on the shock, the spectrum emitted by the shock, and other shock properties depend on whether the shock is "optically thin" or "optically thick," with optically thick shocks having accumulated a postshock column $N > N_{\rm cool}$ behind them, while optically thin shocks have not. Numerical calculations of the structure of time-steady shocks of both types found the ionization structure, radiation force, emission spectrum of a shock of each type. In a simple model of a constant-velocity wind, they found that shocks are typically optically thick near the star and thin farther away; outside a particular radius $r_{\rm crit}$ they are too thin to cool, and move outward at approximately constant velocity.

MacFarlane and Cassinelli (1989) used a simple model of a single shock propagating outward through the wind to show that such a shock, if it occurs, can create an X-ray spectrum in reasonable agreement with the observed spectrum of τ Sco. Their model is discussed further in Sec. 2.6.3.

1.1.7 Time-dependent Dynamical Models

The CAK model assumes a smooth, monotonic, steady-state wind. Given the observational and theoretical evidence that O and B star winds are neither monotonic nor steady-state, the CAK model is remarkably successful in its predictions of mass loss rates and terminal velocities. However, despite these successes, models based on the CAK theory cannot account for the phenomena listed in Sec. 1.1.4.

To investigate the effects of the driving force instability on the wind structure, OCR developed a time-dependent numerical model of a hot star wind. This model solved the hydrodynamical equations, including a radiative force term obtained by solving the radiative transfer equation assuming a power-law distribution of line strengths, as described in Abbott (1982a). (Thus, it does not assume the purely local form of the radiation force developed by CAK, and it does not use the Sobolev approximation.) For simplicity, it assumed an isothermal wind and pure absorption lines.

OCR confirmed that the wind is highly unstable, and that the velocity and density structure become very highly structured, with many shocks and a separation into broad rarefied regions and narrow dense shells. Further developments in the model, including an approximate treatment of scattering lines, are described in Owocki (1991, 1992) and Castor (1991). The OCR model will be discussed in more detail in Sec. 2.2.2.

1.2 Goals of This Work

Do the X-rays observed from hot stars in fact come from shock-heated material in the stars' winds? This is the central question that the work described in this dissertation attempts to answer. To do so, I attempt to combine the models of X-ray emission by shocks, described in Sec. 1.1.6.2, with the time-dependent dynamical model described in Sec. 1.1.7.

Building on the OCR numerical model, this required adding energy balance to the fundamental equations to determine the temperature structure; improving the resolution of the hot postshock regions; and incorporating a calculation of the emitted X-ray spectrum. Each of these steps will be discussed in some detail.

To test the results, I have compared the model spectra to observed spectra from the *Einstein Observatory* and from ROSAT. I have concentrated on models of two types of stars: early O or supergiant B stars with dense winds, such as ζ Pup; and late O and B main sequence stars with low-density winds, such as μ Col.

Chapter 2 describes the methods used to calculate the radiative spectral line force, the hydrodynamical state of the wind, and the emitted spectrum, and shows the results of several problems used to test each of these methods. In Chapter 3 I discuss the difficulties encountered in attempting to resolve the structure of the hot postshock regions where X-ray emission occurs, and report two approaches I have used to get around this problem. Chapter 4 presents some characteristics of the wind structure seen in all or nearly all models, and examines some implications of these results for the heating of wind material, and for diagnostics such as the X-ray luminosity L_{x} and the variability of L_{x}. The results of wind models for two types of stars appear in Chapters 5 and 6. Chapter 5 shows models of the wind of a main sequence star of about type B0, such as τ Sco (B0 V) or μ Col (O9.5 V). The models include several different approaches to overcome the resolution problem described in Chapter 3; model spectra from each are compared to the observed spectra of τ Sco and μ Col. Chapter 5 shows models of the denser wind of the supergiant star ζ Pup (O4(n)f), and again compares model to observed spectra. A summary of the work described in Chapters 2 through 6 appears in Chapter 7, as well as a list of the conclusions reached in this work, and of plans for future efforts to extend it.

Chapter 2

WIND EQUATIONS AND METHOD OF SOLUTION

2.1 Fundamental Equations

In this work I assume a one-dimensional, spherically symmetric wind. The numerical code solves the conservation equations in Eulerian form: the conservation of mass density ρ,

$$\frac{\partial \rho}{\partial t} + \frac{1}{r^2}\frac{\partial\left(\rho v r^2\right)}{\partial r} = 0, \tag{2.1}$$

conservation of momentum flux density ρv,

$$\frac{\partial \rho v}{\partial t} + \frac{1}{r^2}\frac{\partial\left(\rho v^2 r^2\right)}{\partial r} = -\frac{\partial P}{\partial r} - \rho g_* + \rho g_{\mathrm{line}}, \tag{2.2}$$

and conservation of energy density ρE,

$$\frac{\partial \rho E}{\partial t} + \frac{1}{r^2}\frac{\partial\left(\rho E v r^2\right)}{\partial r} + \frac{\partial\left(P v\right)}{\partial r} = (H - C) + \rho v g_{\mathrm{line}}. \tag{2.3}$$

Here t and r are the time and radial distance coordinates, v is the radial flow speed, P is the pressure, $g_* = (1-\Gamma)GM/r^2$ is the effective stellar gravity reduced by the radiative acceleration due to electron scattering, g_{line} is the radiative acceleration due to spectral lines, $E = v^2/2 + (\gamma-1)^{-1}P/\rho$ is the total specific energy ($\gamma = 5/3$ in all models described here), and H and C are energy sources and sinks (only radiative heating and cooling are considered here).

The first equation (2.1) enforces the conservation of mass as the wind flows through the numerical grid zones, and is used (in this or an equivalent form) by all hydrodynamical models. Equations (2.2) and (2.3) include terms that are more directly tied to processes in stellar winds. These terms will be discussed further in the next two sections.

2.2 Radiative Line Force

The terms on the left side of Eq. (2.2) represent, respectively, the time derivative of the momentum flux ρv, and the change in ρv due to the advection with the wind flow of spatial variations in the momentum flux.

On the right side, the first term is the contribution from the pressure gradient $\partial P/\partial r$, while the other two terms combine the effects of gravity and of radiation. The acceleration g_{rad} due to radiation has been separated into contributions from the continuum and from spectral lines: $g_{\rm rad} = g_{\rm cont} + g_{\rm line}$.

Continuum absorption is usually negligible; continuum scattering is dominated by electron scattering

$$g_{\rm es} = \frac{\sigma_T}{c\mu m_{\rm H}} f = \frac{\sigma_{\rm T}}{c\mu m_{\rm H}} \frac{L_*}{4\pi r^2}, \tag{2.4}$$

where $\sigma_{\rm T} = 6.65 \times 10^{-25}\,{\rm cm}^2$ is the Thomson cross section for the electron. Since $g_{\rm es}$ scales as $1/r^2$, just as the stellar gravity $g = GM/r^2$ does, these two terms can be combined into an "effective gravity" term g_*, as used in Eq. (2.2):

$$g_* \equiv g - g_{\rm es} = (1 - \Gamma)g, \tag{2.5}$$

where $\Gamma \equiv g_{\rm es}/g = L/L_{\rm Eddington}$.

The remaining part of the radiative acceleration is the contribution from line absorption and line scattering. Because of the very large number of lines that contribute, calculating this term is the most difficult task in modeling winds of hot stars. I will summarize several approaches to this calculation in the next sections.

2.2.1 The CAK method

In their pioneering work Castor, Abbott, and Klein (1975, CAK) used the Sobolev approximation (Sobolev 1960) for a smooth, supersonically expanding atmosphere. In this approximation, photons of a given frequency will find atoms with a particular line Doppler shifted into resonance with the photons only over a Sobolev length $L_{\rm Sob} \equiv v_{\rm th}/(dv/dr)$. Also, CAK represented the large number of spectral lines by a power law distribution of line strengths (see Section 1.1.3).

With these key simplifications, the wind momentum equation may be converted to a form that may be solved semi-analytically, with analytic expressions for the mass loss rate $\dot{M}$, terminal velocity v_∞, and line force $g_{\rm line}$. For the "point star" case of purely radial stellar radiation, the CAK line force depends on the luminosity L_*, density ρ, and velocity gradient dv/dr (Kudritzki and Hummer 1990):

$$g_{\rm CAK} \sim k \frac{L_*}{r^2} \left(\rho^{-1} \frac{dv}{dr} \right)^\alpha \tag{2.6}$$

Thus the line force depends only on the local quantities r, ρ, and dv/dr. This expression may be modified to account for the effect of changes with distance of ionization in the wind (Abbott 1982a), and to account for the finite disk of the star (Pauldrach, Puls, and Kudritzki 1986; Friend and Abbott 1986).

2.2.2 The OCR method

As Chapter 1 discussed further, the CAK method (with its later improvements) has been extremely successful at calculating mean properties of stellar winds like $\dot{M}$ and v_∞. However, the Sobolev approximation does not permit the growth of instabilities in the wind (Abbott 1980), because the wind is unstable only to perturbations with length scales shorter than the Sobolev length (Owocki and Rybicki 1984). So a model to study the nature of such instabilities requires a different method for calculating the line force.

To calculate the full radiative transfer for a large number of lines, at each of a large number of points in the wind, at each of many successive time steps, would require an impractical amount of computer time. Instead, Owocki, Castor, and Rybicki (1988, OCR) used the CAK approximation of a power-law distribution of line strengths, in the form

$$N(\kappa) = \frac{1}{\kappa_0}\left(\frac{\kappa}{\kappa_0}\right)^{\alpha-2} e^{-\kappa/\kappa_{\max}}, \tag{2.7}$$

but *without* making the Sobolev approximation, to derive a nonlocal radiation force that depends on the (time-dependent) structure of the wind.

The cutoff opacity $\kappa_{\max}$ was introduced to prevent numerical instability that can occur when the force due to the high-opacity tail of the distribution grows without limit. In a real wind, there is some maximum κ above which no lines exist, so it seems reasonable to cut off the distribution above this point for the numerical model. However, the line force instability has proven to be so strong that even lower choices of $\kappa_{\max}$ are necessary in practice. For models of low density winds (Chapter 5), we usually use $\kappa_{\max} = \kappa_0$. For models of high density winds (Chapter 6), the greater density means that $\kappa_{\max}$ must be set lower; we use $\kappa_{\max} = 10^{-2}\kappa_0$, or even $\kappa_{\max} = 10^{-3}\kappa_0$.

The original OCR technique assumed all lines to be pure absorption lines, and thus did not consider the dynamical effect of the scattered radiation field. The justification for this is that, in a smooth, supersonic flow, the scattered field will have approximate fore-aft symmetry (Sobolev 1960), so that most of the net driving force comes from the initial absorption of the direct stellar radiation. With this assumption, the line radiation force per unit mass is (Owocki 1991)

$$g_{\rm dir}(r) = \frac{g_{{\rm thin},\kappa_o}\Gamma(\alpha)}{\kappa_o^\alpha}\int_{-\infty}^{\infty} dx\, \phi(x - v(r)/v_{\rm th})\eta^{-\alpha}(x,r), \tag{2.8}$$

where $x = (\nu - \nu_o)/\Delta\nu_{\rm D}$ is the frequency displacement from line center in units of the thermal width $\Delta\nu_{\rm D} \equiv \nu_0 v_{\rm th}/c$, $\phi(x)$ is the line profile function, the force in the optically thin limit is

$$g_{{\rm thin},\kappa} \equiv \frac{L_* \kappa v_{\rm th}}{4\pi r^2 c^2}, \tag{2.9}$$

and the profile-weighted mass column depth (*i.e.,* optical depth per unit line strength κ) is

$$\eta(x,r) = \frac{\tau(x,r)}{\kappa} = \int_{r_{min}}^{r} dr'\,\rho(r')\phi(x - v(r')/v_{\rm th}). \tag{2.10}$$

The equation in this form applies only to the case of radially streaming photons. This may easily be extended to include an integral over the possible photon arrival directions: see Eq. 2.20.

At each time step, the numerical code first calculates values of $\eta(x,r)$ for each frequency grid point, at each radial grid point. (Only a small number of frequency points need to be updated for each step, since at each radial point r, only photons within a few Doppler widths $\Delta\nu_{\rm D}$ of the comoving-frame line center frequency $(\nu_0)_{\rm CMF} = \nu_0(1 + v(r)/c)$ can be scattered.) With $\eta(x,r)$ known, solving for $g_{\rm dir}(r)$ is then straightforward.

OCR found that this pure-absorption form of the radiation line force results in a wind model whose gross characteristics, such as v_∞ and $\dot{M}$, are similar to the corresponding CAK model. However, unlike the CAK models, the OCR model is highly unstable to the growth of small perturbations, as predicted by the analyses of MacGregor, Hartmann, and Raymond (1979) and Owocki and Rybicki (1984). Fig. 2.1 shows an example. In addition, the model is *intrinsically* unstable: structure develops and grows even in the absence of externally-introduced perturbations, as shown in Fig. 2.2.

2.2.3 The SSF (Smooth Source Function) method

2.2.3.1 Motivation

The approximate fore-aft symmetry of the scattered radiation field means that, in the supersonic part of the wind, the effect of scattered radiation on the mean flow of the wind is small compared to that of the direct (unscattered) radiation from the star (Lucy 1971, Castor 1974b). However, Lucy (1984) showed that the scattered radiation field is *not* symmetric as seen by a perturbed parcel of wind material with velocity above or below the mean flow speed at that radius, and as a result the scattered radiation tends to damp the growth of velocity perturbations in the wind.

Examining this issue further, Owocki and Rybicki (1985) confirmed that the scattered radiation slows the growth of velocity perturbations compared to the pure-absorption case. However, they showed that this effect can completely cancel the instability of the direct radiation force only at the base of the wind, and only if one ignores limb darkening. Higher in the wind, the growth rate increases rapidly—to more than 50% of the (very high) rate for pure absorption by $r = 2R_*$.

Figure 2.1: Structure in a pure absorption (OCR) wind model.

Figure 2.2: Self-excited nature of some pure absorption models.

This suggests that a hot star wind will remain unstable, but that the growth of instabilities can be strongly affected by the scattered as well as the direct radiation. Unfortunately, to incorporate full radiative transfer of the scattered photons in many driving lines at each time step remains impractical with current computers, as it would require at least a hundredfold increase in CPU time over the pure-absorption model, which itself requires on the order of half an hour on a Cray C90. But it is important to find some way to include the dynamical effects of the scattered field in a numerical model, even if the full transfer problem cannot be solved. Owocki (1991, 1992, 1994) has developed a "Smooth Source Function" (SSF) method, which calculates an approximation to the net force from the scattered radiation, while using only about 20% more computer time. I use this method in all the models described in this dissertation, except for test models that use the CAK force.

2.2.3.2 Basic equations

From a formal solution of the radiative transfer equation, the diffuse (scattered) part of the specific intensity at frequency x has the form

$$I_{\text{diff}}(x, \mu, r) = \int S(r')e^{-|t-t'|}dt' \tag{2.11}$$

where the integration is away from the local point at radius r and along a ray that makes an angle $\cos^{-1}\mu$ with the outward radial direction. The optical depths are functions of frequency as well as depth,

$$t = t(x, \mu, r) \tag{2.12}$$

and

$$t' = t(x, \mu, r'), \tag{2.13}$$

but the source function S is typically a function only of radius; for example, for a pure-scattering line with complete frequency and angle redistribution,

$$S(r') = \bar{J}(r'), \tag{2.14}$$

the intensity averaged over both angle and frequency.

The key assumption in the SSF method is that, since the source function is in this sense an averaged quantity, $S(r')$ is relatively insensitive to dynamical variations in wind parameters such as the velocity v, compared to the optical depth $t(x, \mu, r)$. So the source function $S(r')$ may be approximated as

$$S(r') \approx S_o(r), \tag{2.15}$$

where the "smooth" source function $S_o(r)$ is to be determined by one of several approaches described below.

With this approximation, the source function may be taken out of the integral in the formal solution of Eq. (2.11), with the result

$$I_{\rm diff}(x,\mu,r) = S_o \left(1 - e^{-\Delta t(x,\mu,r)}\right) , \tag{2.16}$$

where the optical depths along a forward-pointing (+) or backward-pointing (−) ray are

$$\Delta t = \Delta t_+(x, +|\mu|, r) = \int_{r_{\rm min}}^{r} \kappa\rho\phi\left(x - |\mu| v(r')/v_{\rm th}\right) \frac{dr'}{|\mu|} \ ; \ \mu > 0, \tag{2.17}$$

or

$$\Delta t = \Delta t_-(-x, -|\mu|, r) = \int_{r}^{r_{\rm max}} \kappa\rho\phi\left(x + |\mu| v(r')/v_{\rm th}\right) \frac{dr'}{|\mu|} \ ; \ \mu < 0, \tag{2.18}$$

with the integral always outward: from a minimum radius r_{min} to r for a forward ray, or from r to a maximum radius r_{max} for a backward ray.

We can then calculate the flux $\bar{H}_{\rm diff}$, and from that and the direct flux $\bar{H}_{\rm dir}$ we can calculate the force

$$g_\kappa = (4\pi v_{\rm th}/c^2)\kappa\bar{H}. \tag{2.19}$$

Finally, we can integrate over a power-law distribution of line strengths as in the previous section, and integrate over angle μ. The result is (Owocki 1991)

$$g_{\rm dir}(r) = \frac{g_{{\rm thin},\kappa_o}\Gamma(\alpha)}{\kappa_o^\alpha} \int_0^1 dy \int_{-\infty}^{\infty} dx\, \phi(x - \mu_y v(r)/v_{\rm th}) \eta_+^{-\alpha}(x, \mu_y, r). \tag{2.20}$$

and

$$g_{\rm diff}(r) = g_{{\rm thin},\kappa_o} \frac{S_o r^2}{I_* {R_*}^2} \frac{\Gamma(\alpha)}{\kappa_o^\alpha} \int_0^1 dy \int_{-\infty}^{\infty} dx\, \phi(x - \mu v(r)/v_{\rm th}) \left[\eta_-^{-\alpha}(x,\mu_y,r) - \eta_+^{-\alpha}(x,\mu_y,r)\right] , \tag{2.21}$$

where $\eta_\pm(x,\mu,r) \equiv \Delta t_\pm(x,\mu,r)/\kappa$.

The integral over angle μ has been replaced here by an integral over the parameter $y \equiv (b/R_*)^2$, where b is the impact parameter made by a ray (see, *e.g.*, Mihalas 1978, pp. 252–253). We actually represent this integral by a single-ray quadrature with $y = 0.5$, which we have found gives a result for the direct force within a few percent of the full finite-disk value. For the direct force $g_{\rm dir}$ this integral extends only over the stellar disk: the range $y = 0$ to $y = 1$. For the diffuse force $g_{\rm diff}$ the integral should actually extend over all space: from $y = 0$ to $y = y_{\rm max} \equiv (r/R_*)^2$. To keep the calculation tractable, though, we consider only the range $y = [0, 1]$ for $g_{\rm diff}$ as well as for $g_{\rm dir}$. This requires rescaling the $g_{\rm diff}$ integration by a factor $y_{\rm max}$, which appears in front of the integral in Eq. 2.21.

With this approximation, the expressions for $g_{\rm diff}$ and $g_{\rm dir}$ involve nearly identical integrations over y and η. This means that, once the $\eta(x, \mu, r)$ have been calculated for the direct term as in Section 2.2.2, the diffuse term can also be calculated for only a small additional cost in computer time. So we now have a practical, though approximate, way to include the important Lucy line drag effect in stellar wind models. (See Owocki 1994 for a more detailed analysis of the line drag effect in the SSF approximation.)

2.2.3.3 Setting $S_{\rm o}(r)$

The question now is what form to use for the smooth source function. In the Sobolev approximation, for optically thin scattering (thus, for a weak line),

$$S_{\rm o} = I_* \frac{1-\mu_*}{2}, \tag{2.22}$$

where $\mu_* \equiv \sqrt{1-(R_*/r)^2}$.

In the other limit of optically thick scattering (a strong line), $S_{\rm o}$ also depends on the local velocity gradient:

$$S_{\rm o} = I_* \frac{1-\mu_*}{2} \left[\frac{1+\sigma E_3}{1+\sigma/3} \right], \tag{2.23}$$

where $\sigma \equiv d\ln v/d\ln r - 1$ and $E_3 \equiv (1+\mu_* + \mu_*^2)/3$.

If we use Eq. 2.22 to set $S_{\rm o}$, we find that the growth of instabilities is damped at the wind base as predicted. However, $S_{\rm o}$ decreases more rapidly with r than is correct, so that the growth rate increases faster than the rate calculated by Owocki and Rybicki (1985).

To use Eq. 2.23, we take a relaxed initial condition with a smoothly increasing velocity law, and calculate $S_{\rm o}(r)$ from that, and then fix those values of $S_{\rm o}(r)$ for the duration of the model. This approach makes the growth rate a bit too high at the base, and too low higher in the wind, compared to the Owocki and Rybicki (1985) rate.

The compromise that we currently use is to simply use the initial state to calculate a source function $S_{\rm o}(r)$ that will reproduce the Owocki and Rybicki (1985) growth rate, and then use that $S_{\rm o}$ for the duration of the model. The wind structure that develops in this case is qualitatively similar to the result using either of the first two approaches, though there are differences in the height at which large variations in v or r first form and in other details.

2.2.3.4 Summary: calculating the radiative force

At the start of a new time step, we evaluate the integral expressions in Eqs. (2.17) and (2.17) to find the optical depths $\Delta t_{\pm}$ at each frequency and radius grid pair (x_i, r_i); as mentioned above, only a small number of frequency points needs to be updated for each r_i. The integral is evaluated by means of a numerical quadrature in radius r; that is, by a sum over discrete radial grid points $\{r_i\}$. (In general, we need the optical depth $\Delta t_{\pm}(x, \mu, r)$ for each combination of frequency, radius, and angle; but we normally use a single-point quadrature to represent the subsequent angle integration.)

The frequency grid $\{x_i\}$ covers a range corresponding to the entire velocity range in the wind. The grid spacing is set to $\Delta x = (1/3)\Delta\nu_{\rm D}/\nu_{\rm o}$, so that the resolution is finer than the thermal width $\Delta\nu_{\rm D}$.

With the optical depths $\Delta t_{\pm}$ known (and thus the profile-weighted mass column depths $\eta_{\pm} = \Delta t_{\pm}/\kappa$), we then evaluate Eqs. (2.20) and (2.21) for the direct and diffuse force, respectively. This involves quadratures over the frequency grid $\{x_k\}$ and, if more than one ray is to be used, over rays with parameters $\{y_j\}$. This sets the term $g_{\rm line} = g_{\rm dir} + g_{\rm diff}$ to use in Eqs. (2.2) and (2.3)

2.3 Radiative Heating and Cooling

The terms on the left-hand side of Eq. 2.3 are the energy analogues of the corresponding terms in Eq. 2.2, representing, respectively, the time derivative of the energy density ρE, the advection of energy density by wind flow across the grid, and the work done by pressure gradients. The last term on the right-hand side is the work done by the radiation force $g_{\rm line}$. The only new physics appearing in Eq. 2.3 is in the heating and cooling terms H and C.

2.3.1 Heating and wind temperature

In the absence of instabilities, several authors (*e.g.,* Drew 1989, Pauldrach 1987) have found that the temperature of a hot star wind drops gradually at larger r, but typically no more than 40% or so below the stellar effective temperature $T_{\rm eff}$. Since the present models are intended only to estimate X-ray emission, I have not attempted to calculate the balance between photoionization heating and radiative and expansion cooling in the cool parts of the wind. Instead, the model simply sets a "floor" on the wind temperature $T_{\rm w}$, forcing the wind temperature to be $T_{\rm w} \geq T_{\rm eff}$. In other words, the energy source term H is set at each point and at each timestep to be $H = 0$ if the local temperature $T(r) \geq T_{\rm eff}$. If $T(r) < T_{\rm eff}$, then $H(r) = (3/2)n(r)k(T_{\rm eff} - T(r))$, the energy required to raise the temperature in that zone back to $T_{\rm eff}$.

2.3.2 Radiative cooling

To estimate the energy radiated away by hot (*e.g.,* shocked) wind material, I use a fit to an updated version of the cooling curve calculated by Raymond, Cox, and Smith (1976); the table of data used for the fit was generated by the current version of the thermal cooling code described by Raymond and Smith (1977). The function $\Lambda(T)$, the energy radiated per unit volume, per unit time, has a broad peak near $T = 2 \times 10^5 K$; then decreases approximately as $T^{-1/2}$ to about $T = 10^7 K$; and then rises again as bremsstrahlung radiation becomes the dominant process.

I assume that the wind is optically thin to this radiation: it appears as an energy loss term, but is not included in the radiative transfer. The dynamical consequences of a cooling function of this form, and problems it raises for the calculations, are described in Chapter 3.

2.4 The Hydrodynamics Code

To solve Equations (2.1–2.3) numerically, we use the VH-1 computer code, developed at the University of Virginia (Blondin 1992). This is an implementation of the piecewise parabolic method (PPM) developed by Woodward and Collela (1984; see also Collela and Woodward 1984). We have found VH-1 to be written in an exceptionally transparent style, making it easily adaptable to a wide range of applications. For example, implementing the SSF method required only the addition of one subroutine containing the force calculation, plus minor changes in the initialization, input/output, and main routines.

2.4.1 The piecewise parabolic method

PPM incorporates two main improvements over a simpler hydrocode. The first is a method first suggested by Godunov (1959), and now implemented in a variety of codes. At the beginning of each time step, each numerical zone boundary is modeled as the dividing line in a Riemann shock tube problem (see, *e.g.,* Courant and Friedrichs 1948). The state on each side of the initial discontinuity in the problem is given by the zone averages of mass, momentum, and energy on each side of the zone boundary. The shock tube problem is then solved to find the flux of each quantity across the boundary during the next time step.

The second improvement in PPM is the "piecewise parabolic" algorithm, which determines the input states for the shock tube problem more accurately by making a quadratic interpolation of the distributions of mass, momentum, and energy within each zone. The input states are then taken to be the averages over that part of the zone that can be reached by a sound wave during the length of the time step, *i.e.,* the characteristic domain of dependence.

Because of these extra calculations, PPM uses more computer time per time step than many other methods. But it is especially good at preserving steep gradients or shocks as material advects across the numerical grid, which is a difficult problem for numerical codes. A recent comparison of sixteen hydrodynamics finite differencing schemes by Yang and Przekwas (1992) finds PPM to be "excellent in overall performance," avoiding many of the limitations of other schemes. Besides the inherent desirability of maintaining as much wind structure as possible, it is particularly important for the sudden approximation method of calculating spectra (see Chapter 3) to keep the shocks as sharp and easily identified as possible.

2.4.2 The numerical grid

Most of the numerical models presented here use a discrete radial grid of 1500 or 1600 points, extending from $r = R_*$ to $r \simeq 10R_*$. Some extended models use 3000 or 3200 points, from $r = R_*$ to $r \simeq 25R_*$. This represents a compromise between the need to resolve the wind structure as well as possible in all regions, and the need to keep the computer time required to a reasonable level.

In the subsonic region near the base of the wind, the radial grid separation Δr must at least resolve the pressure scale height $H \sim (a/v_{\rm esc})R_*$, so that the (modeled) wind can adjust properly to changes propagated by sound waves. This is equivalent to requiring that the density cannot change by too large a factor from one zone to the next. Since the Sobolev length $L_{\rm Sob} \sim (v_{\rm th}/v)R_* \sim (a/v_{\rm esc})R_*$, requiring $\Delta r < H$ also ensures that perturbations with wavelengths shorter than $L_{\rm Sob}$ can be represented on the grid; this is necessary, since the line driving force is unstable only to these short-wavelength perturbations.

In the supersonic part of the wind, the goal is to resolve the wind structure as well as possible. Wind shocks themselves are much too narrow to resolve. And in general, as Chapter 3 discusses, I have not been able to properly resolve the postshock cooling regions where X-rays originate, so that alternative methods are necessary to estimate X-ray emission. Instead, I have simply tried to make sure that length scales considerably shorter than typical separations between shocks and dense shells in the wind are resolved, so that the picture of overall wind structure is as accurate as possible.

In order to resolve the subsonic and acceleration regions as well as possible, while still extending the grid out as far as possible, I use a grid spacing that increases from $\Delta r = 0.002R_*$ at the base to $\Delta r = 0.01R_*$ by $r = 9R_*$. For the extended runs, I extend the grid with a constant $\Delta r = 0.01R_*$ from $r \simeq 9R_*$ to 25 R_*, so that the grid does not become too coarse.

So while the narrowness of the postshock cooling regions (and technical problems; see Chapter 3) prevents fully resolving these regions or the dense shells that result, this gridding does make it possible to follow the evolution of shocks and other structure throughout the wind acceleration region and above.

2.4.3 Boundary conditions

The quadratic interpolation of PPM requires values from two zones on each side of a given zone, so that the boundary conditions are set in two ghost zones lying outside each boundary.

In many applications, ensuring that the model results are not unduly influenced by the choice of boundary conditions is a subtle and difficult task. For example, Hedstrom (1979) developed a procedure to set boundary conditions that preserve the Riemann invariants along characteristics across the boundary, and as a result minimize reflections from the boundary. In earlier versions of the stellar wind code, OCR implemented a version of the Hedstrom boundary conditions. They found, however, that the resulting models did not differ much from models using simpler boundary conditions. So in this work I have used simpler conditions at both the lower and upper boundaries of the modeled region.

2.4.3.1 Lower boundary $r_{\min}$

At the lower (inner) boundary, we fix the density to a constant value $\rho_{\rm LB}$; since the temperature at the wind base is assumed to be the stellar temperature $T_{\rm eff}$, this also fixes the pressure to be $P_{\rm LB} = (\rho_{\rm LB}/\mu)kT_{\rm eff}$. To determine an appropriate value for $\rho_{\rm LB}$, note that the mass loss rate $\dot{M}$ at the sonic point $r_{\rm sonic}$ ($v(r_{\rm sonic}) = a$) is determined by the stellar luminosity L_* and the line list parameters k and α. If $\rho_{\rm LB}$ is set too low, mass conservation requires the velocity $v_{\rm LB} = \dot{M}/(4\pi {r_{\min}}^2 \rho_{\rm LB})$ at the lower boundary to be already supersonic, and the wind cannot adjust itself from whatever initial state was chosen for the model. If $\rho_{\rm LB}$ is set too high, then $v_{\rm LB}$ becomes very small, $v_{\rm LB} \ll a$, and the model becomes very "stiff" near the lower boundary, because even small variations Δv result in large fractional changes in $\dot{M}$, perhaps from outflow to infall and back. Oscillations at the boundary result which persist for very long model times.

So the constraints are to choose $\rho_{\rm LB}$ so that the lower boundary is low enough to be in the subsonic part of the wind, but not so low that problems with "stiffness" arise. If $\rho_{\rm LB}$ is chosen within these limits, the model adjusts itself to a state that is nearly independent of the precise value of $\rho_{\rm LB}$. We generally choose $\rho_{\rm LB}$ to be a few percent of the density at the sonic point, which allows the model to relax away from the initial wind state relatively smoothly and quickly. With this choice, the continuum optical depth $\tau_{\text{cont}}(r_{\min}) \simeq 1$ for a supergiant wind, and $\tau_{\text{cont}}(r_{\min}) \ll 1$ for a late O or B main sequence wind.

For the profile-weighted mass column depth η_+ at the lower boundary, we impose a Schuster-Schwarzschild type boundary condition (cf. OCR), with the result

$$\eta_+(x, \mu, r_{\min}) = \frac{1}{\kappa_{\max}} + \frac{\phi(x)}{\sigma_c}, \tag{2.24}$$

where $\phi(x)$ is the line profile function and σ_c is the continuum opacity, assumed to be entirely due to electron scattering.

Finally, the boundary condition for the velocity v extrapolates the velocity gradient from the first two real zones into the ghost zones at the beginning of each time step. This allows the velocity near the wind base to vary as the model adjusts from the initial state, or in response to perturbations.

2.4.3.2 Upper boundary $r_{\max}$

Since the wind is always supersonic at the outer boundary, the choice of boundary conditions there will almost always affect at most the few zones closest to the boundary; disturbances advect off the grid before they can propagate into the rest of the wind. So we simply choose values for the ghost zones that will not be too different from those at the top of the wind.

We set the density in the ghost zones to decrease as r^{-2}, as it would in a constant-velocity wind with a constant mass loss rate. We set the pressure to the value in the last real zone, to reduce reflections off the boundary. For the velocity, we again extend the velocity gradient from the last two real zones into the ghost zones.

The existence of a diffuse radiation force means that radiation from outside the upper boundary $r_{\max}$ can affect the modeled part of the wind. To minimize the effect of such a force at the upper boundary, we set

$$\eta_-(x, \mu, r_{\max}) = \frac{1}{\kappa_{\max}} + \rho(r_{\max})\, r_{\max}\, \phi(x - \mu v(r_{\max})/v_{\text{th}}). \tag{2.25}$$

The second term is the value that $\eta_-(r_{\max})$ would have if the velocity $v(r)$ were constant for all $r > r_{\max}$, and has the effect of making η_- and η_+ nearly the same near the upper boundary $r_{\max}$. This makes the total radiative force small near the upper boundary, so that it has little effect on the structure of the wind within the modeled region.

2.5 Calculating Spectra

Calculating the X-ray spectrum that will result from a modeled state of the wind turns out to have unexpected difficulties, discussed in detail in Chapter 3. For the simplest case, when the temperature and density structure of the wind are well resolved, I can use the values of T and ρ at each point as inputs to the thermal emission code kindly provided by Dr. John Raymond. The code was first described by Raymond and Smith (1977), with further comments and some modifications described in Cox and Raymond (1985) and Raymond (1988). I use the current version as of 1993, obtained by request from Dr. Raymond.

This code considers transitions in the 13 most abundant elements resulting from many processes, including collisional and radiative excitation and deexcitation, bremsstrahlung, dielectronic recombination, (optionally) photoionization, and others. One specifies the desired output range and resolution in photon energy or wavelength, and the Raymond code calculates the power emitted per unit volume, per energy bin, for each input pair (T, ρ).

The output spectrum, in the absence of attenuation by overlying wind material, is then just the sum of the results from all grid points multiplied by appropriate volume and density factors. Wind attenuation may be included by considering the column depth lying above each grid point, and multiplying the emitted power at each photon energy by the appropriate attenuation factor; this is discussed further in Chapters 5 and 6. (I do not consider scattered or re-emitted radiation in these models.)

2.6 Test Problems

To test the accuracy and reliability of the radiation hydrodynamics computer code, I have used the code to solve test problems of several types. Here I will describe the Sod shock tube problem, which I use to test the VH-1 hydrodynamics code; simulations of oscillations due to the "global thermal instability" (Chevalier and Imamura 1982), which test the hydrocode combined with radiative cooling; and a simple fast wind-slow wind model, which tests most of the elements of the stellar wind code.

2.6.1 The Sod shock tube

This problem, which has become a standard test of hydrodynamics codes, was described by Sod (1978). It is a simple shock tube problem, in which a discontinuity is set up, and then the boundary separating the two states is removed at time $t = 0$. The initial states are: $P = 1.0, \rho = 1.0$ on the left side ($x < 0.5$); $P = 0.1, \rho = 0.125$ on the right side ($x > 0.5$); $v = 0$ everywhere. Beginning at $t = 0$, a shock wave moves to the right, and a rarefaction fan propagates to the left, both starting from the initial discontinuity. Because problems of this type are well understood (Courant and Friedrichs 1948), the modeled solution may be compared with the known correct

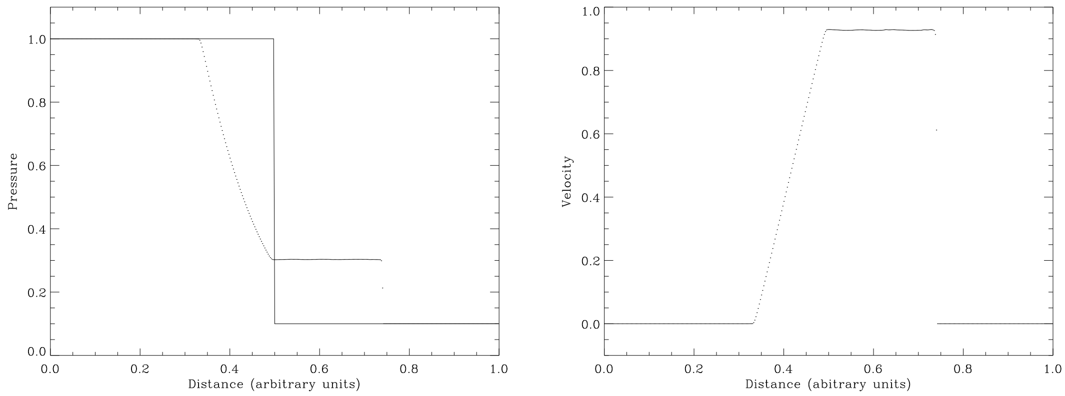

(a) Pressure states. The solid line shows the initial state. The dots show the pressure at each grid point at $t = 0.14$.

(b) Velocity. The initial state has $v = 0$ everywhere. The dots show the velocity at each grid point at $t = 0.14$.

Figure 2.3: Pressure and velocity for the Sod shock tube test problem, after a time $t = 0.14$. A rarefaction fan stretches from $x = 0.34 - 0.5$; a shock appears at $x = 0.73$.

solution. Of particular interest here is to see how well the code can preserve the shock within a small number of zones.

Figure 2.3(a) shows the solution for the pressure after 100 time steps, at the modeled time $t = 0.14$, for a model that uses a grid of 400 points over the interval [0,1]. The shape and location of the rarefaction fan and shock agree well with the exact values. The shock at $x = 0.74$ is spread over only two zones. This very steep shock structure also appears in Figure 2.3(b), showing the velocity solution for the same time. As expected, the PPM method incorporated in VH-1 excels at preserving steep shocks and other structures, with little dissipation.

2.6.2 Global thermal instability of radiating shocks

Shocks with postshock temperatures in the regime $10^5 K \lesssim T \lesssim 2 \times 10^7 K$, where the radiative cooling emissivity decreases or is nearly flat with temperature, experience a cooling instability, which causes the width of the postshock cooling region to oscillate (see Langer, Chanmujam, and Shaviv 1981; Chevalier and Imamura 1982; Gaetz, Edgar, and Chevalier 1988; and references therein). The cooling region increases in width as the shock adds hot, slowly-cooling material. But in this temperature regime, the emissivity of the material increases as it cools, and the cooling rate also grows because the density increases. As a result, the postshock region collapses to a very thin, cool, dense shell, and new material flowing through the shock then begins building up a new

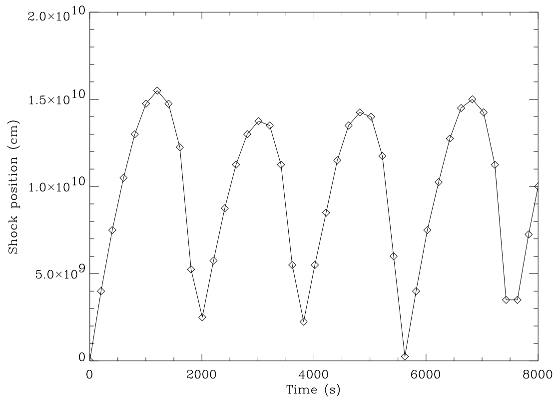

(a) Model with $\Lambda(T) \propto T^{-0.5}$. The width of the postshock cooling region (the distance of the shock from the wall) oscillates with a period approximately equal to the cooling time for material at the postshock temperature $T_\mathrm{s} \simeq 9 \times 10^6 K$.

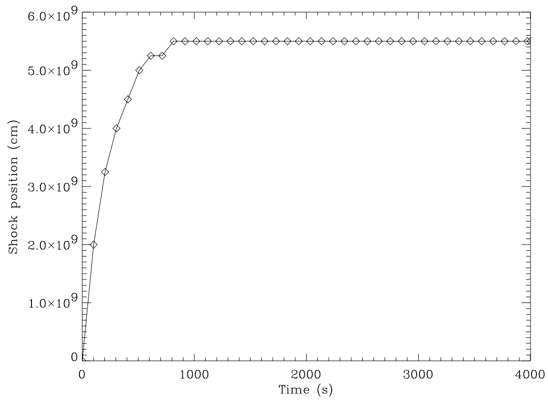

(b) Model with $\Lambda(T) \propto T^2$. The postshock cooling region grows to a steady-state value, and then remains constant as new material flows in and old material cools to join the dense shell at the wall.

Figure 2.4: Position of the shock in tests of the global thermal instability. A wall lies at $x = 0$; the diamonds show the position of the shock (*i.e.,* the width of the postshock cooling region) at each time.

hot region.

Figure 2.4(a) shows this oscillation in the location of the shock relative to the contact discontinuity. This model creates a shock by taking material with temperature $T = 3 \times 10^4$ K, flowing at velocity $v = 600$ km/s, and running it into a wall. (The "wall" is actually a reflecting boundary condition at the edge of the grid.) With a velocity jump $\Delta v = 600$ km/s, the inflow velocity in the frame of the shock is $v_0 = (4/3)\Delta v = 800$ km/s. So the postshock temperature $T_\mathrm{s} \simeq 9 \times 10^6$ K, which is in the regime where the cooling function $\Lambda(T) \propto T^{-0.5}$.

Chevalier and Imamura (1982) showed that instability occurs whenever $\alpha \lesssim +0.4$, where α is the logarithmic slope of the cooling function $\Lambda(T) = \Lambda_0 T^\alpha$. Figure 2.4(b) shows a model that is identical to the first model, except that it uses a cooling function with the form $\Lambda(T) \propto T^2$. As predicted, the width of the postshock region now reaches an equilibrium value, after which it is stable. New material flows through the shock, gets heated, cools as it moves across the cooling region, and then adds to the narrow, cool, high density layer next to the wall.

These results agree well with the model results published by Gaetz, Edgar, and Chevalier (1988).

2.6.3 Fast wind-slow wind interaction

To create a simple stellar wind model that can show some of the characteristics of wind shocks without the expense of a full model, I have used a model with an initially slow wind, created by simply cutting off the velocity of a normal wind above some value. At the start of the model (shown by the dotted line in Figure 2.5), the regular line driving force (here represented by the relatively simple CAK force) is turned on, so that a faster wind develops, and runs into the overlying slow wind. This approach is similar to that used by MacFarlane and Cassinelli (1989).

A model with radiative cooling turned off, shown by the solid line in Figure 2.5, shows clearly the shock pair that develops; similar shock pairs are observed in the solar wind (Hundhausen and Gentry 1969). A reverse shock (propagating back toward the star, in the frame of the contact discontinuity) forms where the fast wind material meets the slower, denser intershock material, at $z = 7.1R_*$. On the other side of this region, a forward shock forms at $z = 7.8R_*$ as slow wind material gets swept up and shocked to a higher velocity. Figure 2.6(a) shows a closeup of the shock region, with the value at each grid point represented by a dot. Since this model has no radiative cooling, the temperature of material between the shocks approximately shows the postshock temperature corresponding to the shock amplitude when that parcel of material went through the shock; both shock amplitudes were initially small, so the material closest to each shock is hottest.

When radiative cooling is included, as shown in Figure 2.6(b), the intershock region is much narrower, since the shocked material compresses as it cools. It is actually narrower than an analytic estimate predicts, a problem that I will discuss at greater length in the next chapter. Here, let us note once again that the modeled shocks are quite steep, so that identifying the shocks and measuring shock parameters such as the amplitude and preshock density is relatively simple.

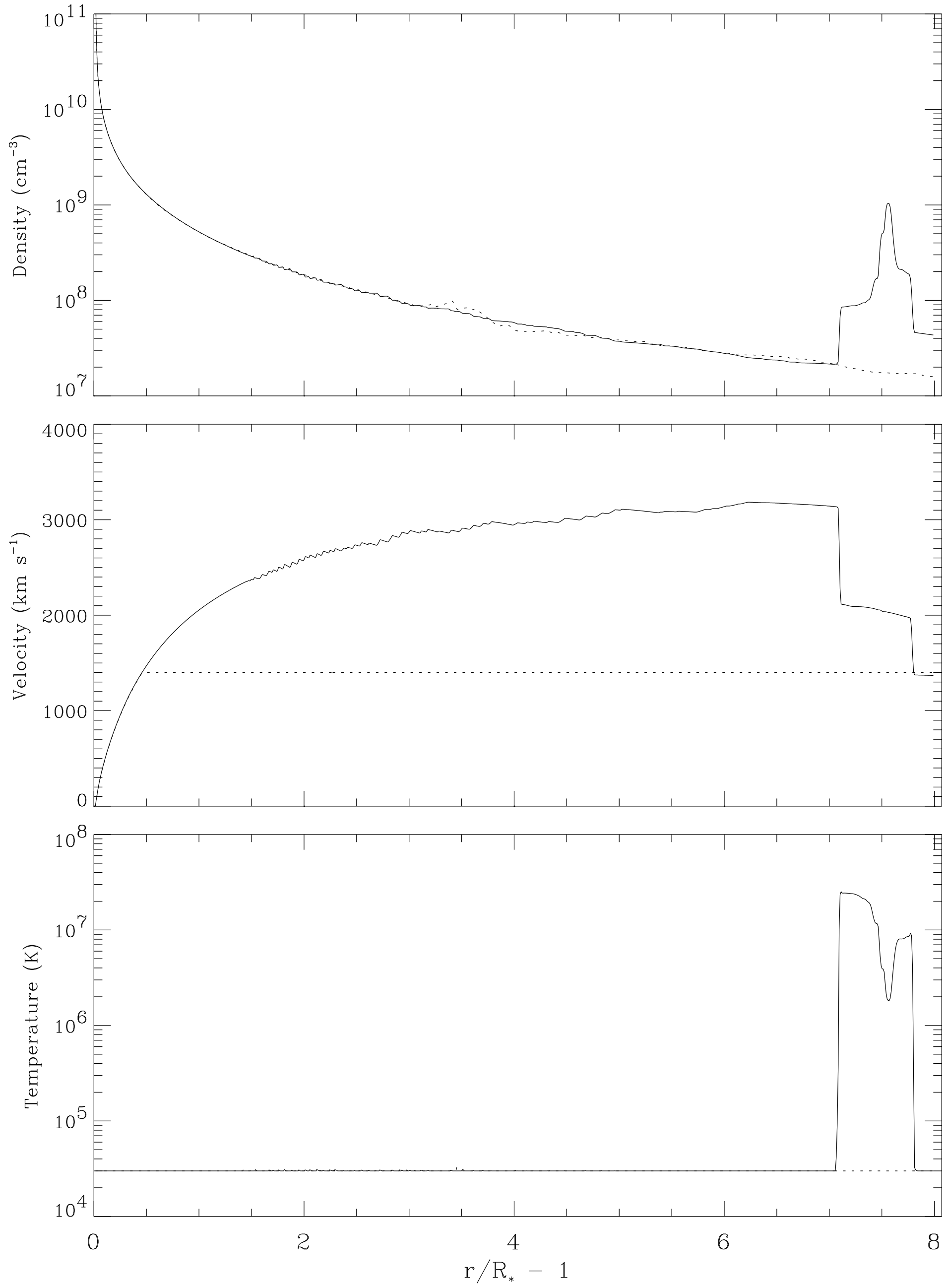

Figure 2.5: An adiabatic model of a fast wind-slow wind interaction. The dotted line shows the initial state, with the velocity cut off at $v = 1400$ km/s. The solid line shows the result after $t = 19$ ksec. A shock pair has formed, with a reverse shock at $z = 7.1R_*$ and a forward shock at $z = 7.8R_*$.

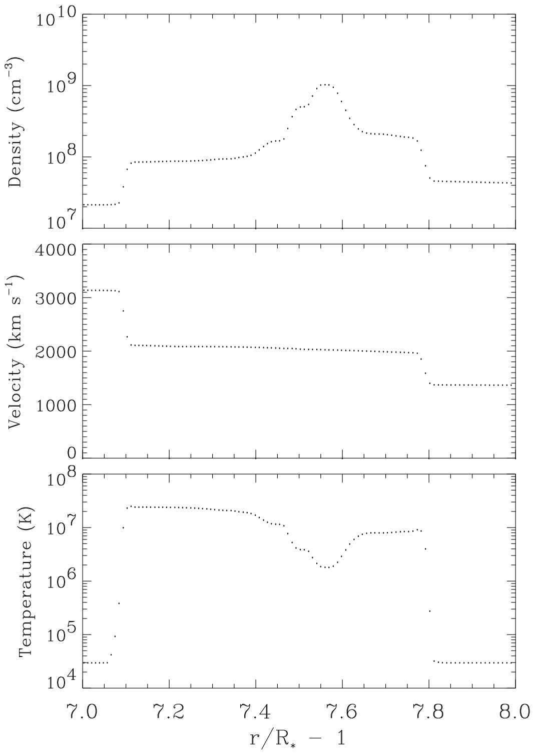

(a) Closeup of the shock pair region of Figure 2.5. Values of density, velocity, and temperature at each grid point are shown. In this adiabatic model, the cool region between shocks consists of material that went through a shock early, when the shock amplitude was small.

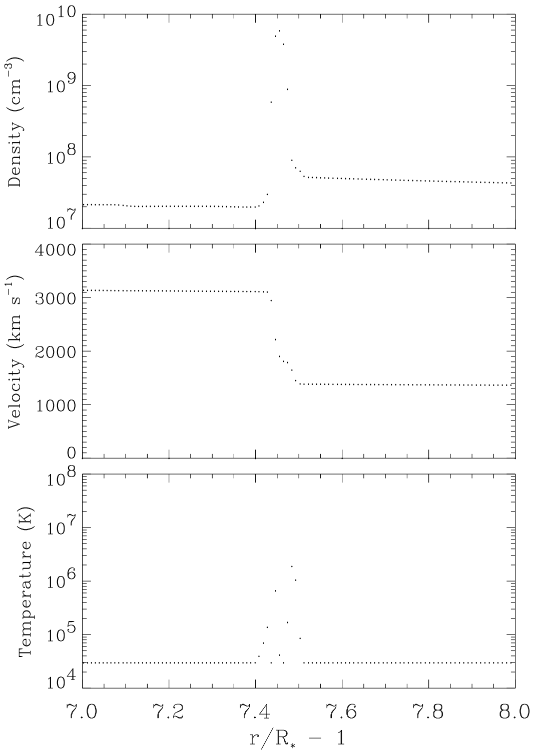

(b) The shock pair region for a model identical to that in (a), except with radiative cooling included.

Figure 2.6: The reverse and forward shocks in two models of a fast wind / slow wind interaction. Figure (a) shows an adiabatic model; (b) shows a model with the same initial state and wind parameters, but with radiative cooling added.

Chapter 3

RESOLVING SHOCK-HEATED REGIONS

3.1 Introduction

Calculating the expected X-ray flux from a wind model is, in principle, straightforward: the model supplies the temperature and density at each point in the wind; a model of thermal X-ray emission calculates the flux from each point; these fluxes can then be folded through absorption by the overlying wind material, and finally added together to get the integrated X-ray spectrum.

However, a variety of practical difficulties interfere with this simple plan. The most vexing problem encountered in this work has been the difficulty in properly resolving the temperature and density structure of the hot postshock cooling regions where X-rays originate. This difficulty arises both from certain physical properties of hot star winds and from limitations of numerical hydrodynamics codes. The next two sections discuss these constraints on resolution, and the following sections describe the approaches I have used to partially overcome them for two types of winds.

3.2 Physical Constraints

If material cools too quickly after being heated by a shock, the cooling region will be unresolvable even aside from any loss of accuracy in the numerical model, simply because the grid point spacing cannot be too fine if the modeled region is to extend a reasonable distance from the stellar surface—at least, say, several stellar radii. Since the radiative cooling rate is typically proportional to the square of the density, $\Lambda(T) \propto n^2$, cooling regions are much narrower in the dense winds of early O and supergiant OB stars than in, for example, the lower-density winds of main sequence B stars.

It is useful to consider several parameters that provide order-of-magnitude estimates of the characteristic sizes of cooling regions. I will define several such parameters below, and then examine values of these parameters that correspond to typical conditions in high- and low-density hot star winds.

3.2.1 Cooling time

A simple estimate of the time required for material to cool from the postshock temperature T_s to an equilibrium (much lower) temperature can be obtained by dividing the energy density by the radiative cooling rate:

$$t_\mathrm{cool} \sim \frac{\frac{3}{2}nkT_\mathrm{s}}{\Lambda(n, T_\mathrm{s})}, \tag{3.1}$$

where n is the number density, $k = 1.38 \times 10{-}16 \mathrm{erg\,K^{-1}}$ is the Boltzmann constant, and $\Lambda(n, T)$ is the total power radiated per unit volume. For temperatures between about $10^5\,\mathrm{K}$ and $2 \times 10^7\,\mathrm{K}$, the Raymond, Cox, and Smith (1976) cooling law has the approximate form

$$\begin{aligned} \Lambda(n, T) &= n_\mathrm{e} n_\mathrm{H} L(T) && (3.2)\\ &\simeq n_\mathrm{e} n_\mathrm{H} L_0 \left(\frac{T_0}{T}\right)^{\frac{1}{2}}. && (3.3) \end{aligned}$$

Choosing $T_0 = 10^6\,\mathrm{K}$, we find $L_0 \simeq 1.0 \times 10^{-22} \mathrm{erg\,cm^3 s^{-1}}$. So

$$\begin{aligned} t_\mathrm{cool} &\sim \frac{\frac{3}{2}nkT_\mathrm{s}}{n_\mathrm{e} n_\mathrm{H} L_0 \left(\frac{T_0}{T_\mathrm{s}}\right)^{\frac{1}{2}}} && (3.4)\\ &\sim (91\,\mathrm{ksec})\; T_6^{\frac{3}{2}}\, n_8^{-1}, && (3.5) \end{aligned}$$

where $\quad T_6 = T_\mathrm{s}/(10^6\,\mathrm{K}),\ n_8 = n/(10^8\,\mathrm{cm^{-3}})$.

This simple estimate ignores the change in the cooling rate as the material cools. Also, cooling does not proceed at constant density as the estimate assumed, since the material generally compresses as it cools; assuming constant pressure might be more accurate. However, the total time is dominated by the early part of the cooling process, when the cooling rate is lowest, so the above expression yields estimates that are within a factor of two or less of more careful calculations. In the interest of simplicity, I will use the expression in Eq. 3.5 to make order-of-magnitude estimates.

3.2.2 Cooling length

We can use this result to estimate the "cooling length": the distance from the shock to the point where material has cooled. We are interested in strong shocks, in which the shock velocity jump $\Delta v \gg a$, where a is the sound speed. The velocity v_0 of incoming material in the rest frame of a strong shock is related to Δv by $v_0 = (4/3)\Delta v$. In this frame, the velocity v_1 of outgoing material that has just passed through the shock is $v_1 = v_0/4$. So the cooling length for a strong shock may be estimated to be

$$L_\mathrm{cool} \sim t_\mathrm{cool} \left(\frac{v_0}{4}\right). \tag{3.6}$$

Since the immediate postshock temperature T_s for a strong shock is (*e.g.,* Krolik and Raymond 1985)

$$T_s \simeq 1.4 \times 10^5\,\mathrm{K} \left(\frac{v_0}{100\mathrm{kms}^{-1}}\right)^2, \tag{3.7}$$

we can combine equations 3.5, 3.6, and 3.7 to get

$$L_{\rm cool} \sim 6 \times 10^{11}\,\mathrm{cm}\; T_6^2\, n_8^{-1}\,. \tag{3.8}$$

3.2.3 Cooling column

A convenient feature of cooling regions follows from the above result that $L_{\rm cool} \propto n^{-1}$. The column depth $N_{\rm cool}$ of the cooling region is

$$N_{\rm cool}(r_{\rm shock}) = \int_{r_{\rm shock}}^{r_{\rm shock}+L_{\rm cool}} n\,dr \propto n. \tag{3.9}$$

So, for a steady-state shock (one whose parameters have not changed for a time $t \gtrsim t_{\rm cool}$), the hot postshock region will have a *constant* column depth (Krolik and Raymond 1985)

$$\begin{aligned} N_{\rm cool} &= \int n\,dr & (3.10)\\ &\simeq 7 \times 10^{17}\,\mathrm{cm}^{-2} \left(\frac{v_0}{100\mathrm{kms}^{-1}}\right)^4. & (3.11)\end{aligned}$$

3.2.4 Results for parameters of interest

In this work I will concentrate on models of winds from two types of hot stars: early O stars such as ζ Pup with massive, dense winds, and late O to early B main sequence stars such as μ Col or τ Sco with weaker, less dense winds. Typical radiative cooling lengths change from very short and difficult to resolve ($L_{\rm cool} < 0.1R_*$) to quite long (with $L_{\rm cool}$ stretching to many stellar radii, so that cooling is dominated by adiabatic expansion rather than radiation) over this range in spectral type.

The preshock density in wind models depends both on the stellar parameters and on local conditions; to indicate typical values for each type of wind, I use the average density at a point one stellar radius above the surface. The strongest shocks seen in our models usually have postshock temperatures $T_s \sim 10^7$ K; the weakest shocks that might have significant X-ray emission have $T_s \sim 10^6$ K.

Cooling times $t_{\rm cool}$ and cooling lengths $L_{\rm cool}$ for these ranges in number density n and temperature T, appear in Table 3.1 below.

It is generally not practical to make the numerical grid spacing smaller than perhaps $0.01R_*$ (Section 2.4.2). So for low density winds, good resolution—say, on the order of 100 zones in the

Table 3.1: Cooling times and lengths

Wind type	$R_*/R_\odot$	n	T	$t_{\rm cool}$	$L_{\rm cool}$
High density	19.0	$2.5 \times 10^9\,{\rm cm}^{-3}$	$10^6\,$K	$3.6 \times 10^3\,$sec	$0.02R_*$
High density	19.0	$2.5 \times 10^9\,{\rm cm}^{-3}$	$10^7\,$K	$1.1 \times 10^5\,$sec	$1.8R_*$
Low density	6.7	$2.5 \times 10^7\,{\rm cm}^{-3}$	$10^6\,$K	$3.6 \times 10^5\,$sec	$5.2R_*$
Low density	6.7	$2.5 \times 10^7\,{\rm cm}^{-3}$	$10^7\,$K	$1.1 \times 10^7\,$sec	$520R_*$

hot postshock region—should be possible in principle for all shocks strong enough to be important for X-ray emission. For high density winds, good resolution appears impossible for weaker shocks, but is possible in principle for very strong shocks. However, the next section discusses further limits on the resolution that is actually achieved by our numerical code.

3.3 Numerical Constraints

Relatively early in this work, I made estimates like those shown in Table 3.1, and, guided by arguments like those above, decided to begin with models of a low density wind. I chose parameters appropriate to τ Sco (B0 V), and calculated a few test models. As expected, the model wind was very structured, with some strong shocks. But I was surprised to find that the hot regions behind these strong shocks remained narrow, or even completely unresolved.

I discovered that the problem of resolving the cooling regions of radiating shocks is a very difficult one for numerical computer codes, for reasons that stem from the nature of finite-differencing schemes. In the following I will discuss limitations in hydrodynamical models themselves, and also a problem that arises from the interaction of the interpolations made by the differencing scheme with radiative cooling.

3.3.1 Numerical diffusion

As discussed in Section 2.4, we use an Eulerian hydrodynamics code which models the volume of interest by specifying values of the density, velocity, and pressure at discrete points in space. Any such code has difficulty following a feature that has a length scale less than the grid spacing. In particular, a shock or other steep gradient will always be spread across at least two or three grid points, because the code has to interpolate between zone-center values as the shock moves between points. Although the piecewise-parabolic method (PPM; Collela and Woodward 1984) used by our code does a better job of preserving steep gradients than most such methods, any discontinuity or near-discontinuity does experience some rounding because of this numerical "diffusion."

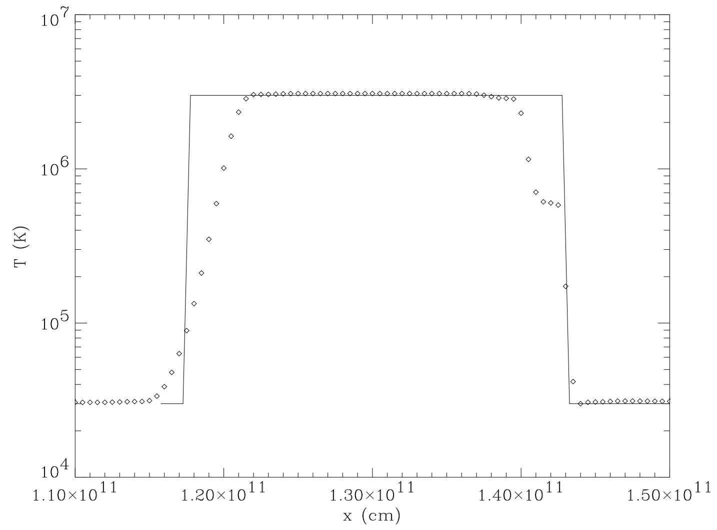

Figure 3.1: Effect of numerical interpolation scheme on a square temperature pulse, with no cooling. Solid line: original pulse shape. Diamonds: calculated temperature in each zone, after the pulse has advected five times its width.

Consider a simple model to illustrate this process. The initial state for this model is a 50-zone wide square temperature pulse, where the pulse temperature is 3×10^6 K, a factor of 100 higher than the background temperature elsewhere on the grid, and inflowing at the left boundary. The density in the pulse is $6 \times 10^7\,\mathrm{cm}^{-3}$, a factor of 100 lower than the density elsewhere, so that the pressures inside the pulse and outside are equal. Therefore there should theoretically be no expansion or compression; since this model has no radiative or other cooling, an analytic solution would simply show the unaltered pulse shape moving across the grid. Both the pulse and surrounding material have a velocity of 200 km/s.

The result appears in Figure 3.1, which shows as diamonds the zone temperature values in and near the pulse, after the pulse has advected a distance equal to five times its width across the numerical grid, at time $t \simeq 5800$ seconds. The solid line shows the initial pulse structure. Though the pulse still largely traces the original square outline, some rounding is obvious, together with small numerical ripples generated by the steep gradients at the pulse edges.

3.3.2 Radiative diffusion

In addition to this process found (in varying degrees) in all Eulerian hydrocodes, radiative cooling adds a second, synergistic effect wherever there is a steep gradient in temperature. The finite number of grid points means that the peak temperature usually does not lie exactly at the center of a zone, where model parameters are stored. In the case of a shock, the temperature and other variables jump discontinuously, or more precisely over a distance that is much shorter than any feasible grid spacing. Even in the finite differencing schemes that do best at preserving this sort of steep structure, there will always be at least one zone which includes both preshock and postshock material, so that values in the zone (and often one or two zones on each side) are interpolated between the exact preshock and postshock values. In particular, material that has just passed through the shock, and whose temperature should be T_s as given by Eq. 3.7, must always pass through such a zone or zones, in which the zone temperature value is less than T_s.

The radiative cooling rate varies as $T^{-1/2}$ for temperatures from about 2×10^5 K to 2×10^7 K (Eq. 3.3), and thus for the entire range of temperatures that are found in these winds and are important for producing X-rays. So material that should be at the high postshock temperature, but is averaged by the numerical grid to an intermediate temperature, cools faster than the rate corresponding to the postshock temperature T_s. The result is that the modeled material cools toward the background wind temperature faster than the correct cooling rate for material at the same density and at temperature T_s. This too-fast drop in temperature then steepens the temperature gradient between this point and the next, which in subsequent time steps lowers the temperature at that next grid point, and the process repeats.

To calculate radiative cooling I use an updated version of the relation shown in Raymond, Cox, and Smith (1976); the values used for the cooling function $\Lambda(T)$ were calculated using the current version of J. Raymond's thermal emission code (Raymond and Smith 1977). See Section 2.3.2 for further details.

Let us consider the model of an advecting square temperature pulse described in the previous section, with radiative cooling now added. To distinguish the effects of cooling from those of advection, I also show a third model that includes radiative cooling but keeps the pulse stationary.

Figure 3.2 illustrates the results of the stationary and advecting models with radiative cooling. Model states after about 5800 seconds (the same time as shown in Figure 3.1) are shown for each of the two models and for the initial state. This time is far less than the cooling time $t_{\rm cool} \sim 8\times10^5$ seconds in the pulse, but is approximately twice the cooling time $t_{\rm cool} \sim 2500$ seconds for the values $n = 6\times10^8\,\mathrm{K}, T = 3\times10^5\,\mathrm{K}$, intermediate between the pulse and background. Zones at the edge of the pulse take on intermediate values, cool quickly, and expose new zones; by the time shown, all of the zones in the pulse have been affected.

The solid line shows the initial pulse shape, with 50 zones at the higher temperature $3\times$

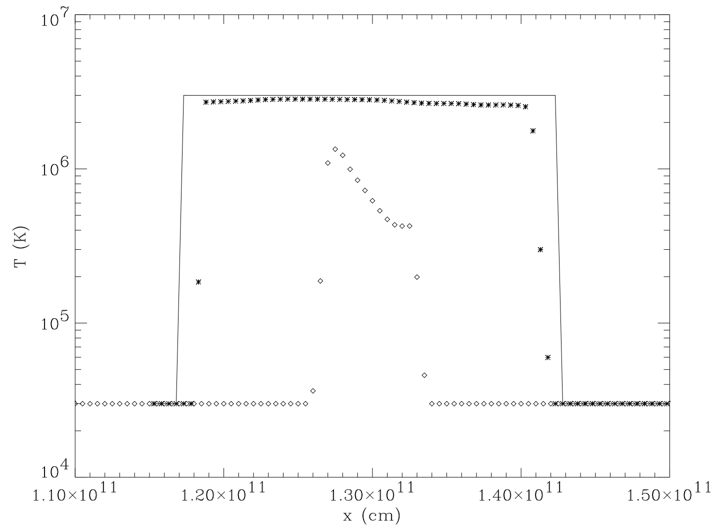

Figure 3.2: Effect of numerical interpolation scheme on a square temperature pulse, with radiative cooling included. Solid line: original pulse shape. Diamonds: calculated temperature in each zone, after the pulse has advected five times its width. Stars: calculated temperature in each zone for a stationary pulse after the same time interval, showing the effect of cooling alone, without advection.

10^6 K, as before. The asterisks show the effect of radiative cooling alone (without advection) in the stationary model. Some rounding occurs near the edges, even without motion on the grid. The pulse temperature has dropped only to 2.8×10^6 K, as we would expect since $t \ll (t_{\rm cool})_{\rm pulse}$. The diamonds show the combined effects of cooling and advection. Both the leading and trailing edge of the pulse have been eaten away by the radiative diffusion process, to the point that even the center of the pulse has begun to cool faster than in the no-advection case. The pulse of hot, low density material disappears by $t = 7000$ seconds, 1200 seconds after the time shown here.

I have not found an ideal solution to these resolution problems. However, to calculate spectra from models of the two types of stellar winds, I have used one of two approximations: adiabatic models for the low-density winds of main sequence B or late O stars, and a "sudden approximation" for the dense winds of supergiant and earlier O stars.

3.4 Adiabatic Calculations (No Radiative Cooling)

As shown in Section 3.2.4, an analytic estimate indicates From Table 3.1, in a low density wind, material hot enough to emit X-rays has a nominal radiative cooling time of 360 ksec (100 hours) or more. This is much longer than other relevant timescales: for example, a wind with a velocity of 1000 kms^{-1} moves on the order of 40 R_* in this time.

The characteristic length for the velocity to change, assuming a velocity law of the form (CAK)

$$v(r) = v_\infty \left(1 - \frac{R_*}{r}\right)^\beta \tag{3.12}$$

is

$$\begin{aligned} \frac{v}{(\frac{dv}{dr})} &= r\left(\frac{r}{R_*} - 1\right) && (3.13) \\ &= 2R_* && (3.14) \end{aligned}$$

at a height of 1 R_* ($r = 2R_*$), for $\beta = 1$.

So for hot, X-ray emitting material ($T > 10^6\,\mathrm{K}$), we may simply approximate the radiative cooling time to be infinite, and shut off radiative cooling: once material gets heated, it cools only by means of adiabatic expansion. Such an adiabatic calculation provides an approximate upper limit to the amount of hot material in the wind at a given time. It overestimates the amount of material at intermediate temperatures $T \sim$ few $\times\, 10^5\,\mathrm{K}$, where radiative cooling is strongest, but this material should have little effect on the calculated X-ray spectrum. (It will eventually affect the wind structure, however. See Sec. 5.5 for further discussion of this point.) And this approximation has the great advantage that it prevents the radiative diffusion problem described in Section 3.3.2.

With this approximation, the cooling regions behind strong shocks are well resolved, and it is possible to proceed with the direct calculation of X-ray emission from each numerical zone described in the opening sentences of this chapter. For examples of adiabatic models and the spectra calculated from them, see Chapter 3.

3.5 A Sudden Approximation for Estimating X-Ray Spectra

The estimated values in Table 3.1 indicate that most shocks in a high density wind will have short cooling lengths $L_{\mathrm{cool}} < R_*$, and often $L_{\mathrm{cool}} \ll R_*$. This makes a direct calculation impossible, and it also means that an adiabatic model would be a poor approximation in this case. But on further reflection one can see that rapid cooling, with narrow postshock cooling regions, is an *advantage*, because the cooling region rapidly reaches a steady state.

At such a steady-state shock, a steady stream of particles enters the shock and is heated to temperature T_{s}; moves away from the shock, radiating and cooling; and finally reaches the equilibrium wind temperature T_{wind}, exiting the postshock cooling region. A snapshot at one instant, if we could resolve the cooling region, would show the region to be made up of particles that went through the shock at various times up to $t_{\rm cool}$ ago, and that are therefore at various temperatures between $T_{\rm s}$ and $T_{\rm wind}$.

This space profile of $T(r)$ *vs.* r corresponds to a time profile, $T(t)$ *vs.* t, of a single particle radiatively cooling from $T_{\rm s}$ to $T_{\rm wind}$. (Here we may, to a reasonable approximation, ignore expansion cooling, since radiative cooling dominates in this case.) In other words, the total emission integrated across the postshock cooling region is the same as the emission $\dot{e_1}$ from one particle integrated over its cooling history, times the number flux of particles entering the shock:

$$\int_{L_{\rm cool}} \Lambda(x)\, dx = (\#\ {\rm in/s}) \int_{t_{\rm cool}} \dot{e_1}\, dt. \tag{3.15}$$

The number flux is just the preshock number density $n_{\rm in}$ times the shock-frame incoming velocity v_0, quantities that the numerical model can determine fairly well even though the postshock region is not resolved.

I have used this correspondence to design a "sudden approximation" method to estimate the X-ray emission spectrum from a model of a high density wind. The method assumes that the wind density is high enough that material heated by a shock cools in a time shorter than the characteristic time for the shock parameters to change significantly. The sudden approximation method also assumes that the density is high enough that a cooling column depth $N_{\rm cool}$ of material flows through the shock faster than the shock parameters change. These assumptions can hold even relatively high in the wind, where the density is lower, because the wind structure changes more slowly as the wind moves to larger r.

To implement this method, I calculated the integrated emission from a single atom as it cools from initial temperature $T_{\rm s}$ to the wind temperature $T_{\rm wind}$; since $T_{\rm wind}$ is always much less than X-ray emitting temperatures, the precise value used does not affect the calculated spectrum. I repeated the calculation for each of a set of initial temperatures spanning the range of interest, from 10^4–10^8 K. The rate $\Lambda(n,T) = n_{\rm e} n_{\rm H} L(T)$ at which particles radiate away energy depends on density, but happily the spectrum integrated over a cooling time is very nearly independent of n for $n \lesssim 10^{12}{\rm cm}^{-3}$, as is always the case anywhere that shocks occur in these winds. So I compiled a table of integrated emission spectra for each of the series of initial (postshock) temperatures, using a representative density of $n = 10^8{\rm cm}^{-3}$.

The results for several values of $T_{\rm s}$ appear in Figures 3.3 and 3.4, along with the emission spectra of single-temperature plasmas at temperatures equal to the higher values of $T_{\rm s}$. (Because the single-temperature spectra overlap a great deal at low energies, only one temperature is shown in each plot for clarity.) As one might expect, the integrated spectra are softer than those of a gas at the initial T_s: the integrated spectra have more power at lower energies, as a result of emission by the cooling gas at temperatures below T_s. (Note: the normalizations between the integrated and single-temperature curves are arbitrary. A comparison of the overall flux requires assumptions (or model calculations) of the amount of gas at the temperature in question, which will be reserved for later chapters.)

To calculate the spectrum from a wind model, the method using the sudden approximation executes the following steps:

1. Identify the locations r_i, amplitudes $v_{0\,i}$, and preshock densities $n_{\mathrm{in}\,i}$ of all the shocks present in the wind.

2. For each shock, convert that $v_{0\,i}$ to the corresponding temperature T_s, using Eq. 3.7.

3. For each shock, interpolate the integrated spectrum per particle for that T_s from the table, and multiply by the flux $n_{\mathrm{in}\,i} v_{0\,i}$ of particles into the shock.

4. For each shock, calculate the attenuation (at each energy bin in the spectrum) by overlying wind material, and obtain the emergent spectrum from the top of the wind.

5. Sum (for each energy bin) the spectra from all the shocks.

Since PPM already has a shock-recognition algorithm, the sudden approximation method is very simple to implement. It is also much faster than a direct calculation of the emitted spectrum from every zone, because the emission-spectrum calculations have already been done to make the table, and also because it requires calculations only for each of the $\sim$ 100 shocks present in the wind rather than for each of the 1500-3200 zones.

The assumptions made by the sudden approximation are not always valid, and unfortunately they are more likely to fail for the rare, very strong shocks that can provide a large part of the total flux at moderate to high energies, since these shocks have longer cooling times. However, even though the parameters of an individual shock as determined by the model can show substantial variations, the errors introduced by using the sudden approximation in this case are primarily random, rather than systematic. So the method can be improved by averaging the modeled spectra from a number of times within a specified time interval; see Chapter 6 for further discussion, and examples, of these considerations.

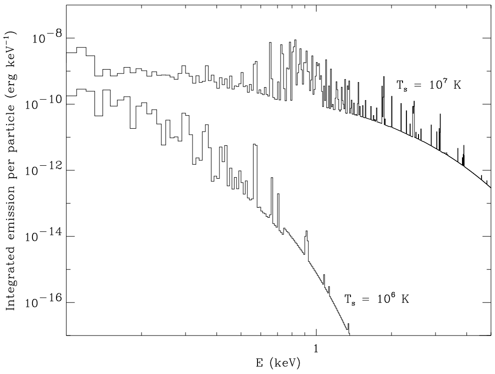

(a) Integrated emission per particle, cooling from an initial temperature of 10^6K (lower curve) or 10^7K (upper curve).

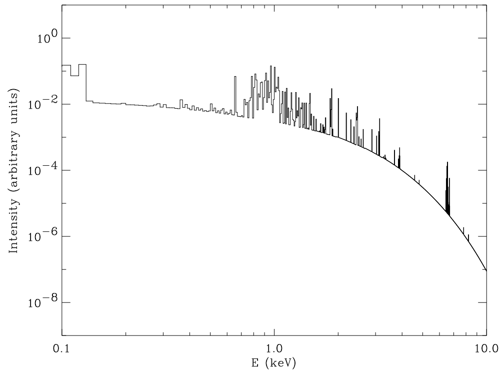

(b) Spectrum of a plasma at $T = 10^7K$.

Figure 3.3: The integrated spectrum emitted by a particle as it cools from initial temperature $T_\mathrm{s} = 10^7K$ or 10^6K, and the spectrum emitted by a single-temperature plasma at $T = 10^7K$, for comparison.

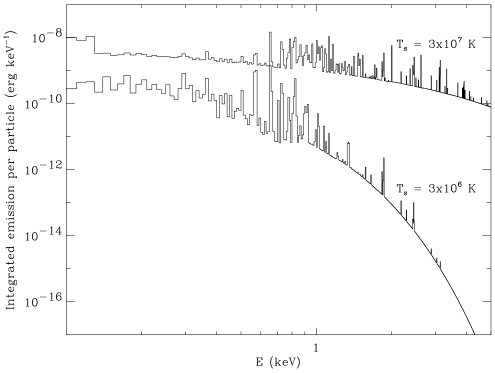

(a) Integrated emission per particle, cooling from an initial temperature of 3×10^6K (lower curve) or 3×10^7K (upper curve).

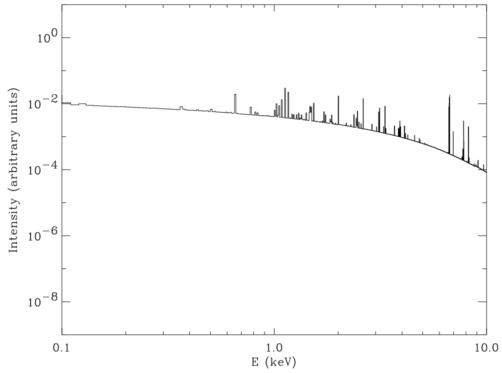

(b) Spectrum of a plasma at $T = 3 \times 10^7K$.

Figure 3.4: The integrated spectrum emitted by a particle as it cools from initial temperature $T_\mathrm{s} = 3\times10^7K$ or 3×10^6K, and the spectrum emitted by a single-temperature plasma at $T = 3 \times 10^7K$, for comparison.

Chapter 4

CHARACTERISTICS OF THE WIND STRUCTURE

Having reviewed the development of the numerical models, some of the technical problems that arose, and my (partial) solutions to them, let us begin looking more systematically at the models' results. In this chapter I will concentrate on those results that are common to the wind models over a wide range of stellar and other model parameters. These include the overall structure of the wind, the nature of the shocks that form, the frequency of strong shocks, and related issues. Spectra and other results from models of stars of particular spectral types will be discussed in chapters 5 and 6.

To illustrate, I will use results from a model of a main sequence star such as μ Col (type O9.5 V). Table 4.1 lists the stellar parameters used. To begin the calculation I used an initial model obtained by setting the source function $S_0 = 0.6$ throughout the wind, which damps the growth of instabilities. (See Sec. 2.2.3 and Owocki 1991.) The initial model relaxes to a smooth steady state similar to a CAK model.

For the full simulation, the model calculates a realistic $S_0(r)$ from the smooth initial state, and then uses this function without change throughout the simulation. In the model shown here, I introduce sinusoidal density perturbations at the base of the wind, varying the density at the boundary with an amplitude $\Delta\rho/\rho = 0.25$ and a period of 4000 seconds.

4.1 The Clumping Instability

As predicted by the linear instability analyses (see Sec. 1.1.3.1), and consistent with isothermal models (OCR, Owocki 1992), all the numerical models confirm that the line driving force is extremely unstable. The dominant global effect is a "clumping instability": the wind material separates rapidly into a series of dense clumps (shells in these 1-D models), separated by highly rarefied regions.

Consider an example of this process. Fig. 4.1(a) shows the initial state of the wind model. Once the simulation with the full, undamped line force begins, this smooth initial state quickly

Table 4.1: Model Parameters

Quantity	Symbol	Value
Mass	M_*	20 $M_\odot$
Luminosity	L_*	3.3×10^4 $L_\odot$
Radius	R_*	6.7 $R_\odot$
Effective Gravity	g_*	$12200 \mathrm{cm\,s^{-2}}$
Effective Temperature	T_{eff}	30,000 K
Opacity constant	$\kappa_0 v_{\mathrm{th}}/c$	$100\,\mathrm{cm^2 g^{-1}}$
CAK power law index	α	0.6
CAK mass loss rate	$\dot{M}_{CAK}$	$1.8 \times 10^{-8}\, M_\odot \mathrm{yr}^{-1}$
CAK terminal velocity	v_∞(CAK)	$1270 \mathrm{km\,s^{-1}}$
PPK terminal velocity	v_∞(PPK)	$3400 \mathrm{km\,s^{-1}}$
Driving amplitude	A	0.25
Driving period	P	4000 s

breaks up into the highly structured state seen in Fig. 4.1(b), after only 10 ksec. The flow time for this model is on the order of $t_{flow} = R_*/v_{wind} \sim 5$ ksec, yet structure already appears all the way to the model boundary at $r = 9R_*$. So this structure is not caused primarily by perturbations propagating up from the wind base, but by the instability of the line driving force itself.

Fig. 4.2(a) shows the model after 30 ksec, when material entering the wind at the start has had time to flow across the model grid. The velocity and other quantities vary rapidly, as intrinsic perturbations grow and collide with interact with others. A few strong shocks have developed, so that some material at X-ray temperatures has appeared. A careful look reveals, however, that the peaks on the temperature graph generally occur at or near troughs on the density graph—that is, the hot regions have low density, and thus the emission measure of X-ray emitting regions is lower than a first look might suggest.

The structure is very complex: besides the clumps, rarefied regions, and strong shocks, we see a large number of other shocks, with a wide range of strengths. In fact, the wind structure is so chaotic that it is hard to understand how the CAK model and subsequent steady-state models can have such success at predicting mass loss rates, terminal velocities, and many features of line profiles. This question is considered in Sec. 4.2.

This complex shock structure increases the resolution difficulties discussed in Chap. 3, since the variety of shock locations and strengths means that hot wind material forms over a large range of temperatures and densities, and thus a wide range of cooling lengths. However, most of the X-ray emission usually comes from only a few very strong shocks (see Chaps. 5 and 6), so that

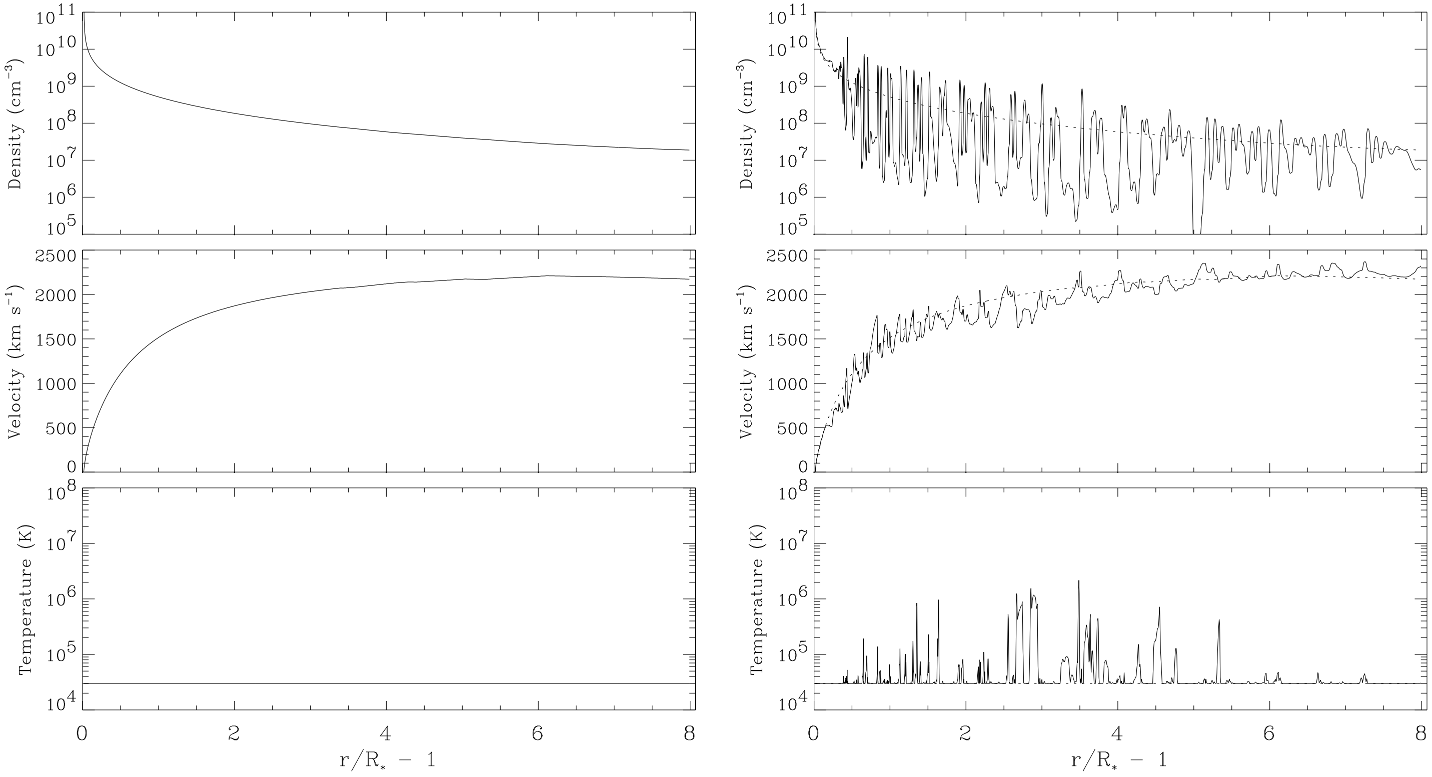

(a) Smooth initial state (time t=0).

(b) Solid line: the model after t = 10 ksec, showing the early development of wind structure. Dashed line: the initial state, for comparison.

Figure 4.1: Density, velocity, and temperature of the sample model; shown here are the initial state and the state after 10 ksec.

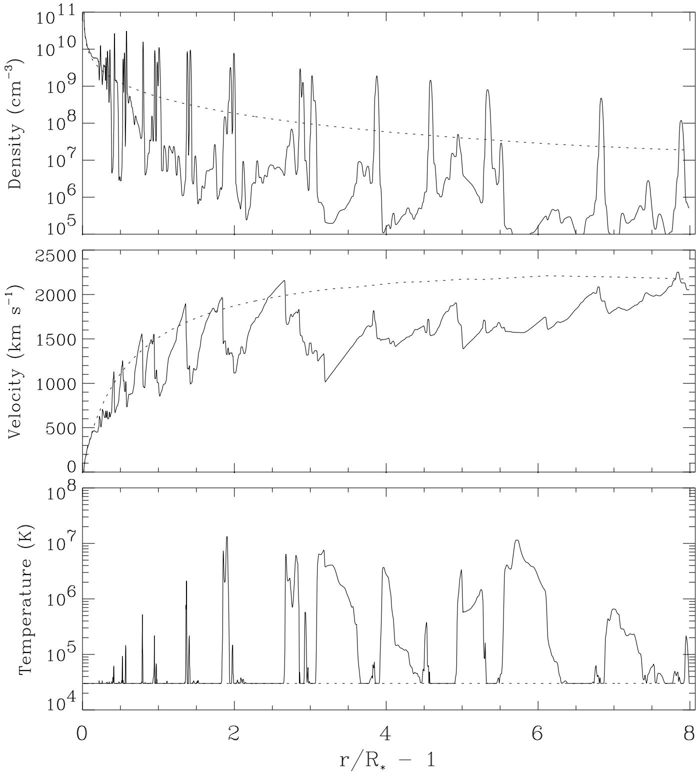

(a) Solid line: the model after t = 30 ksec. The wind has now acquired its characteristic structure: spatially broad rarefied regions terminated by shocks with a wide range of strengths, and separated by narrow, dense shells of unshocked and cooled material. Dashed line: the initial state, for comparison.

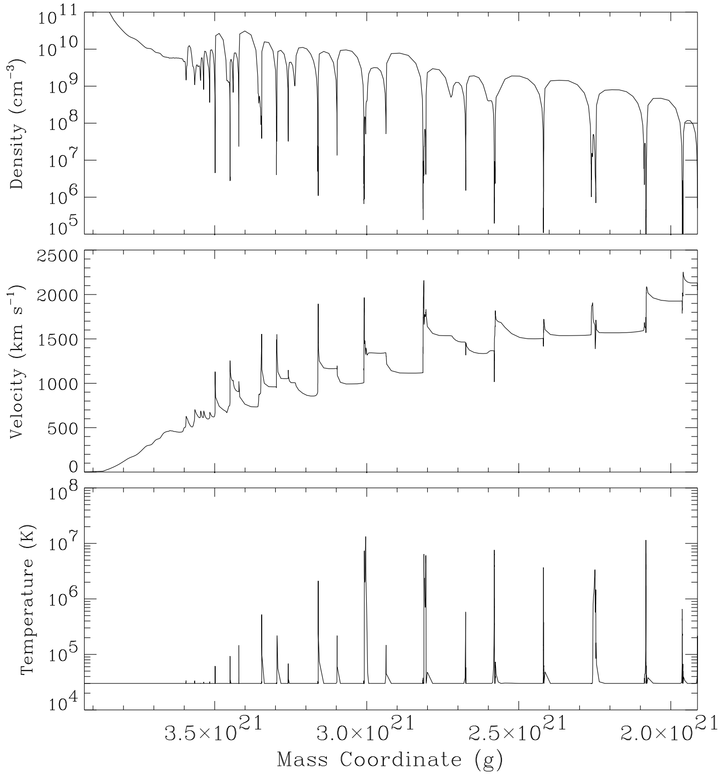

(b) Lagrangian mass coordinate. The cool, dense shells, narrow in plot (a), may be seen to contain most of the total mass of the wind. The broad hot regions in plot (a) are narrow spikes here, containing very little mass.

Figure 4.2: Density, velocity, and temperature of the sample model after 30 ksec, plotted with respect to radius and to a Lagrangian mass coordinate.

uncertainties from the weaker shocks and their postshock regions do not affect estimates of X-ray spectra too severely.

4.2 Tracing the Mass

Besides the impact on X-ray luminosity mentioned above, the large variations in density mean that "Eulerian" plots such as those in Figs. 4.1(a) through 4.2(a), using distance as the independent variable, exaggerate the importance of the extended low-density regions which contain only a small fraction of the wind mass. To show better what is happening to most of the mass we need a "Lagrangian" plot, with distance along the X axis proportional to the amount of *mass* contained in the interval.

4.2.1 Lagrangian mass coordinate

To make such a plot, we define a Lagrangian mass variable

$$m(r,t) \equiv m_0(r) + \int_{t_0}^{t} 4\pi\rho r^2 v\, dt, \tag{4.1}$$

where

$$m_0(r) = m(r,t_0) \equiv \int_{r}^{r_{max}} 4\pi\rho r'^2 dr', \tag{4.2}$$

with r_{max} the outer boundary of the modeled region. Each point in the wind at time t_0 is thus assigned a label corresponding to the initial mass above that point; as each bit of material subsequently enters at the base of the wind, it receives a mass label equal to the total amount of mass that has entered the wind above it. Since (for a 1-D model) material cannot move past other material, each label then remains with the same bit of mass as it moves in the wind.

We can use this mass coordinate $m(r,t)$ in two ways. The most obvious is to replot the quantities of interest *vs.* m, at a fixed time t. For the characteristic clumped wind structure, the spatially narrow, high-density clumps will be spread out, while the broad rarefied regions that occupy much of the Eulerian plots will be compressed to narrow intervals in mass. Fig. 4.2(b) shows the same model as in Fig. 4.2(a), plotted with respect to the mass coordinate. The dramatic fluctuations in velocity that are so prominent in the Eulerian plot appear here as much narrower spikes; nearly all the mass lies fairly close to a smooth curve of acceleration. Similarly, the broad hot regions seen in the temperature plot of Fig. 4.2(a) are much less prominent in Fig. 4.2(b), though some hot material does still appear. For example, the region from $z = 5.5$ to $z = 6.1$ in the Eulerian plot, with temperatures as high as $10^7 K$, is merely a spike (at $m = 2.0 \times 10^{21}$) in the Lagrangian plot.

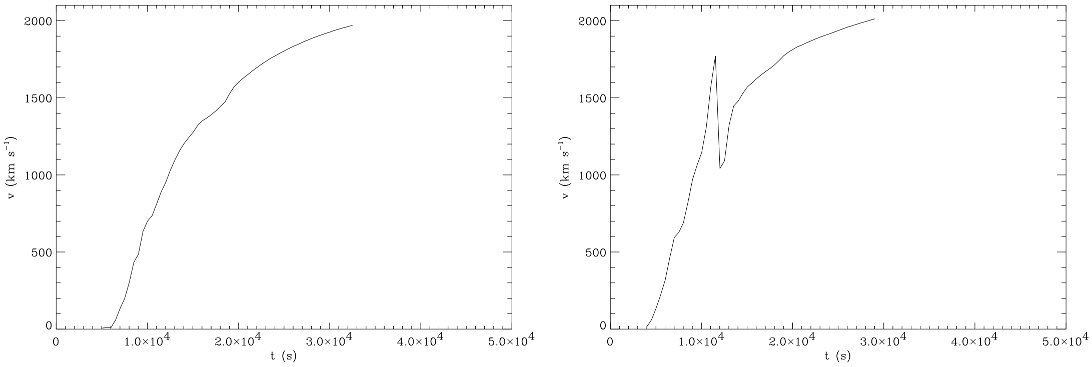

(a) A typical parcel, following approximately a smooth time-independent model velocity law.

(b) A parcel that goes through a strong shock.

Figure 4.3: Velocity histories of two mass parcels.

4.2.2 Following mass parcels

We can also follow a specific parcel of mass as it moves through the wind, by plotting quantities of interest *vs.* t at a fixed value of m. (As I commented above, Eq. 4.1 is defined to follow the flux of mass away from the star, or even toward it in the case of infall; so a specific value of m always labels the same bit of mass.) Figs. 4.3(a) and 4.3(b) show two such parcels: the first follows a fairly smooth path, and the second goes through a strong (600 km s^{-1}) shock.

In the first case, the parcel never experiences a large velocity jump. Even in the second, with a parcel selected to be one that does experience a strong shock, note that it goes through only one sizeable shock—after that, it flows outward as part of a clump. Since this is a model of a low-density wind, the wind cools slowly, and once the parcel is heated, it remains hot; but parcels rarely get strongly heated more than once, or reheated if they cool.

Let us now examine the relative frequency of these two types of particle histories, as well as of intermediate cases.

4.3 Distribution of shock strengths

Fig. 4.4 shows the velocity histories of 50 mass parcels spread evenly through the wind. Small ($\lesssim 100$ km s^{-1}) shocks appear frequently, but the strong ($\gtrsim 250$ km s^{-1}) shocks required to heat material to X-ray emitting temperatures are rare.

In fact, Fig. 4.5 shows that only about 1% of the mass in the wind goes through a shock of 500 km s^{-1} or more. Only about 5% goes through a shock as large as 200 km s^{-1} (with postshock

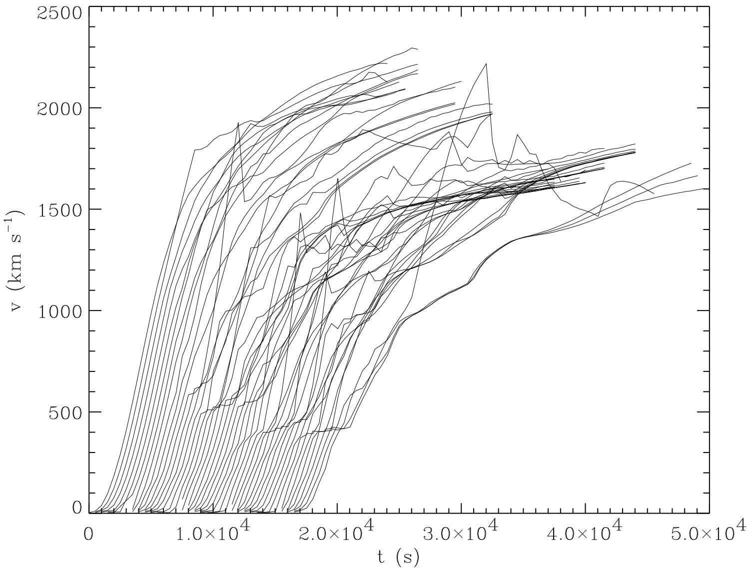

Figure 4.4: Velocity histories for 50 mass parcels, separated by equal mass intervals. Most parcels follow approximately the unperturbed velocity law, though strong shocks are evident for a few.

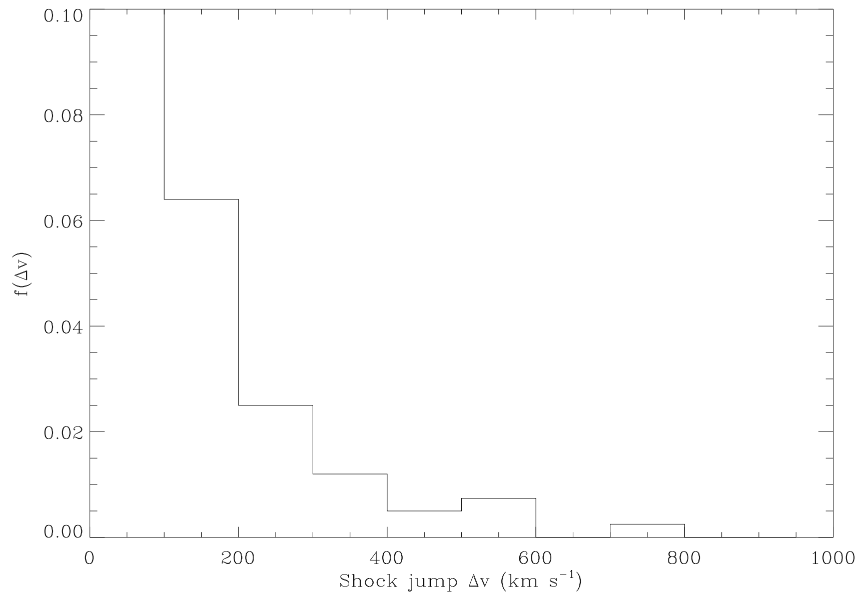

Figure 4.5: Fraction of the mass that goes through shocks of various amplitudes.

temperature $T_{shock} \gtrsim 10^6$K), an approximate minimum for significant X-ray emission. (These values are for the model shown in Fig. 4.2(a), but are typical of those found in all models.)

In the first case, the parcel never experiences a large velocity jump. As we shall see in Chap. 5, this result represents a rather severe restriction on the X-ray flux that is possible from the shock-heated material. It means that the modeled X-ray flux will be small compared to, *e.g.*, the Lucy (1982) model with a single shock strength, which assumed that all wind material would be accelerated and heated by multiple strong forward shocks. This distribution in shock strengths recalls instead the hint seen in Cassinelli and Swank (1983), who found that their observed X-ray spectrum could be fit by a Lucy model only by assuming that one shock in several hundred was a very strong one. (For their fit, the other shocks were all assumed to be identical weak shocks.)

4.4 The Structure of a Typical Shock

Driven shocks in a homogeneous or slowly-varying medium typically form a shock pair: a reverse shock, propagating back toward the star in the frame of the shocked material, where the driven material slows; and a forward shock, propagating outward in the same frame, where the slower overlying material is swept up and accelerated (Hundhausen and Gentry 1969).

However, in these models, no forward shock usually forms. Instead, because the density of the high-velocity material entering the shock is so much lower than that of the wind in front of the shock, only a rarefaction wave propagates outward from one of these typical shocks. Each bit of high-velocity (and low-density) material slows nearly to the velocity of the overlying material in the reverse shock. The shocked material moves with the overlying material. Each bit of this overlying material, in turn, remains unaffected until the pressure gradient above it accelerates that parcel enough to move out of the shadow of the dense shell behind it, at which time it accelerates and rarefies until it goes into a shock higher in the wind.

Because these (reverse) shocks are preceded by very low-density regions, the strong shocks that can produce X-rays generally have only a small flux of mass flowing through the shock. This is really another way of seeing the result of the last section that only a small fraction of the mass goes through a strong shock. Most of the mass simply compresses relatively smoothly into dense clumps and then stays there, separated from any strong shocks that form.

Therefore we can expect that the total emission measure of very hot ($\gtrsim$ a few million K) material will be relatively small, and that a limited fraction of the wind's kinetic energy goes into X-rays. Perhaps this will prove helpful, since $L_{\rm x}/L_{\rm bol}$ is only about 10^{-7}. Chaps. 5 and 6 report on comparisons with observed X-ray spectra.

4.5 Distribution of Emission Measure with Temperature

Because X-ray detectors have had relatively low energy resolution, observed X-ray spectra from hot stars have traditionally been fit to the thermal emission from a gas at a single temperature $T_{\rm x}$ and emission measure EM, or in some cases to a two-temperature model with a temperature and emission measure for each of two components. However, enough information is now available that a more realistic model is needed to fit the observations (Cohen *et al.* 1993).

In any model in which X-rays originate in thermal emission from hot gas, the gas will in general have a distribution of temperatures, rather than a uniform, single-temperature plasma. This is true even if the gas is heated by passing through a single shock, because X-ray emission comes from the postshock cooling region, from gas at temperatures ranging fom the original post-shock temperature $T_{\rm s}$ down to the background temperature of the smooth wind. In addition, as we have seen, the instability of the line driving force results in a large number of shocks with widely varying amplitudes, and therefore widely varying values of $T_{\rm s}$.

Figure 4.7 illustrates this distribution in the emission measure of material at various temperatures. The large amount of emission measure in the first bin shows the "cool" (unshocked)

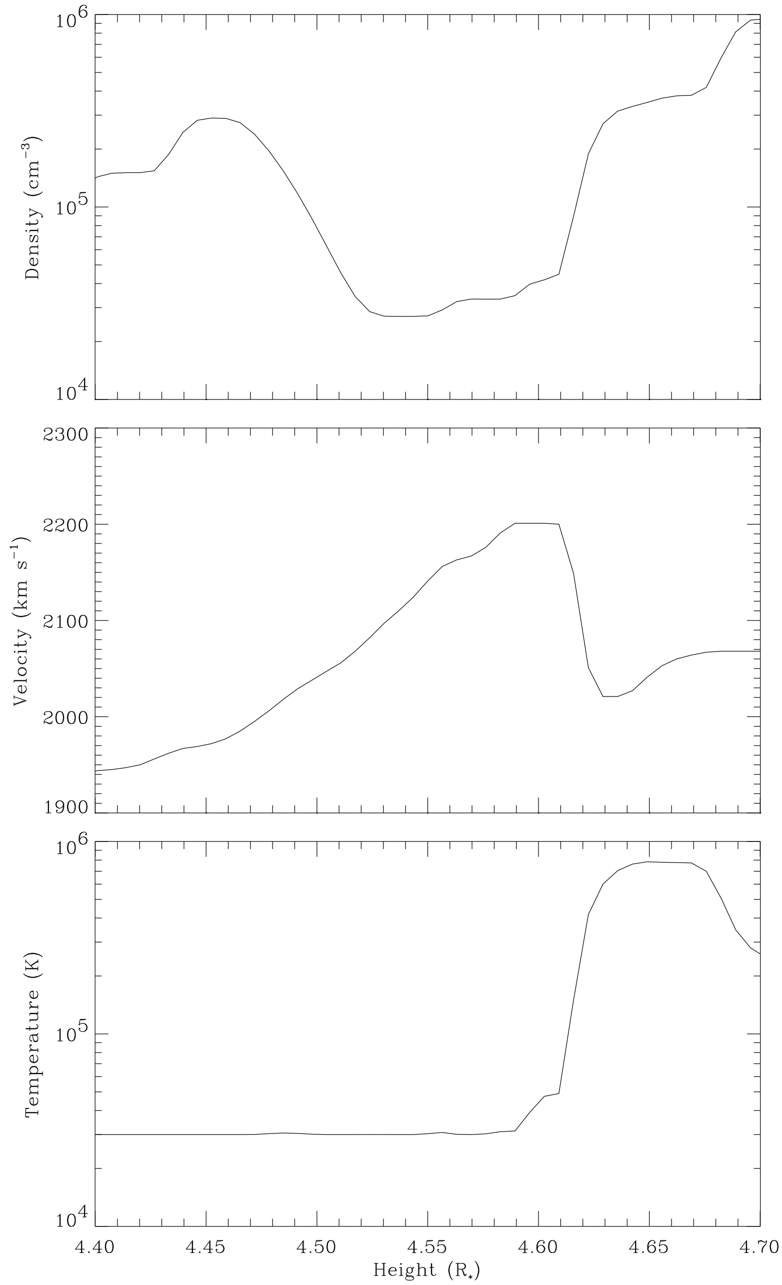

Figure 4.6: A close-up view of the structure of a typical shock. Note the large decrease in density as the particle accelerates just before going through the shock at $z = 4.6$.

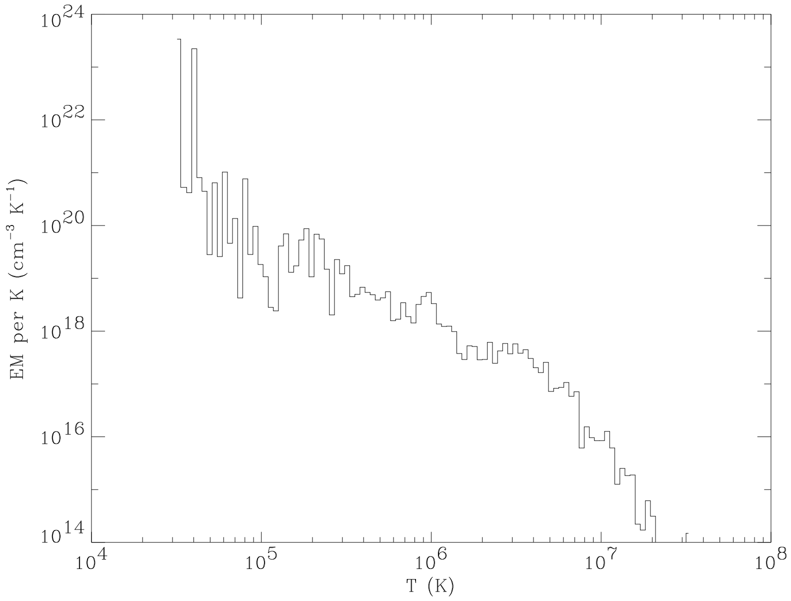

Figure 4.7: The emission measure (per 1K interval) of material at temperature T, in a representative wind model.

wind. Since this is an adiabatic model (no radiative cooling), the low-temperature side of this curve is not realistic, but the emission measures for temperatures above about 10^6 K should be relatively unaffected (see Section 3.4). The figure shows that there is material present at all temperatures between the wind temperature $T_{\rm wind}$ and perhaps 3×10^7 K, and that the emission measure $EM(T)$ of this material varies approximately as $EM(T) \propto T^{-1.5}$.

A goal for future work is to examine the distribution of wind emission measure with temperature in a wider range of models, and (for example) to characterize the range of the power-law exponent in the above relation for $EM(T)$.

4.6 Time-averaged Wind Properties

Sec. 4.2 showed that the bulk of the mass of the wind, at any instant, lies along a relatively smooth velocity curve that is qualitatively like that of a modified CAK (mCAK) model; the violent structures, shocks, and hot regions occur in a minority of the wind mass. However, the curve is significantly flatter than the CAK curve, with the departure beginning about $0.5R_*$ above the stellar surface. The solid curve in Fig. 4.8 shows the same wind model as in Fig. 4.2(a), averaged every 1/2 ksec over a 50-ksec interval.

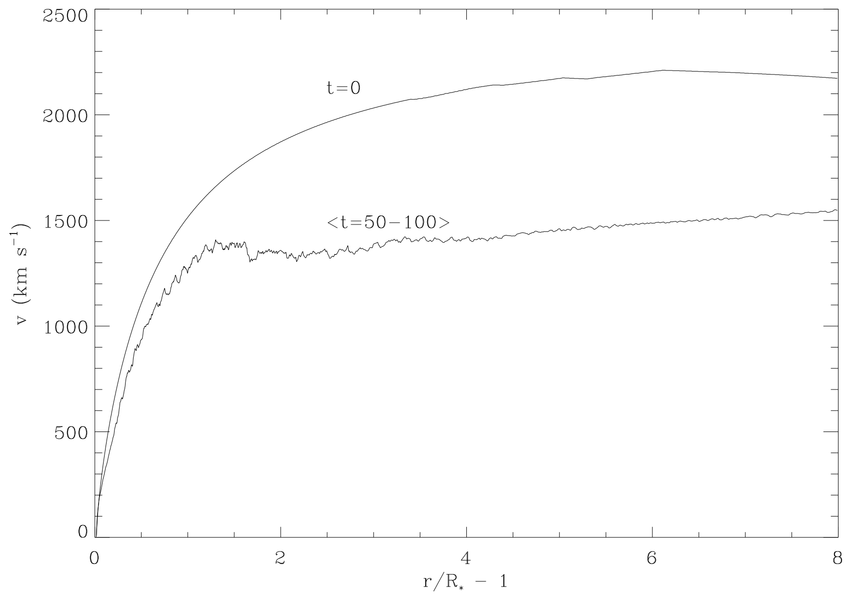

Figure 4.8: The average of 100 snapshots of the wind model, taken every 500 seconds from $t = 50$ ksec to $t = 100$ ksec. The upper curve shows the smooth initial velocity law. The decrease in acceleration above about $z = 0.5R_*$ is apparent.

This flattening in the velocity curve is partly the result of the high-temperature cutoff in the radiation force (see Sec. 2.2). However, almost the same effect occurs in a model using an *isothermal* equation of state, in which the temperature cutoff does not occur. The major cause of the flattening appears instead to be the clumping discussed in Sec. 4.1: wind material becomes concentrated within only certain velocity ranges, so that more stellar photons escape without accelerating the wind.

This effect provides a natural (qualitative) explanation of the fact that the observed terminal velocity in some B stars, *e.g.,* τ Sco, is significantly less than the velocity predicted by modified CAK models. However, a quantitative investigation, as well as comparison to other effects such as the "thermal runaway" described by Springmann and Pauldrach (1992), will wait for later work.

Chapter 5

MODELS OF LOW-DENSITY WINDS

In this chapter and the next I will present dynamical models and model X-ray spectra for two types of hot stars. This chapter discusses results for a main-sequence late O or early B star, with a low-density wind which has relatively long cooling lengths and is optically thin to most X-rays throughout most of the wind. Chapter 6 discusses results for a supergiant, early O star, with a denser wind which has much shorter cooling lengths and much higher X-ray absorption.

Though these models are not intended to provide a detailed fit to a specific star, as references I compare the model results to *Einstein Observatory* and ROSAT observations of the type O9.5 V star μ Col and the type B0 V star τ Sco. τ Sco is perhaps the best-studied star in this spectral range, but it is apparently not a typical example, having both a higher L_x and a harder X-ray spectrum than other stars of nearly the same spectral type. μ Col appears to be more representative of late O–early B main-sequence stars (Cassinelli *et al.* 1994, hereafter CCMSW).

5.1 Summary of Previous Work

5.1.1 X-ray observations of μ Col and τ Sco

X-rays from τ Sco have been observed using three different instruments. Observations using the *Einstein Observatory* imaging proportional counter (IPC) (Grillo *et al.* 1992) showed τ Sco to be a relatively strong X-ray source, with X-ray luminosity $L_x \simeq 3.7 \times 10^{31}$ erg s^{-1}. *Einstein Observatory* solid state spectrometer (SSS) observations by Swank (1985) approximately confirmed the IPC results, and provided evidence of emission from material at temperatures of about 5×10^6 K and 2×10^7 K. Recently, τ Sco has been observed with the ROSAT position sensitive proportional counter (PSPC) by CCMSW. They find emission temperatures of about 2×10^6 K and 8×10^6 K; these are lower than the *Einstein* SSS results, in part because the PSPC is not sensitive to photons much above 2 keV, so that the higher-temperature SSS emission would not be detected by the PSPC. CCMSW also find that the total X-ray luminosity L_x is 2.7×10^{32} erg s^{-1}, several times the luminosity determined by the IPC.

μ Col was also observed with the *Einstein* IPC (Chlebowski, Harnden, and Sciortino 1989). This showed μ Col to be quite typical of late O stars, with X-ray luminosity $L_{\mathrm{x}} = 2.2 \times 10^{31}$ erg s^{-1}. ROSAT PSPC observations by CCMSW agree with the *Einstein* results for μ Col.

The CCMSW observations of other early B stars in luminosity classes V to III show τ Sco to have both an exceptionally high X-ray luminosity and an exceptionally high X-ray temperature. μ Col, on the other hand, is very much like the other stars studied, so that it appears to serve well as a representative example of hot stars with lower-density winds.

Both *Einstein* and ROSAT observations have also been examined for X-ray variability. Those results will be discussed later, in Section 5.7.

5.1.2 Models of X-rays from τ Sco

As we indicated above, models of X-ray emission have concentrated on the O4(n)f star ζ Pup (see Chapter 6) and the B0 V star τ Sco. The observations of CCMSW indicate that the choice of τ Sco may have been an unfortunate one, since τ Sco may be an exceptional case. However, it is useful to continue to consider τ Sco to compare the present models to previous attempts.

Lucy and White (1980) and Lucy (1982) presented a heuristic picture of periodic shocks propagating through, and in fact driving, the wind: wind material in this picture is accelerated by repeatedly going through (forward) shocks. (See Chapter 1 for more details.) They found that this model did not match the IPC results for τ Sco well, but they pointed out that a small number of much stronger shocks could account for the relatively hard X-rays observed.

MacFarlane and Cassinelli (1989) examined another heuristic picture, this one of a faster wind overtaking an earlier, slower wind. They found that a single shock of this type, with a suitable choice of the velocity difference and preshock density, could produce an X-ray spectrum similar to that observed by the SSS for τ Sco. In their model, a forward-reverse shock pair developed—a quite different structure from the periodic forward shocks in the Lucy models, but consistent with the shock structures in the models described here. This is not surprising, since the Lucy models did not attempt to solve the hydrodynamic equations, but simply investigated the consequences if the periodic shock structure did form.

These indications that the observed X-rays can be produced (at least in principle) by thermal emission from shock-heated material encourage us to proceed to look at the results of time-dependent, dynamical models. However, recalling the shock characteristics described in Chapter 4, we can see that producing the substantial X-ray fluxes observed may be a challenge, since the reverse shocks typically seen in these models heat only a fraction of the wind to X-ray temperatures.

5.2 The Hydrodynamical Model

A brief summary of the approach we use to model radiation-driven winds might be helpful.

We specify the stellar parameters L_*, M_*, R_*, and $T_{\rm eff}$. The equilibrium wind temperature $T_{\rm wind}$ is assumed equal to $T_{\rm eff}$.

The CAK parameter α is chosen from the table in Abbott (1982a), or from more recent work by the Munich group, if available. We choose the parameter κ_0, analogous to the CAK k, so that the resulting model mass-loss rate fits the observed value (or range of values) of $\dot{M}$ as well as possible.

At the outer boundary of the modeled region, we use outflow boundary conditions on the velocity v, density ρ, and pressure P. At the inner boundary, we fix the value of ρ in the "ghost" zones at a value ρ_{in} that results in a smooth, stable wind. We also fix P in the ghost zones, at a value $P_{in} = (\rho_{in}/\mu)\, kT_{\rm wind}$. We specify v in the inner ghost zones by extrapolating the slope of the velocities in the first two active zones.

Note that the observed quantities v_∞ and $\dot{M}$ are not input parameters, but *results* calculated by the model. In fact, v_∞ varies with time, as various wind structures propagate through; $\dot{M}$ may be measured at any point in the wind, and also varies with time—by several orders of magnitude, when a dense shell passes the measuring point. To compare with the observed values, we use time averages of each quantity.

5.3 Effects of Attenuation

To estimate cross sections for X-ray attenuation by overlying wind material, we use the formula given by Morrison and McCammon (1983). For the low-density wind models in this chapter, the effect of absorption is small over the entire range of energies (0.5 to 4.5 keV) considered. At lower energies, attenuation would significantly affect the emergent X-ray flux, but modeling the spectrum at those energies will require a better knowledge of the ionization state of the wind.

These and other issues relating to wind attenuation are discussed more extensively in Section 6.3, since attenuation does have a significant effect on the spectra of higher-density winds. For the present, low-density models, we present the model spectra including the effects of wind attenuation; in all cases, however, those effects are small over the modeled energy range.

5.4 A Typical Model with No Adjustments

We have already seen in Chapter 3 that numerical and physical constraints combine to make it difficult to resolve the hot postshock regions well enough to properly estimate their X-ray emission. Let us look at the effect of these constraints on the calculated model spectrum.

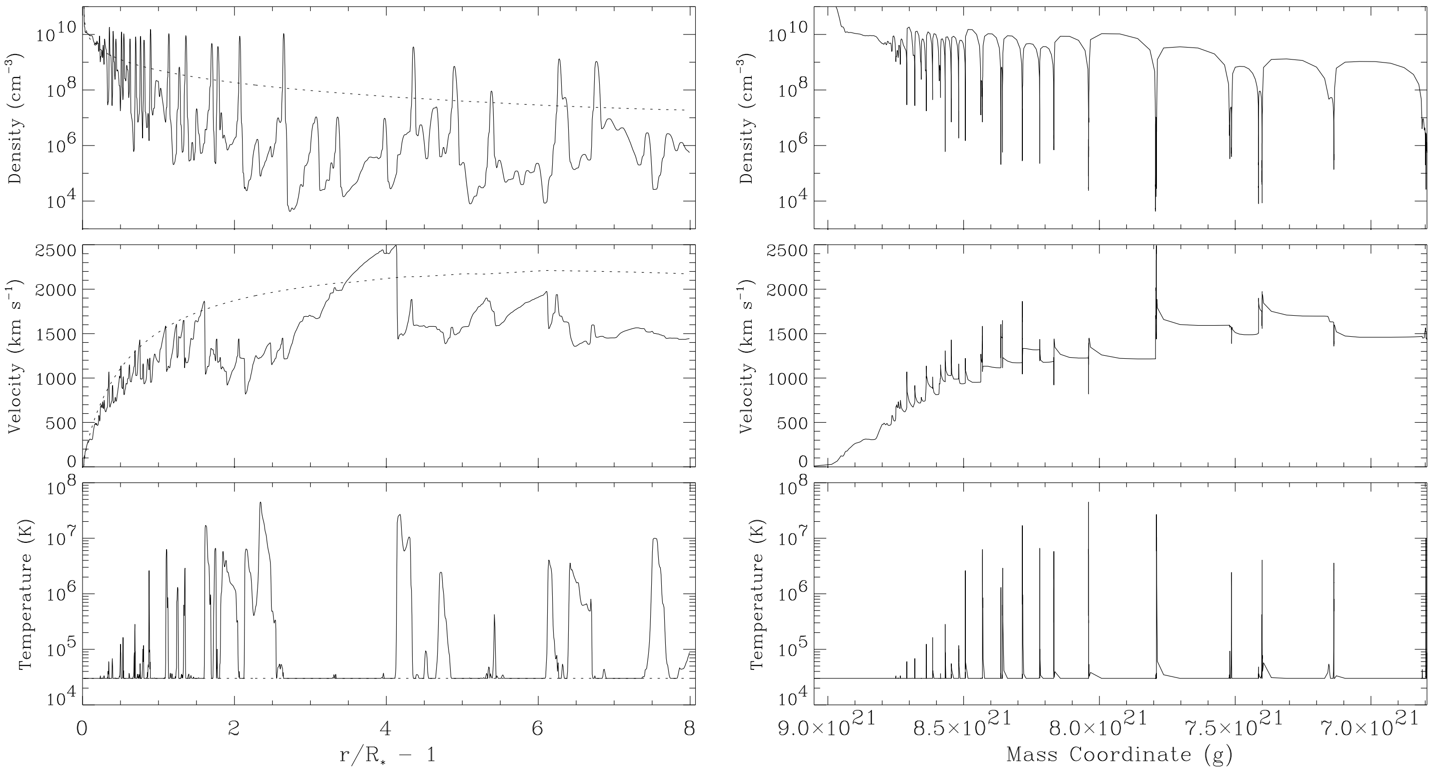

(a) Eulerian plot, with obvious but limited hot postshock regions.

(b) Lagrangian plot, showing that hot regions are very narrow in mass.

Figure 5.1: A typical low-density wind model, with no special provisions to increase resolution of postshock regions.

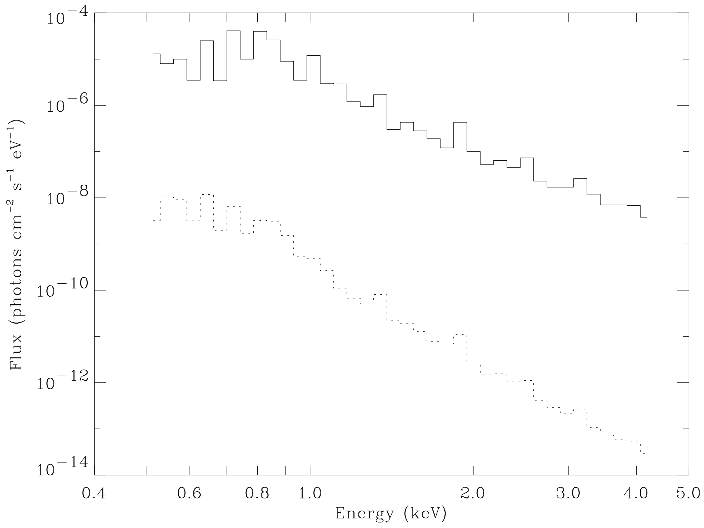

Figure 5.2: X-ray spectrum for the low-density wind model shown in Figure 5.1. Solid line shows the observed spectrum of τ Sco (Swank 1985); dotted line shows the model spectrum.

Figure 5.1 shows a model using the standard stellar parameters for an B0 V star listed in Table 4.1. This is the same model as that shown in many of the figures in Chapter 4, though it is shown here at a later time. As in those figures, the hot regions are narrow, especially when viewed as a function of the mass coordinate, as in Figure 5.1(b). For example, the region following the shock at $z = 4.1$ is only about 0.25 R_* wide, even though the cooling length for a shock this size at this (very low) density is about $L_{\rm cool} \sim 2 \times 10^5 R_*$. (See Eq. 3.8.)

This suggests that an attempt to calculate the X-ray spectrum directly will give a fairly low result. And that is exactly the case, as shown in Figure 5.2. The model has $L_{\rm x} = 4.1 \times 10^{28}$ erg s^{-1}, a factor of 6×10^3 below the observed value of 2.7×10^{32} erg s^{-1} (CCMSW). The model spectrum has roughly the same shape and features as the observed spectrum, but is below it by factors of 10^4 or so, consistent with the integrated $L_{\rm x}$ values.

Although the narrow hot regions indicate that much of the hot material gets lost to numerical diffusion, the model does have a non-negligible emission measure of material hotter than 10^6 K. The fact that the model spectrum is so far below the observations, even with this significant amount of hot material, suggests that a surprisingly large fraction of the wind must be hot—a point made also by CCMSW.

5.5 Adiabatic Models: Radiative Cooling Shut Off

5.5.1 Uncorrected version

To establish an upper limit to the amount of hot material that might be present in one of these models, we can artificially set the radiative cooling rate $\Lambda(T) = 0$, so that the only cooling process is adiabatic expansion. (Numerical diffusion, described in Section 3.3.1, also acts to "cool" the hottest material by averaging it with neighboring, cooler material.)

As we argued in Section 3.4, cooling times in low-density winds for hot, X-ray emitting material are generally very long, in particular for material at X-ray emitting temperatures above 10^6 K. So setting $\Lambda(T) = 0$ is a relatively good approximation for these regions, and the amount of material at X-ray temperatures $T \gtrsim 10^6 K$ will not be too greatly overestimated.

Material at somewhat lower temperatures, a few$\times 10^5 K$, cools much faster, and will therefore be overestimated by a larger factor. This eventually affects the wind dynamics relatively far out in the wind (see below). However, since most X-ray emission comes from strong shocks in the first few R_*, and from hotter material, the model X-ray spectrum itself is not affected very much by this excess "warm" material.

Figure 5.3 shows the result of this adiabatic approximation. As expected, the model now shows a great deal of hot material. In fact, almost all the wind material above about 0.5 R_* is hotter than the stellar effective temperature of 30,000 K, though only a relatively small fraction of the wind material is at X-ray emitting temperatures of 10^6 K or higher. This is because, as we saw in Section 4.3, only a small fraction of wind material ever goes through a shock strong enough to heat the gas to X-ray temperature.

There is now enough hot material to produce a much larger X-ray flux than in the previous model. As shown in Figure 5.4, the model spectrum is below the observed τ Sco spectrum by a factor of about 10. The model X-ray luminosity is $L_{\mathrm{x}} = 3.1 \times 10^{31}$ erg s^{-1}, compared to the observed value 2.7×10^{32} erg s^{-1}.

The velocity curves in Figure 5.3 show a side effect of neglecting radiative cooling: because so much material is (artificially) hot—primarily at temperatures between 10^5 K and 10^6 K—the radiative force is essentially cut off above about $r = 2R_*$. (Recall from Chapter 2 that we introduced an exponential temperature cutoff term $\exp(-(T - T_0)/T_0)$ for the radiative force as a crude approximation to the effect of ionizing the driving species in the wind. Initially, we used $T_0 = T_{\mathrm{wind}} = T_{\mathrm{eff}}$.)

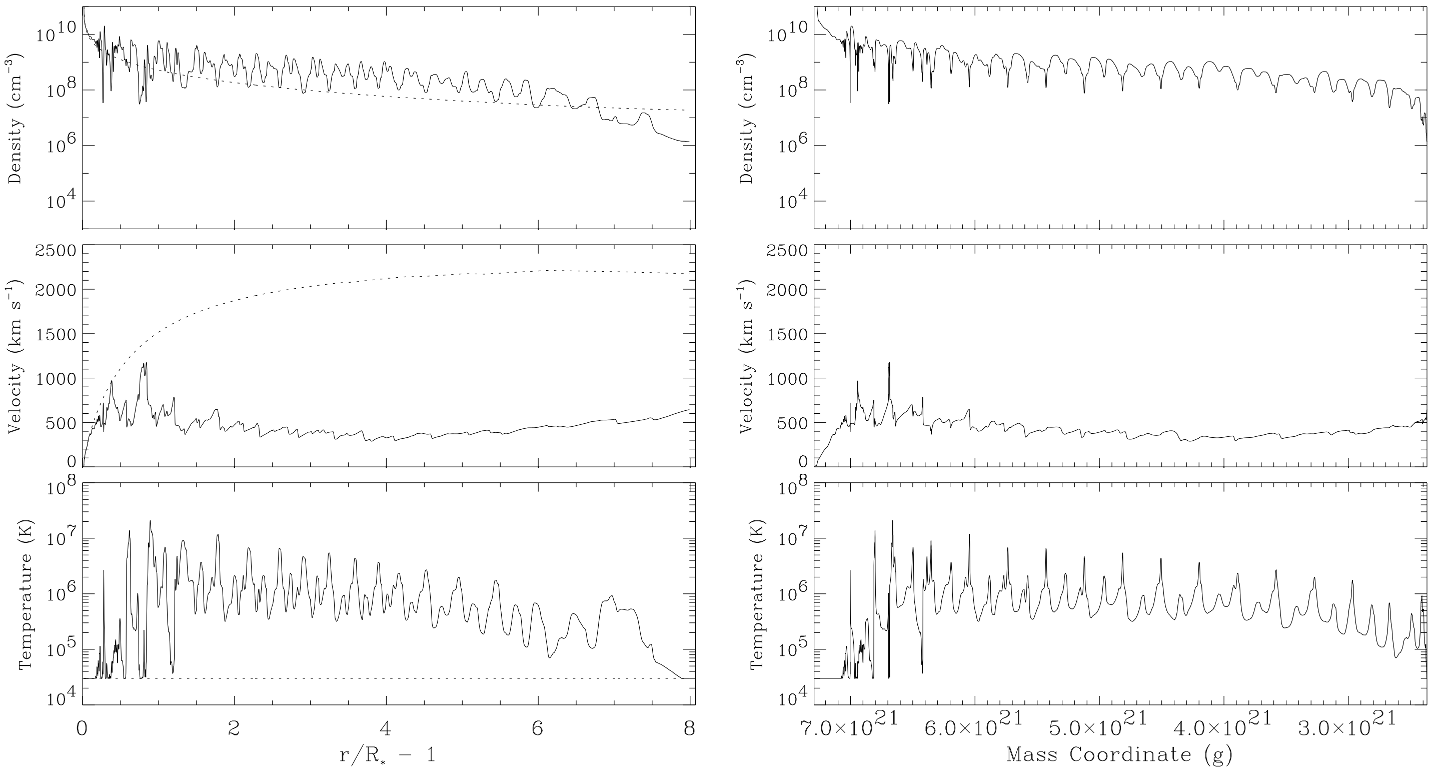

(a) Eulerian plot, with broad hot postshock regions.

(b) Lagrangian plot

Figure 5.3: A model with radiative cooling turned off. This "upper limit" model shows abundant hot material, though most of the wind material remains below 10^6 K.

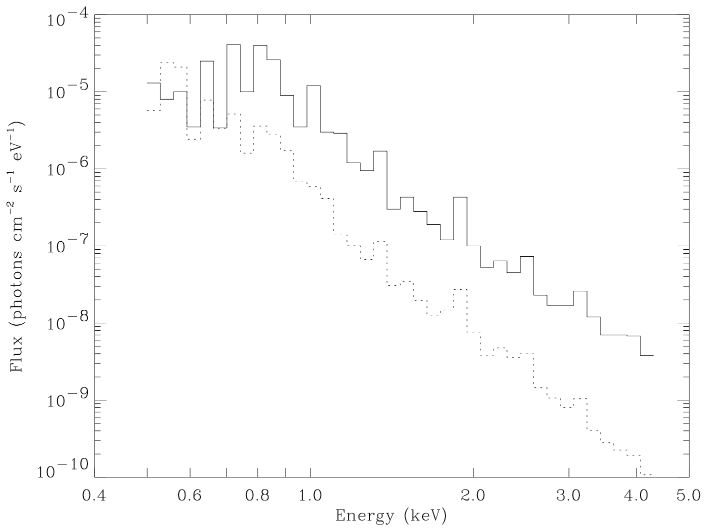

Figure 5.4: X-ray spectrum for the adiabatic model, shown in Figure 5.3. Solid line shows the observed spectrum of τ Sco (Swank 1985); dotted line shows the model spectrum.

5.5.2 Corrected version

To correct (somewhat crudely) for this, we could cut off radiative cooling as before, but with the "ionization" cutoff set at a higher temperature. Figure 5.5 shows a model in which the cutoff temperature T_0 was set to $T_0 = 5 \times 10^5$ K. With this choice of T_0, material at X-ray temperatures above 10^6 K or so does not contribute to line driving. But the rather large part of the wind at temperatures of a few $\times\ 10^5$ K—which would cool rapidly if radiative cooling were not shut off, and is therefore most affected by using an adiabatic model—does now contribute to driving the wind.

The velocity law of the wind in this model agrees better with the observed v_∞, and with the velocity laws of models that include radiative cooling. The X-ray spectrum, shown in Figure 5.6, is similar to that of the model with $T_0 = T_{\rm wind}$ and no radiative cooling.

5.6 A Model with the Wind Unstable at the Base

In a few models, the wind instability reached all the way to the base of the wind. These models may have been unstable for numerical, rather than physical, reasons. However, we might imagine them to be examples of what might happen if instabilities in the stellar atmosphere—for example, nonradial pulsations or magnetic structures—couple to the wind. In such a case, a faster

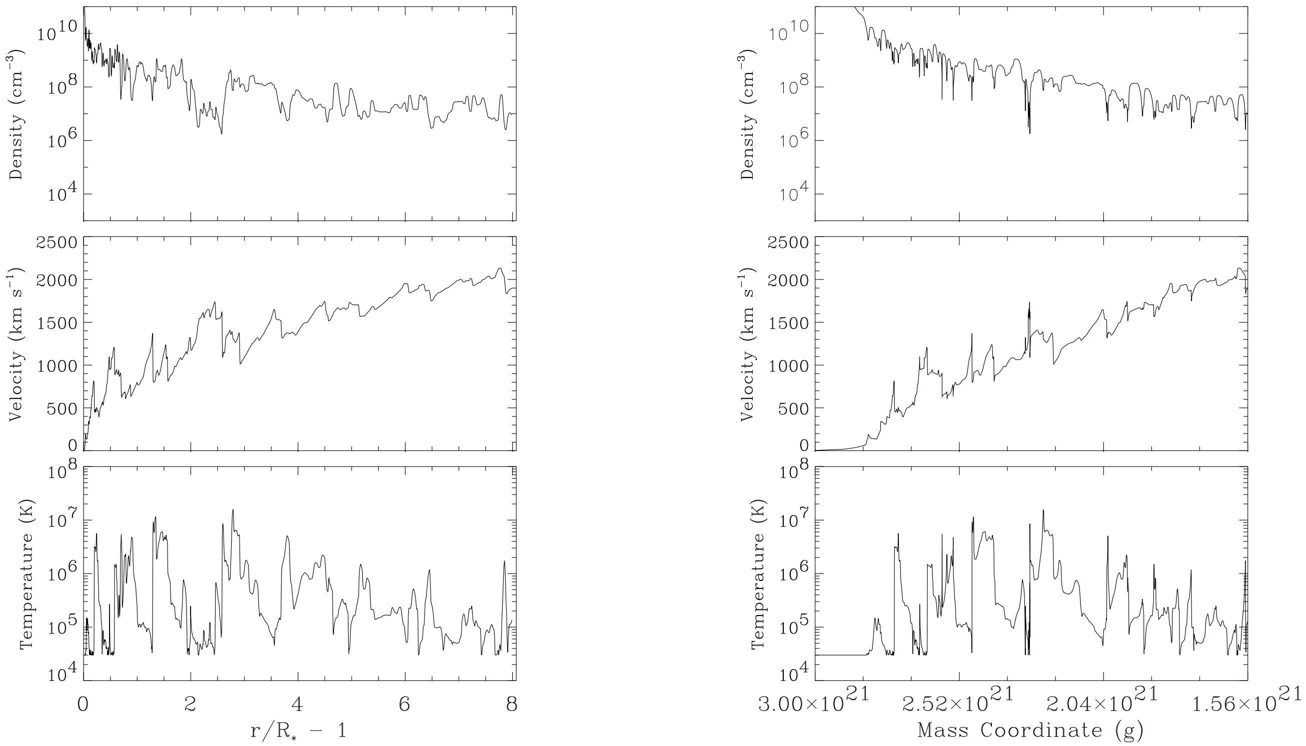

(a) Eulerian plot. Broad hot regions remain, and the velocity law is closer to what is observed.

(b) Lagrangian plot

Figure 5.5: A model with radiative cooling turned off, and the ionization cutoff temperature $T_0 = 5 \times 10^5$K.

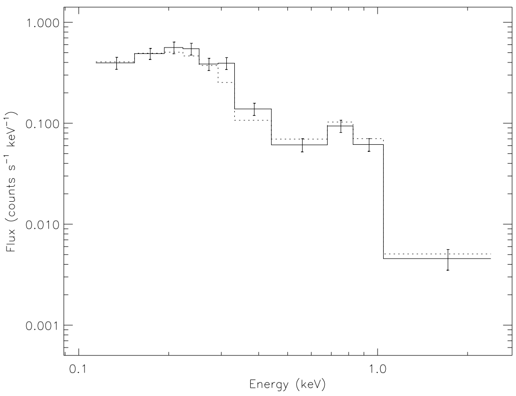

(a) Comparison with the ROSAT PSPC spectrum of μ Col (CCMSW). Solid line: observed spectrum; dotted line: model spectrum at time $t = 100$ ksec.

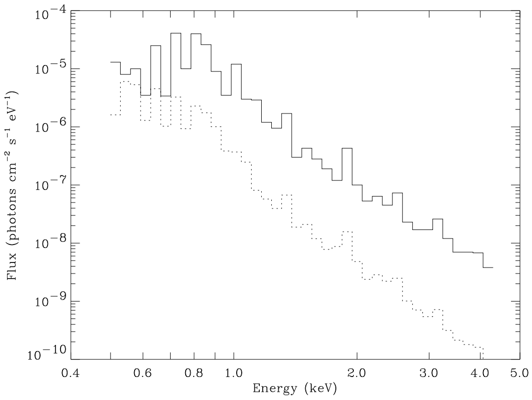

(b) Comparison with the *Einstein* SSS spectrum of τ Sco (Swank 1985). Solid line: observed spectrum; dotted line: average of 50 model spectra, calculated every 0.5 ksec between $t = 75$ ksec and $t = 100$ ksec.

Figure 5.6: X-ray spectra for the adiabatic model with higher ionization cutoff temperature, shown in Figure 5.5.

wind encounters the overlying, slower wind, creating a situation something like that envisioned by MacFarlane and Cassinelli (1989). A strong *forward* shock propagates through the wind at this boundary between faster and slower wind, so that most of the wind material gets swept up by the shock and heated to X-ray temperatures. This is quite different from the models we have seen, in which the strong shocks are all reverse shocks preceded by strong rarefactions, so that only a relatively small fraction of the wind material ever goes through a strong shock.

Figure 5.7 shows such a model. Notice that the strong shock at $z \sim 5.6R_*$ lies at the *leading* edge of the associated hot region, as does a newly forming shock at $z \sim 0.8R_*$. The typical reverse shocks occur when small amounts of material get accelerated far above the "underlying" wind velocity (and become highly rarefied in this expansion), and then shock back to the lower velocity. Here, in contrast, the wind preceding the shock follows a generally smooth velocity law, and the density behind the shock is much higher. This maintains the strong forward shock, which encounters wind material above it at typical (un-rarefied) wind densities, and therefore the mass flux into the shock is much higher than for the reverse shocks.

Because a large fraction of the wind material gets heated, the model X-ray luminosity is high. As shown in Figure 5.8, the model X-ray spectrum for this model is nearly as high as the observed spectrum of τ Sco—a star which, as we commented at the beginning of this chapter, shows

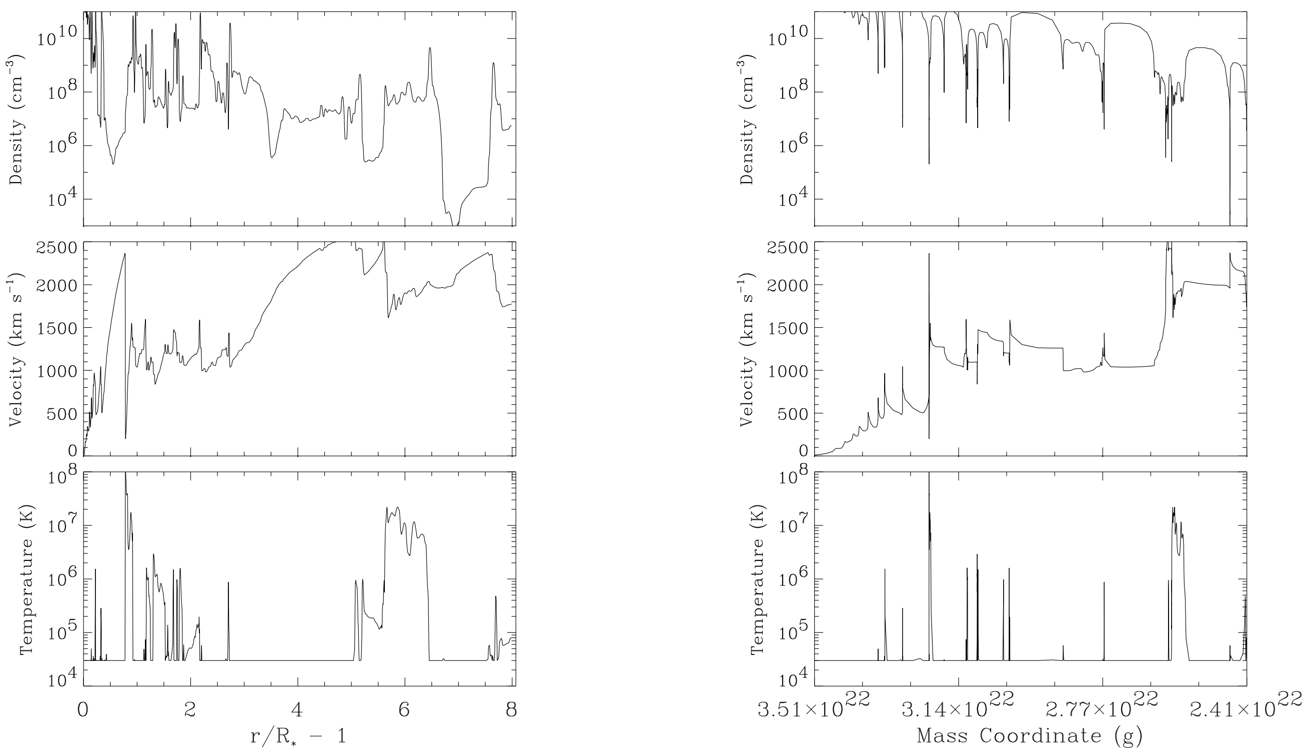

(a) Eulerian plot. Notice that the preshock acceleration regions do not show the usual sharp dip in density.

(b) Lagrangian plot. A substantial amount of mass now appears in the hot region at $M = 2.6 \times 10^{22} g$.

Figure 5.7: A model in which a strong forward shock develops. A large fraction of wind material is heated to X-ray temperatures.

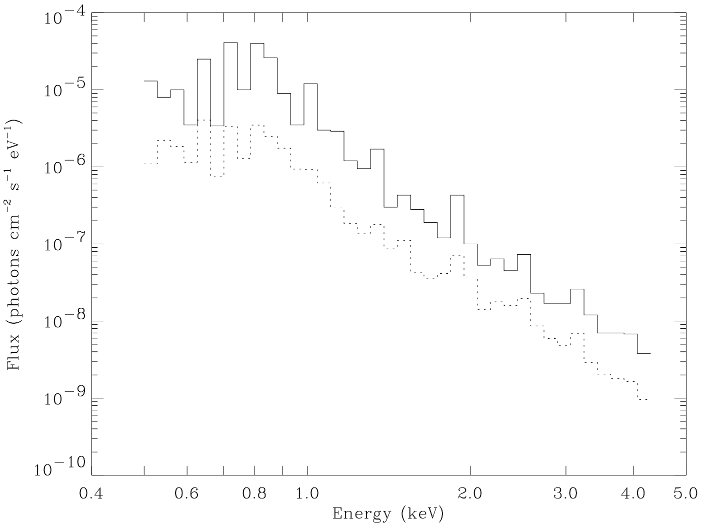

Figure 5.8: X-ray spectrum for the model with a strong forward shock, shown in Figure 5.7. Solid line shows the observed spectrum of τ Sco (Swank 1985); dotted line shows the model spectrum.

anomalously high X-ray luminosity, as well as an anomalously high derived X-ray temperature.

A recent suggestion that τ Sco may be a Be star seen pole-on (Waters *et al.* 1993) may partially explain why τ Sco's X-ray spectrum is so different from other stars with similar spectral types. Alternatively, if a mechanism can be found to generate the sort of wind instability at the base that is seen in this model, the forward shocks produced by such an instability can heat enough of the wind to high enough temperatures to generate the observed X-ray spectrum.

5.7 Time Variability of X-ray Emission

5.7.1 Variability in X-ray observations

Collura *et al.* (1989) tested the *Einstein Observatory* data from τ Sco for variability. They found marginal (3 σ) evidence for short-term variability in one of the six data sections, with amplitude of about 30% and time scale of roughly 50 s. Since τ Sco was observed on only one day, the *Einstein* data said nothing about variability on longer time scales.

The ROSAT observations of CCMSW detected variability in τ Sco of about 20%, with a period of 125 seconds, but they state that this was most likely a result of the spacecraft wobble. Indeed, a more recent ROSAT observation, more than a year after the first, shows the same L_{x} to

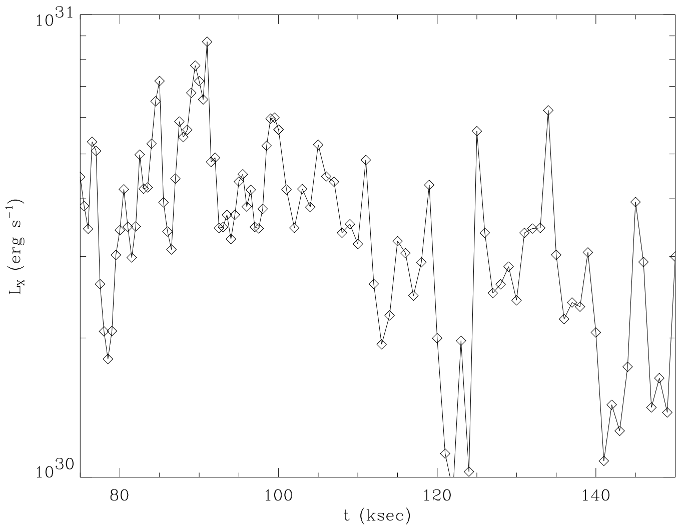

Figure 5.9: Variability of the integrated X-ray luminosity $L_{\rm x}$, for the model of Figure 5.5.

within a few percent (Cohen, private communication). CCMSW found no evidence of variability in μ Col, on scales from seconds to hours.

5.7.2 Variability of modeled X-rays

In contrast, the modeled X-ray luminosities show fluctuations by factors of 2–5, over time intervals of 10^3 to 10^4 seconds. Figure 5.9 shows the model $L_{\rm x}$ as a function of time for the model of Section 5.5.2.

This level of variability is present because most of the X-ray emission comes from the few strongest shocks. As one or more of these shocks changes its amplitude or reaches material with a different density, or flows off the numerical grid, the integrated X-ray luminosity is affected. For the present one-dimensional model, of course, we assume each shock to cover uniformly a spherical shell around the star at the shock's radius. However, in the actual three-dimensional case, it is likely that the X-ray emission comes fom a larger number of shock fragments, each with a limited angular extent, thus lowering the effect of changes in any one shock on $L_{\rm x}$.

For example, since the line driving force is unstable only to perturbations with wavelengths shorter than the Sobolev length

$$L_{\rm Sob} = \frac{v_{\rm th}}{dv/dr} \sim \frac{a}{v_\infty/R_*} \tag{5.1}$$

$$\sim 10^{-2} R_*, \tag{5.2}$$

we might expect on the order of 100 or more such shock fragments per stellar radius R_*, thus reducing the amplitude of variability by a factor on the order of $\sqrt{100}$, thus by a factor of perhaps 10–20.

Chapter 6

A MODEL OF A HIGH-DENSITY WIND

This chapter discusses results for models of a supergiant, early O star, with stellar parameters corresponding to those of the type O4(n)f star ζ Pup. This is one of the best-studied O stars (see, *e.g.,* Hillier *et al.* 1993, Corcoran *et al.* 1993, and references therein.) ζ Pup has the earliest spectral type of those O stars for which X-ray spectra are available, and thus is near the high end of the range of mass loss rates and wind densities among type O and B stars.

Because of the high mass loss rate (about 3×10^{-6} $M_{\odot}$/year in our models, compared to about 1.5×10^{-8} $M_{\odot}$/year for the models discussed in Chapter 5) and the resulting higher wind densities, radiative cooling is typically more rapid, and the postshock regions correspondingly narrower. Therefore we use the "sudden approximation" described in Section 3.5 to calculate model X-ray spectra.

6.1 X-ray Observations of ζ Pup

ζ Pup has now been observed several times at X-ray wavelengths.

Cassinelli *et al.* (1981) used low-resolution spectra obtained with the *Einstein Observatory* imaging proportional counter (IPC) to test the coronal model of X-ray emission (Cassinelli and Olson 1979). Since X-rays emitted from a coronal region must traverse the entire wind, the corresponding optical depth is very large for low-energy photons in a dense wind, so that low-energy photons are strongly absorbed. Cassinelli *et al.* found that, for ζ Pup as well as for two other stars, a model with a coronal source at the base of the wind did not fit the IPC spectrum. However, a model with a source higher in the wind, experiencing less wind attenuation, could easily fit the observations.

This conclusion was supported by higher-resolution spectra from the *Einstein* solid state spectrometer (SSS), though ζ Pup itself was not observed with this instrument. SSS observations of other O stars (*e.g.,* Cassinelli and Swank 1983) showed no evidence of strong absorption features, such as the oxygen K-shell absorption edge at about 0.6 keV. So the observed X-rays, at least the softer ones, apparently must come from higher in the wind.

Recently, two groups with new observations have reported detecting evidence of X-ray attenuation in the wind of ζ Pup.

Hillier *et al.* (1993), used the ROSAT position sensitive proportional counter (PSPC) to observe ζ Pup. The PSPC has higher sensitivity and can detect lower energies (0.1 keV) than the *Einstein* instruments. The PSPC has higher spectral resolution than the *Einstein* IPC, though not as high as the *Einstein* SSS. Hillier *et al.* do not find evidence of the oxygen or nitrogen absorption edges; and, since they see some photons even at 0.1 keV—where optical depth $\tau = 1$ occurs only at $r \sim 1000R_*$—they conclude that at least some of the X-rays must originate beyond $r = 100R_*$.

They use a modified-CAK, time-independent model for the wind dynamics, and include full radiative transfer and ionization balance, including the ionizing effects of the emitted X-rays. A model with the X-rays originating from a corona cannot provide a good fit to their observed spectrum. However, they are able to fit their observations with a model that envisions shocks (thus, hot material) distributed uniformly from some minimum radius $R_{min} = 1.5R_*$ outward, and a combination of two temperatures with $\log T_s = 6.66$ and 6.23. In fact, they can get a good fit to their observations even if all the X-rays originate above $R_{min} = 10R_*$, though they argue that this model is less plausible than one with $R_{min} = 1.5R_*$.

Corcoran *et al.* (1993), using the Broad-Band X-Ray Telescope (BBXRT), report detecting the long-sought oxygen absorption edge in ζ Pup. BBXRT is not sensitive to the lowest-energy photons observed by the ROSAT PSPC, with a range of 0.3–12 keV for BBXRT, compared to 0.1–2.5 keV for the PSPC. But the energy resolution of BBXRT is higher: $E/\Delta E \simeq 11$ at 1 keV for BBXRT, $E/\Delta E \simeq 2.4$ for PSPC. To obtain an acceptable fit to their observations, Corcoran *et al.* must include a significant amount of wind attenuation, although less than the amount that would result if the X-rays originated in a corona at the base of the wind. They estimate this overlying attenuation, and find that the inferred column depth of absorbers indicates that the X-rays originate between about $r = 3.1$ and 9.7 R_*.

Using the BBXRT and IPC observations, together with line profiles of UV resonance lines, MacFarlane *et al.* (1993) confirm that a coronal model would result in more than the observed amount of attenuation. They calculate models somewhat like those of Hillier *et al.*, with hot X-ray emitting regions distributed throughout various regions of the wind, and with a model of the radiation transfer and ionization balance in the wind. Their preferred model rules out a coronal origin for the X-rays, but requires at least some X-ray emission as low as $r \lesssim 2R_*$ to account for the observed presence in UV lines of O VI at low velocities.

6.2 The Hydrodynamical Model

6.2.1 Description of model

Table 6.1 lists the stellar parameters used for a high-density wind model. The parameters are as determined by the Munich group (Herrero, private communication), except that the normalization constant k was modified here to obtain a mass loss rate consistent with the observed range of values.

This model uses the "optically thin" form of the smooth source function (SSF) approximation (Section 2.2.3); other models using the optically thick form show similar results. As with the low-density wind models described in Chapter 5, we begin the model from a smooth, CAK-like initial state.

Table 6.1: Parameters for a High-Density-Wind Model

Quantity	Symbol	Value
Mass	M_*	$40\ M_\odot$
Luminosity	L_*	$6.9 \times 10^5\ L_\odot$
Radius	R_*	$19\ R_\odot$
Effective Gravity	g_*	$3030\ \mathrm{cm\,s^{-2}}$
Effective Temperature	$T_{\rm eff}$	37,800 K
Opacity constant	$\kappa_0 v_{\rm th}/c$	$3500\,\mathrm{cm^2\,g^{-1}}$
CAK power law index	α	0.7
Mass loss rate	$\dot{M}$	$3 \times 10^{-6}\,M_\odot\,\mathrm{yr^{-1}}$
CAK terminal velocity	v_∞(CAK)	$940\ \mathrm{km\,s^{-1}}$
PPK terminal velocity	v_∞(PPK)	$2700\ \mathrm{km\,s^{-1}}$

In addition to the new stellar parameters, the resulting higher-density wind makes it necessary to modify several features of the numerical model itself. First, since the wind has a higher column density of absorbers than the corresponding point in a low-density wind, it is necessary to extend the model grid out farther, so that the modeled region includes the X-ray photosphere. For example, in the model shown in Figure 6.1, optical depth $\tau = 1$ occurs at $r = 14R_*$ for 0.5 keV photons, and at $r = 8R_*$ for 1.0 keV photons. The models shown here extend from $r = 1$ to 27 R_*.

Because of the higher opacity of this wind, it is necessary to cut off the power-law distribution of line strengths at a smaller value than for the low-density wind models of the previous

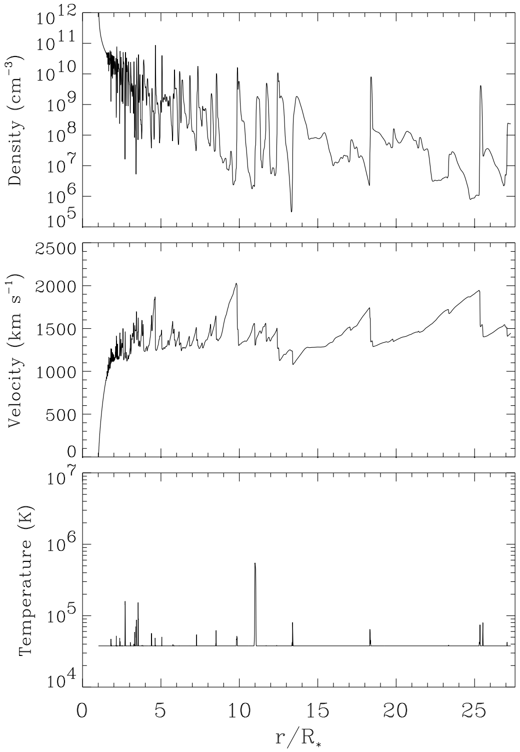

(a) Eulerian plot. Postshock cooling regions are unresolved.

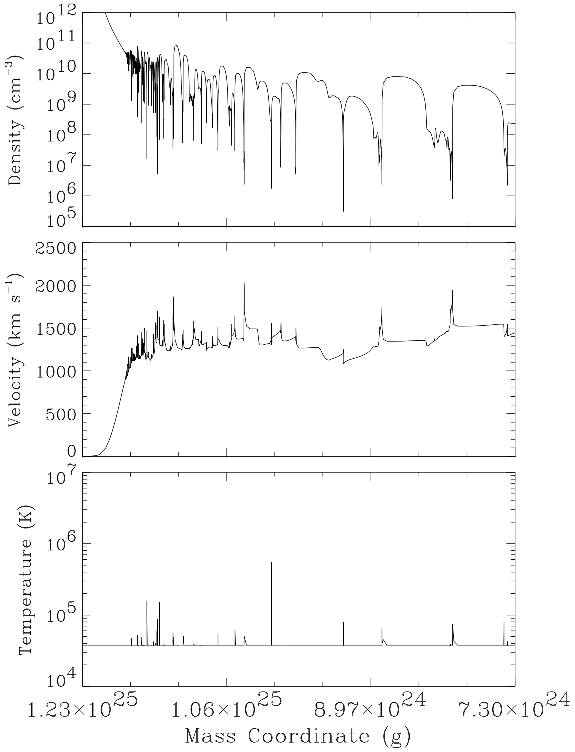

(b) Lagrangian plot.

Figure 6.1: Standard model for high-density (ζ Pup-type) winds, at time $t = 500$ ksec.

chapter, to prevent runaway acceleration by a small number of extremely strong lines. (See Section 2.2.) For all the models discussed here, we use $\kappa_{max}/\kappa_0 = 10^{-3}$; this is the value used in previously published isothermal models, *e.g.,* OCR.

Finally, models of a larger star must be run for a longer time. The flow time $t_{flow} = R_*/v$ is longer: the stellar radius R_* is about three times as large, while a typical wind velocity v is the same or somewhat smaller. And the numerical grid extends for more stellar radii, as discussed above. So it takes wind material longer to travel across the numerical grid, and the wind model takes longer to reach an approximate steady state that does not depend strongly on the model's initial state. The flow time for these models is $t_{flow} \sim 6$ ksec (compared to perhaps 1.5–2 ksec for the models in Chapter 5). Because velocities near the base of the wind are low, material takes on the order of 250 ksec to travel across the entire grid width of 26 R_*.

We have found that the line-driving instability is strong enough in high-density winds that strong shocks and a highly structured wind form, even when no explicit perturbation is introduced at the base of the wind. (Perturbations from numerical roundoff error, and from any departure of the model's initial state from equilibrium, are sufficient to "seed" the growth of such instabilities, and the fluctuations are then self-perpetuating.) Therefore in the standard model shown here, no explicit perturbation is applied.

6.2.2 Hydrodynamical results

Model results after evolution for 500 ksec (about 6 days) appear in Figure 6.1. A number of strong shocks are evident. However, as expected from the high wind density, cooling is rapid enough that the hot postshock regions are confined to very narrow spikes; these are only a few numerical zones wide, and thus unresolved. It is therefore not practical to calculate a model spectrum directly from the model temperature and density, and we use the sudden approximation (Section 3.5) instead.

As we found for lower-density winds, the shocks that form are characteristically *reverse* shocks. Before entering a strong shock, material gets strongly accelerated. As a result, the preshock material is rarefied, so that the mass flux into the shock is low, and only a small fraction of the wind goes through a strong shock.

6.2.3 Locations of strong shocks

Figure 6.2 shows the locations and amplitudes of shocks in the wind at the time of Figure 6.1. Strong shocks of 200 km/s or more develop low in the wind, sometimes as low as $r = 1.3 R_*$. Shocks of all strengths are more numerous low in the wind; the number of shocks decreases higher in the

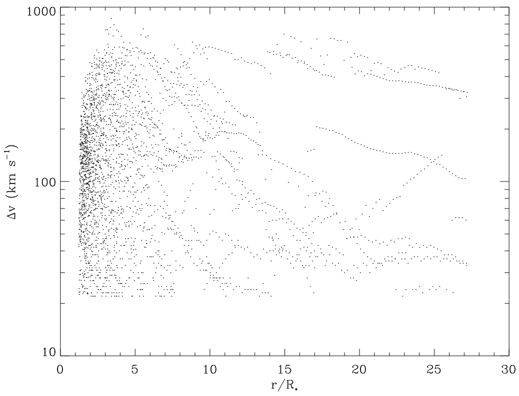

(a) Shocks occurring in the modeled region during the time $t = 400 - 500$ ksec. Data are plotted at 2-ksec intervals.

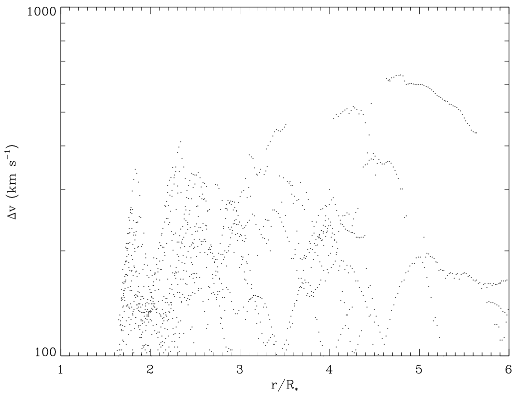

(b) Closeup of the inner wind region. Data shown here are from times $t = 500 - 510$ ksec, plotted at 0.2-ksec intervals.

Figure 6.2: The locations and strengths of shocks in the wind, plotted at regular times during the intervals indicated.

wind, as nearby shocks merge. The relative number of strong and weak shocks, however, shows no obvious trend with radius—the proportion of each remains approximately constant as all the shocks propagate outward.

6.3 Effects of Attenuation

With a model of the state of the wind at a specified time, we can now estimate the flux of X-rays emitted by shocked material within the wind. However, the absorbing column of wind material is large enough to significantly alter the spectrum of X-rays that emerge from the top of the wind. So we must account for this self-attenuation by the wind before comparing spectra to observations.

6.3.1 Cross sections

As an approximation to the absorption cross sections for X-ray photons, we use the formula given by Morrison and McCammon (1983). This formula gives the total cross section (per H atom) as a function of energy, assuming a solar-abundance mix of elements.

Since the formula was derived by fitting the results of calculations for attenuation by interstellar matter, it also assumes that all elements are neutral. This is clearly not the case in hot star winds. However, the total cross section depends strongly on the ionization state only below about 0.6 keV, as discussed below. In this work we emphasize models and observations above this range.

Neutral hydrogen and helium, almost nonexistent in hot star winds, would contribute a substantial fraction of the total only at energies below the oxygen edge at about 0.6 keV (see below). Singly-ionized helium can also be important at these energies, and it may be present in the outer wind (Hillier *et al.* 1993). If He II is present, the X-ray photosphere (the distance at which the optical depth through the overlying wind $\tau = 1$) lies within our modeled region only for energies above 300–400 eV. Because these models do not address the question of ionization balance, we have concentrated on comparing model spectra to observations at higher energies—especially the BBXRT observations (Corcoran *et al.* 1993), since BBXRT has better energy resolution than the ROSAT PSPC.

At energies above 500 eV, the largest contributions to the total cross section are from photoionization of K-shell electrons in heavier atoms: C, N, O, Fe, etc. The ionization state of these elements does not affect the total cross section very much, except that the energies of the absorption edges can shift by 5–10%; for example, the oxygen K-shell edge occurs at 0.53 keV for neutral oxygen, but at 0.67 keV for O VI. This will be an interesting question for the next generation of X-ray observations, *e.g.,* with ASCA, (and for the next generation of models), but the edges have not been resolved by the observations that are presently available.

6.3.2 Attenuation within the modeled region

Within the part of the wind covered by the numerical grid, we estimate the attenuation as follows. The wind column depth N radially outward above radius r is

$$N(r) = \int_r^\infty n(r')dr', \tag{6.1}$$

so the column depth N_{grid} to the outer edge R_{max} of the grid is

$$N_{grid}(r) = \int_r^{R_{max}} n(r')dr', \tag{6.2}$$

If the contribution to the *emitted* luminosity at energy E, from material at radius r, is $dL^0_{em}(E,r)$, then the contribution to the *observed* luminosity $dL^0_{obs}(E,r)$, if all photons emitted at distance r from the star passed through the same column $N_{grid}(r)$, would be

$$dL^0_{obs}(E,r) = dL^0_{em}(E,r)e^{-\tau(E,r)}, \tag{6.3}$$

where

$$\tau(E,r) = \sigma(E)N_{grid}(r) \tag{6.4}$$

and $\sigma(E)$ is the absorption cross section at energy E, assumed to be given by the interpolation formula in Morrison and McCammon (1983).

We do not consider any possible multiple scattering, nor do we consider the effect of the absorbed X-ray photons on the local state of the wind.

For the spherical geometry assumed in these models, we should calculate the emergent flux by integrating the contributions from all parts of the wind to the total flux along our line of sight—*i.e.,* we should obtain a formal solution of the radiative transfer equation for the X-ray photons. Photons originating anywhere in the wind other than along the line of sight through the center of the star must pass through a larger absorbing column. So the column N_{grid} calculated above is actually a lower limit to the column through which radiation from material at distance r from the star must pass to reach us.

Given the approximate nature of these estimates of attenuation, instead of calculating the emergent intensity along many rays and integrating, we simply assume that the average optical depth τ_* encountered by X-rays from all material at distance r from the star, along our line of sight, is (Rybicki and Lightman 1979, p. 44)

$$\tau_*(E,r) = \sqrt{3}\,\tau(E,r,\mu=1). \tag{6.5}$$

This is an approximate "two-stream" or "single ray" solution, giving a rough average over rays from locations around a spherical shell at radius r.

With this approximation, the contribution to the X-ray luminosity from all material at distance r from the star is

$$dL_{obs}(E,r) = dL_{em}(E,r)e^{-\tau_*(E,r)}, \tag{6.6}$$

and the total luminosity at photon energy E is

$$L_{obs}(E) = \int_{R_{min}}^{R_{max}} dL_{obs}(E,r)\,dr. \tag{6.7}$$

6.3.3 Attenuation by material above the modeled region

We can make a rough estimate of the attenuation by the wind above the upper edge of our model grid by calculating the column depth in a smooth CAK wind with the same mass loss rate and terminal velocity. We assume that the wind velocity is described $v(r)$ by a beta law (Groenewegen and Lamers 1991):

$$v(r) \simeq v_\infty \left(1 - \frac{R_*}{r}\right)^\beta, \tag{6.8}$$

where v_∞ is the terminal velocity, R_* is the stellar radius, and β is a constant. Pauldrach *et al.* (1993) find that β lies between 0.8 and 1.0; we use $\beta = 1$. For this (assumed) smooth, time-independent part of the wind, mass conservation requires that

$$\dot{M} = 4\pi r^2 v(r)\rho(r), \tag{6.9}$$

where $\dot{M}$ is the (constant) mass loss rate, and $\rho(r)$ is the mass density at radius r. So the number density $n(r)$ is

$$\begin{aligned} n(r) &= \frac{\rho(r)}{\mu} && (6.10)\\ &= \frac{\dot{M}}{4\pi\mu r^2 v(r)} && (6.11)\\ &\simeq \frac{\dot{M}}{4\pi\mu r^2 v_\infty\,(1 - R_*/r)}. && (6.12)\end{aligned}$$

In the current case, $r > 27R_*$, so that $v(r)$ is always very close to v_∞ (96% or more). So we may simplify the above equation to

$$n(r) \simeq \frac{\dot{M}}{4\pi\mu r^2 v_\infty}. \tag{6.13}$$

The wind column depth N_{above} above the upper edge of the model grid is then approximately

$$\begin{aligned} N_{above} &= \int_{R_{max}}^{\infty} n(r)dr && (6.14)\\ &\simeq \frac{\dot{M}}{4\pi\mu v_\infty}\int_{R_{max}}^{\infty}\frac{dr}{r^2} && (6.15)\\ &\simeq \frac{\dot{M}}{4\pi\mu v_\infty R_{max}}. && (6.16)\end{aligned}$$

For $\dot{M} = 3 \times 10^{-6}\ \dot{M}$/year and v_∞= 2000 km/s, this gives an overlying column

$$\begin{aligned} N_{above} &\simeq 4 \times 10^{22} cm^{-2}\left(\frac{R_*}{R_{max}}\right) && (6.17)\\ &\simeq 1.5 \times 10^{21} cm^{-2} && (6.18)\end{aligned}$$

for $R_{max} = 27R_*$. Notice that this is a small fraction of the total wind column: for example, it is less than 2% of the column down to $r = 1.5R_*$.

To estimate the total attenuation by wind material, we can simply replace $N_{grid}(r)$ with

$$N_{wind}(r) = N_{grid}(r) + N_{above} \tag{6.19}$$

in Equation 6.5 to find the total optical depth $\tau_{*(total)}(E, r)$,

$$\begin{aligned} \tau_{total}(E, r) &= \sqrt{3}\,\tau_{total} && (6.20)\\ &= \sqrt{3}\,\sigma(E)N_{wind}(r). && (6.21)\end{aligned}$$

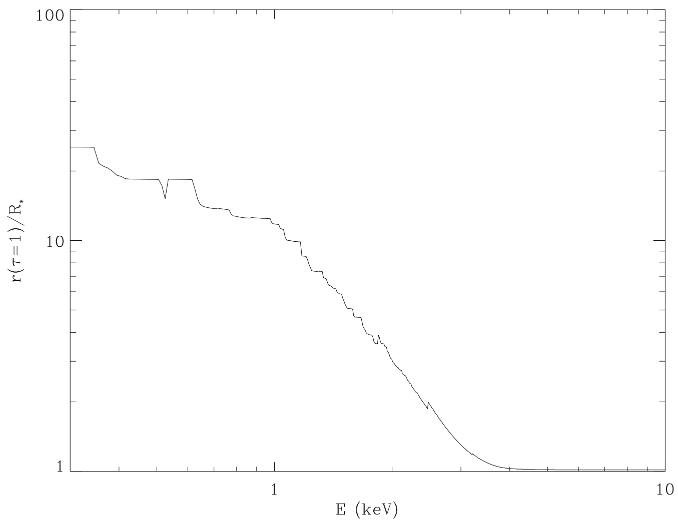

Figure 6.3: The radius at which optical depth $\tau = 1$ occurs. Below about 0.3 keV, the wind is optically thick even above the region included in the model grid.

6.4 Optical depths for different X-ray energies

Using the cross sections described in Section 6.3.1 and the above expressions for the column depth, we can use Equation 6.4 to find the optical depth $\tau(E, r)$. Inverting Equation 6.4, we can find the distance from the star at which optical depth $\tau = 1$ occurs, for each energy E.

The result for material within the model grid appears in Figure 6.3. The dense wind of ζ Pup is optically thick at nearly all X-ray energies observed by *Einstein*, ROSAT, or BBXRT, but much more so at lower energies. Optical depth $\tau = 1$ occurs at about $r = 17R_*$ for 0.5 keV photons; at about $r = 12R_*$ for 1.0 keV photons; and at about $r = 2R_*$ for 2.0 keV photons. So shocked material low in the wind affects mainly the high-energy end of the spectrum, while the low-energy part of the emergent spectrum comes primarily from hot material well up into the wind.

These values are approximately consistent with the results of Hillier *et al.* (1993) for an unstructured, smooth wind. (See their Figure 1.)

6.5 Model Spectra

We can now calculate the emergent X-ray spectrum from a model wind state, such as that of Figure 6.1; Spectra calculated from these models turn out to be rather variable, a point that will

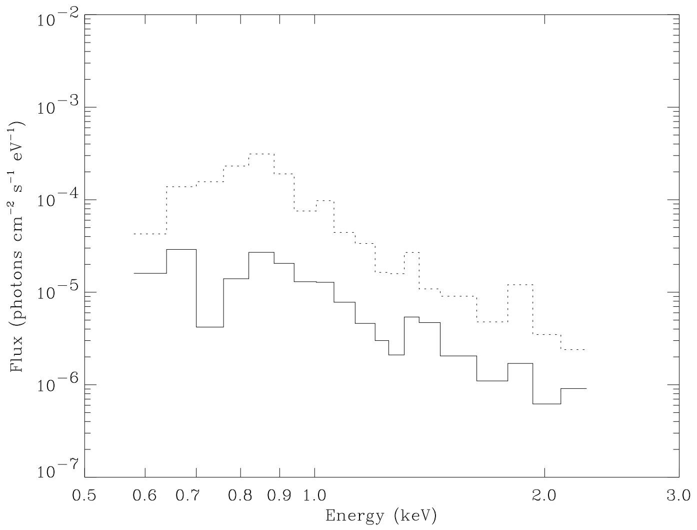

Figure 6.4: X-ray spectrum for the model shown in Figure 6.1; average of model spectra for times from $t = 400 - 500$ ksec (see text). Solid line shows the observed spectrum (Corcoran *et al.* 1993); dotted line shows the model spectrum.

be discussed further in Section 6.6. For this reason, the model spectra displayed here represent averages over model states from time $t = 400$ to 500 ksec. The standard model spectrum is shown in Figure 6.4. The model spectrum (dotted line in the figure) was calculated using the sudden approximation, and includes attenuation by overlying material within the modeled part of the wind. The observed spectrum (solid line) is the best fit obtained by Corcoran *et al.* to their BBXRT observations of ζ Pup.

As we saw for thin-wind models, the *shape* of the model spectrum agrees reasonably well with that of the observed spectrum. However, in this case the model luminosity lies *above* the observed value: $(L_{\rm x})_{mod} \simeq 10 \times (L_{\rm x})_{obs}$.

To illustrate the effect of attenuation within the wind, in Figure 6.5 we show three successive model curves, in addition to the observed spectrum (solid line). The top (dashed) curve is the model X-ray spectrum with no attenuation—thus, the emitted, rather than the emergent, spectrum. The second (dash-dot) curve includes attenuation by material in the modeled region, $r = 1 - -27R_*$; this is the same as the model spectrum shown in Figure 6.4. Finally, the third (dotted) curve adds attenuation by overlying wind material, *i.e.,* from $r = 27R_*$ to ∞. Attenuation affects the emergent spectrum significantly—far more than in a low-density wind, as we would expect. But

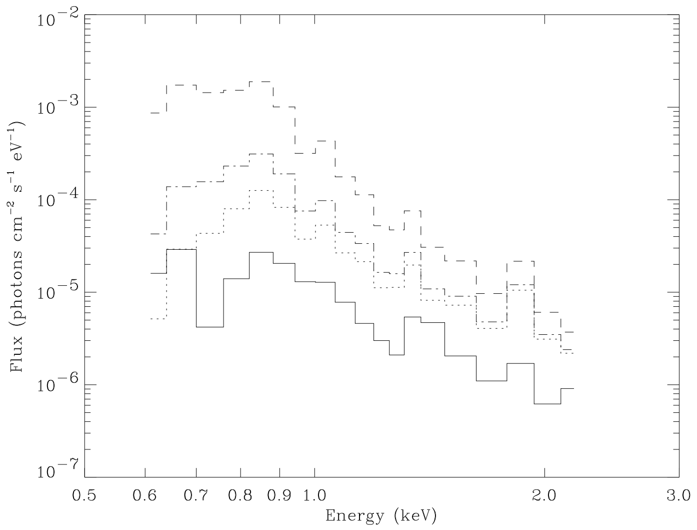

Figure 6.5: X-ray spectrum for the model shown in Figure 6.1. Solid line: observed spectrum (Corcoran *et al.* 1993); dashed line: model spectrum with no attenuation; dash-dot line: model spectrum with attenuation by the modeled region; dotted line: model spectrum with attenuation by the modeled region plus estimated overlying wind material.

even here, the reduction is only by a factor of 1.5–100, with factors of a few typical over much of the energy range shown, 0.5–3 keV. Since the lowest curve includes attenuation by overlying material, but no emission by the same material, it represents roughly a lower limit to the emergent L_{x} for this model.

The ratio $(L_X)_{emergent}/(L_X)_{emitted}$ is about 0.24 for the interval from 0.5 to 2.5 keV, or about 0.14 between 0.1 and 2.5 keV, for the modeled region; *i.e.,* we see only on the order of 15% of the X-rays emitted by the wind. If we include attenuation by the overlying "upper" wind, the ratio drops to 0.085 for 0.1–2.5 keV.

To further examine the competing effects of added attenuation and added emission in higher layers of the wind, we can look at the spectrum resulting from only the inner wind ($r = 1 - 10R_*$), and compare that to the spectrum from the entire modeled region $r = 1 - 27R_*$. This is shown in figure 6.6, where the center (dotted) curve shows the model spectrum that would result if we include only the emission and attenuation from material between $r = 1$ and 10 R_*, and the upper (dashed) curve shows the model spectrum from material out to 27 R_*. (The lower, solid line shows the observed spectrum, as before.) The extended range 10–27 R_* adds only about 50% to the total

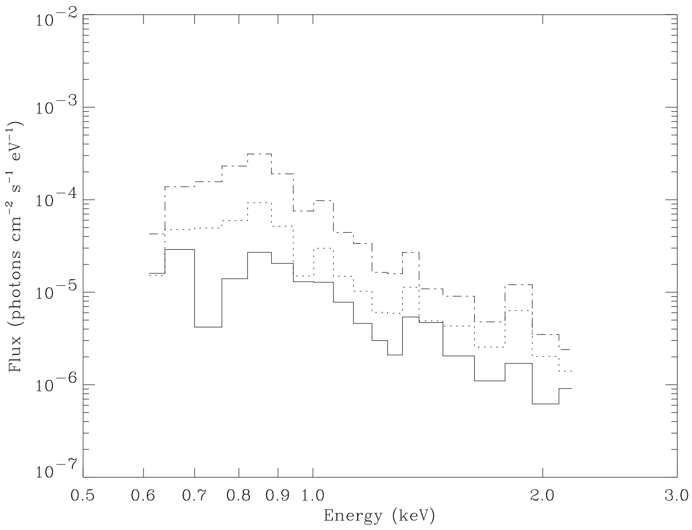

Figure 6.6: X-ray spectrum from modeled regions extending from $r = 1 - 10\ R_*$ (dotted line) and $r = 1 - 27\ R_*$ (dot-dash line). Solid line is observed spectrum, as in Figure 6.5.

wind column, and at the same time adds a significant amount of X-ray emission; the emergent spectrum is almost identical at high energies, and slightly higher at low energies. Extending the grid even farther would add relatively little attenuation, as we saw in Figure 6.5, and will partially compensate for this additional attenuation with added emission. So the present range for the modeled region should produce a fairly representative model X-ray spectrum, for energies above 0.6 keV.

6.6 Time Variability of L_x

6.6.1 Variability in X-ray observations

As was the case for other hot stars, observations of ζ Pup have generally found either that the X-ray luminosity of ζ Pup was not variable, or that it varies with a relatively small amplitude. However, each result is based on a relatively small number of observations, so that the limits on observed variability are still fairly wide.

Collura *et al.* (1989) tested *Einstein* IPC observations of ζ Pup for variability. They found that the soft band (0.2–0.8 keV) varied by 40% or more over time scales of days, while the hard band (0.8–4.5 keV) varied by no more than 10% over the same time scales. Over shorter periods, they found only upper bounds: the hard and soft bands vary by no more than 15–25% over time scales of seconds to hours.

The ROSAT PSPC observations of ζ Pup described in Hillier *et al.* (1993) showed *no* variability above the photon noise, on time scales from seconds to a week (Baade, private communication).

6.6.2 Variability of modeled X-rays

The X-ray luminosity $L_{\rm x}$ predicted by a one-dimensional model might well show higher variability than is actually observed. Each shock in the model is interpreted to extend uniformly over a spherical surface, while the actual wind probably has many more shocks, each with limited angular extent. So the observed X-rays probably result from a larger number of shocks, and thus presumably have smaller fluctuations in the total $L_{\rm x}$. On the other hand, comparing the observed variability to that of one-dimensional models might in principle provide limits on the number of these smaller-angle shock fronts that is required, and thus on the angular extent of typical shocks.

The model $L_{\rm x}$ does show large fluctuations with time. Figure 6.7 shows the luminosity in the band 0.5–4.5 keV, over a span of 250 ksec ($t = 250 - 500$ ksec), for the standard model. The luminosity varies by a factor of up to 100, and by factors as large as 5–10 over short (2 ksec) time scales.

6.6.3 Sources of variability in $L_{\rm x}$

Considering the large number of shocks present at any time even in the 1-D models (see Figures 6.1 and 6.2), it might seem surprising that the total X-ray luminosity is so variable. But the total flux is dominated by emission from material heated by a small number of shocks—sometimes only one or two. Any change in either the strength of one of these key shocks, or the preshock density (thus the mass flux into the shock) is reflected in a change in $L_{\rm x}$.

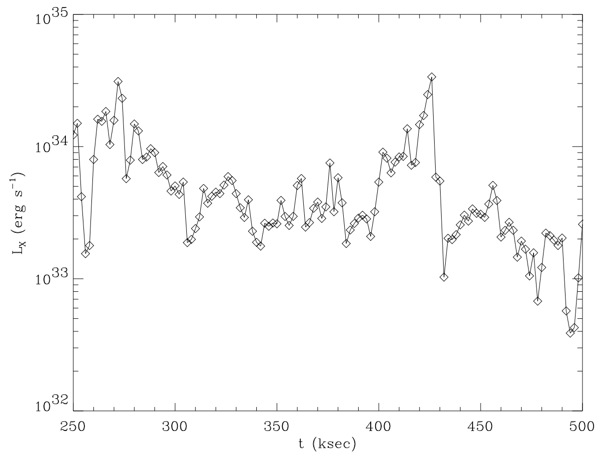

Figure 6.7: Variation of $L_{\rm x}$ during the interval t = 250—500 ksec. The luminosity varies by factors of 5 to 100, over time scales of 2–100 ksec.

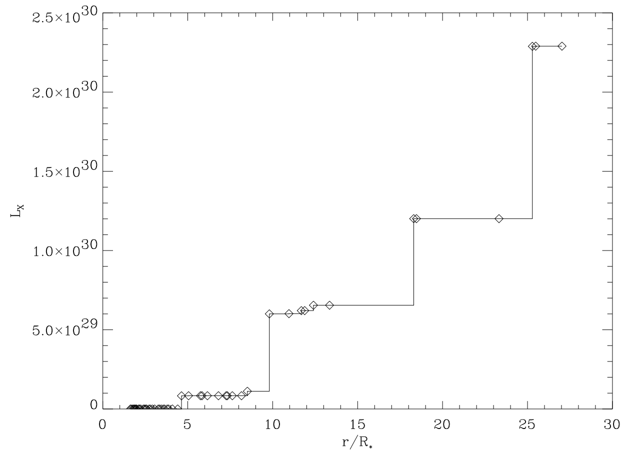

Figure 6.8: Total emergent $L_{\rm x}$ from all material below radius r, at the same time t = 500 ksec shown in Figure 6.1. The large jumps occur at the locations of strong shocks that lie relatively high in the wind and have relatively large preshock densities.

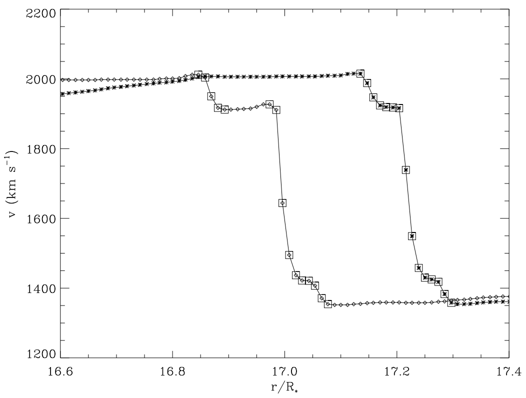

(a) Velocity structure.

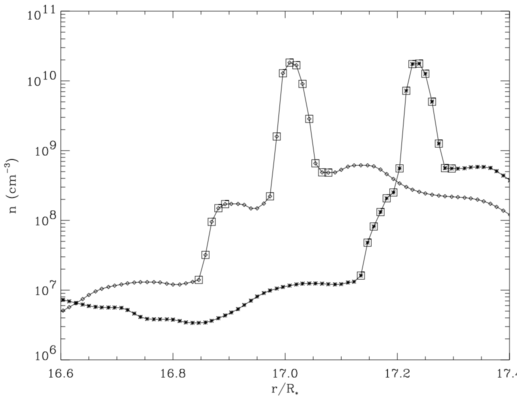

(b) Density structure.

Figure 6.9: A close-up look at one shock, at times t = 426 ksec (diamonds), and t = 428 ksec (stars). The two separate shocks seen at 426 ksec merge into one larger shock by 428 ksec. The second shock at 426 ksec has a somewhat smaller amplitude, but much larger preshock density $n_{\rm in}$ (10^8 vs $10^7 cm^{-3}$), than the single shock at 428 ksec; so the total luminosity $L_{\rm x}$ decreases.

This dependence of $L_{\rm x}$ on a small number of shocks is evident in Figure 6.8, which shows the total emergent X-ray luminosity between 0.50 and 0.51 keV at time t = 500 ksec, from all material below each radius. Most of the total comes from strong shocks at $r = 10R_*$, $18R_*$, and $25R_*$. (Several other strong shocks exist in the wind, but they lie deeper in the wind, so that most photons are absorbed on the way out.)

As Figure 6.7 shows, $L_{\rm x}$ varies on a timescale on the order of the flow time across the modeled region, perhaps 100–200 ksec; and also on a much faster time scale, sometimes jumping by a factor of 5 or even more over just 2 ksec.

The rapid changes are probably an artifact of the method used here. For example, the sudden drop in $L_{\rm x}$ seen from t = 426 ksec to 428 ksec in Figure 6.7 occurs because $L_{\rm x}$ is dominated at 426 ksec by emission from just one strong shock, together with a weaker, nearby shock. As shown in Figure 6.9, these two shocks merge into a single shock over the next two ksec. The result is a shock with a higher Δv; which would tend to *increase* $L_{\rm x}$. More importantly, however, the higher-density ($n_{\rm in} = 10^8 cm^{-3}$) material entering the second shock at 426 ksec has now disappeared, with only $n_{\rm in} = 10^7 cm^{-3}$ material entering the single shock at 428 ksec. So the estimated X-ray spectrum is slightly harder at 428 ksec, but the total estimated $L_{\rm x}$ is lower.

Besides cases like this, where two shocks become one, a single shock can also change fairly rapidly. This is especially true fairly low in the wind, in the acceleration region, where shocks are often still growing (and the radiation force from the star is relatively large), but it can also occur higher in the wind, where more of the emitted X-rays will actually emerge. In particular, the preshock density $n_{\rm in}$ can vary as denser and less-dense shells reach the shock.

If such changes in $n_{\rm in}$ (or in Δv) occur over a time shorter than the postshock cooling time $t_{\rm cool}$, then using the sudden approximation can exaggerate the change in $L_{\rm x}$. The sudden approximation assumes that the postshock region present at a selected instant matches that behind a steady-state shock with the same $n_{\rm in}$ and the same Δv. But if we could properly resolve the postshock cooling region, the effect on $L_{\rm x}$ of fluctuations in $n_{\rm in}$ would be "averaged" by the presence of still-hot material that went through the shock earlier, with a higher or lower density (or velocity jump) than that of material now entering the shock.

Combined with the probable presence in three dimensions of a larger number of shocks, each extending over only part of the spherical surface assumed in these 1-D models, we expect the amplitude of variability to be much smaller than that shown in Figure 6.7. However, it is difficult to predict more precisely how much smaller the model variability might be until we have better resolution of the postshock regions, or two- or three-dimensional models, or both.

Chapter 7

SUMMARY AND CONCLUSIONS

In Sections 7.1 through 7.3, I offer a brief review of the major parts of this work. Section 7.4 discusses some questions that remain regarding the source of X-rays observed from hot star winds, and some plans for future investigations extending the work begun here. Finally, a brief list of the conclusions reached in this work appears in Section 7.5.

7.1 Techniques for Resolving Postshock Cooling Regions

Material heated by passing through a shock has a characteristic cooling time $t_{\rm cool} \sim (nkT)/(n_e n_H \Lambda(T))$. If the shock persists for long enough, the postshock region reaches an equilibrium column density $N_{\rm cool} \sim 7 \times 10^{17} (v_s/100{\rm kms}^{-1})^4$ (Krolik and Raymond 1985). This corresponds to a cooling length $L_{\rm cool} \sim 6 \times 10^{11}{\rm cm}\ T_6^2\, n_8^{-1}$, where T_6 is the temperature in units of 10^6 K, and n_8 the density in units of $10^8{\rm cm}^{-3}$, of material that has just gone through the shock.

The cooling length varies over a wide range in winds with different densities, and for shocks with different strengths. First, consider a shock just strong enough to heat material to X-ray emitting temperatures ($T_6 \simeq 1$), lying relatively low in the wind of an early type supergiant, where $n_8 \simeq 100$. Then $L_{\rm cool} \sim 6 \times 10^9$ cm $\sim 0.005 R_*$. In this case, radiative cooling dominates, but $L_{\rm cool}$ is too short to resolve the cooling region with any reasonable grid, if the grid is also to extend a significant distance from the star. So in this sense, this is an isothermal shock.

At the other extreme, for a main sequence star around type B0, a strong shock with $T_6 = 10, n_8 = 0.1$ might reach $L_{\rm cool} \sim 6 \times 10^{14}$ cm $\sim 1300 R_*$. This means that radiative cooling is insignificant in such a shock, and the postshock material initially cools only by adiabatic expansion. In fact, cooling will be dominated by adiabatic expansion even for a weaker shock with $T_6 = 1$, for which $L_{\rm cool} \sim 13 R_*$.

Of course, even within a single wind there will be shocks with a range of postshock densities and temperatures, so that neither of the above limits applies wholly to the wind of any star. However, it is fair to say that a "typical" shock is more nearly isothermal in an early-type supergiant wind, and more nearly adiabatic in a late-type main sequence wind. I have taken advantage of these approximate limits to develop separate methods of estimating the X-ray emission from the two types of wind.

7.1.1 The sudden approximation

For the dense winds of early-type and supergiant stars, I assume all shocks to be isothermal: that is, I make the approximation that shocked material cools in a time shorter than the time required for the shock parameters to change, and also shorter than the time required for adiabatic expansion cooling. At a particular time, each shock in the wind may then be considered to be in a steady state, and the hot material behind the shock therefore emits the same X-ray spectrum that would result from a stationary, steady-state shock with the same amplitude and preshock density.

I have calculated these steady-state spectra for a range of shock parameters, and stored the results in a table. To calculate the X-ray spectrum emitted by a wind model at a given time, I identify the location, velocity jump, and preshock density of each shock; look up from the table the spectrum emitted by a shock with these parameters; modify this spectrum to account for attenuation by overlying wind material; and add the result to the total from other shocks.

7.1.2 Model spectra from adiabatic models

In the relatively low-density winds of late O / early B main sequence stars, typical postshock cooling regions should be wide enough to resolve well. But, for reasons explored in Chapter 3, numerical models that include radiative cooling miss a significant amount of the hot, X-ray emitting material.

Since radiative cooling is not the primary cooling mechanism in these winds for the strong shocks that make X-rays, I have simply calculated wind models using only adiabatic cooling. This distorts the structure of cooler regions, where radiative cooling should be important, but should not affect the hotter X-ray emitting regions too badly. With this approximation, the hot regions are well resolved on the numerical grid, and I can then calculate the emitted X-ray spectrum directly, using the model temperature and density at each point in the wind.

7.2 Results for Low Density Winds: Late O or Early B Stars

I compared observations of the X-ray spectra of μ Col (type O9.5 V) and τ Sco (B0 V) to model spectra calculated from time-dependent wind models that used stellar parameters appropriate to this spectral type. Although τ Sco is perhaps the most extensively studied of stars in this spectral range, it may be rather atypical in its X-ray properties, with both higher total X-ray flux and a harder spectrum than other such stars (Cassinelli *et al.* 1994, hereafter CCMSW). The spectrum of μ Col, on the other hand, appears quite similar to those of other stars with nearby spectral types, and therefore I use it as a more nearly typical representative.

As discussed in Section 7.1, I use adiabatic models (with no radiative cooling) for these stars. The principal result is that thermal emission from shocks produced by the line driving instability can account for the observed X-rays only under fairly restrictive conditions, if at all. Model spectra reproduce (roughly) the observed spectral shapes rather naturally, but the simplest models typically have total X-ray luminosity $L_{\rm x}$ below the observed $L_{\rm x}$, often by a factor of 10 or more.

CCMSW have noted that, beginning at about this spectral type, stars show emission measures of hot ($> 10^6$ K) material that represent substantial fractions of all wind material. In some ways, this might not be too surprising. The relatively low-density winds of these stars might be expected to have a relatively high fraction of hot material, since the cooling times are long: any material that does get heated to X-ray emitting temperature essentially stays hot. Also, these winds are optically thin at photon energies down to 0.3–0.5 keV; so most of the X-rays produced escape to be observed.

But the nature of the line driving instability makes it difficult to heat a large fraction of the wind to high temperature. Although a number of strong shocks develop, the shocks are typically preceded by a region of strong acceleration, with resulting strong rarefaction. So material enters a strong shock at low density, and the mass flux into the shock is small; in fact, only about 5% of wind material goes through a shock with the minimum postshock temperature $T_{shock} \geq 10^6$ K required for significant X-ray emission, in a typical model (see Chapter 4).

As a result, the model x-ray luminosity $L_{\rm x}$ is normally well below the observed $L_{\rm x}$, not only from τ Sco, but also from μ Col. To reproduce the X-ray flux (and spectral shape) seen in μ Col and similar stars requires enhancing the growth of instabilities low in the wind, where the density is high. For example, if the density at the base of the wind varies by 25% over a period of about an hour, then the resulting model spectrum is in good agreement with the observed spectrum of μ Col (see Figure 5.6(a)).

The only case I have seen in which the model X-ray flux reaches the value observed in τ Sco may be a numerical artifact rather than a true physical prediction. In certain cases the wind instability can reach all the way to the base of the modeled wind. When this happens, the wind can switch to a smooth velocity law with a new, higher v_∞. This fast wind then overtakes material in the overlying slower wind, with the result being a strong *forward* shock. A large fraction of wind material then goes through this forward shock, generating a large emission measure of X-ray emitting material. The model X-ray spectrum can then match the observed, high-L_x spectrum of τ Sco (see Figure 5.8).

So, if conditions near the base of the wind vary enough that the wind density changes by a significant fraction, perhaps 20% or more, then these models suggest that material heated by instability-generated shocks may emit the observed X-rays, at least in "typical" stars such as μ Col; and if conditions change even more strongly, this mechanism may be able to account for the stronger X-ray emission from τ Sco. Note that these variations at the wind base would not necessarily have to extend simultaneously over the entire stellar disk, but might be limited in longitude or latitude, so that global wind parameters such as $\dot{M}$ and v_∞ might show much less variation.

If this sort of variability in the density or other parameters near the base does not occur, then these models suggest that the line driving instability may not be enough, and some other mechanism(s) may be responsible for some, or even most, of the X-ray emission.

One possibility may be the comoving interaction regions (CIR's) proposed by Mullan (1984, 1986), in analogy with the regions observed in the solar wind. If there are longitudinal variations in the radial wind speed, then as the wind moves outward, the fast wind sectors catch up to the slower ones, with the resulting shocks and density enhancements forming a spiral pattern in the wind. This might help to account for the indication that the discrete absorption components described in Chapter 1 recur on a time scale related to the star's rotation period (Prinja *et al.* 1990). Calculations of X-ray emission from this process require two-dimensional wind models, for which work is in progress.

Finally, we can compare the variability of L_x in model and observed spectra. Model spectra show variations in L_x by as much as a factor of 2 on a time scale as short as 1 ksec, and by a factor of 5 over 10 ksec. Observations, on the other hand, show variability of no more than 30% for τ Sco, and no variability was seen in μ Col. This discrepancy may arise simply from using one-dimensional models: each shock is assumed to extend over an entire spherical shell, while the wind may actually have many shock fragments, each covering only a small solid angle. It may be possible to use this argument to place limits on the number of shock fragments and their angular extents. A better answer, of course, will be provided eventually by two- or three-dimensional wind models.

7.3 Results for High Density Winds

X-ray emission from the dense winds of early-type and supergiant stars such as ζ Pup presents a dilemma opposite that presented by the stars discussed in Section 7.2: in high density winds, only a small fraction of the total wind mass must be hot to emit the observed flux of X-rays, and model spectra easily reach the observed L_x. In fact, model spectra are typically *higher* than observed by a factor of 5–10, in the modeled range above 0.5 keV. (I use the sudden approximation method to calculate spectra for these models.)

This discrepancy is less clear than in the previous case, because there are several sources of uncertainty that were less important in low density winds. First, attenuation of X-rays by overlying wind material plays a larger role in a high density wind. Because these models do not address ionization balance, attenuation at energies below about 0.5 keV—which is dominated by H and He, if they are present—is very uncertain. Above 0.5 keV, attenuation comes mainly from K-shell absorption by C, N, O, and other metals, and the cross section is nearly the same for any of the likely species (*e.g.,* O IV, O V, and O VI); so that a reasonable estimate of attenuation is possible over the modeled region. But, since current models extend no farther than 25 R_*, some question remains as to the effect of material above this point: it will cause extra attenuation, but also some extra X-ray emission, and it is not clear which effect will be larger.

Also, the sudden approximation may not be entirely justified, even though the density is high enough that cooling times are relatively short. Because preshock material is rarefied, postshock cooling times can be significantly longer than an initial estimate would suggest. The sudden approximation will still be valid if the shock parameters (amplitude and preshock density) do not change much over this longer cooling time, and that is more or less the case for most of the shocks that are present at a particular time. Nevertheless, the net effect is that the sudden approximation tends to overestimate the X-ray flux, potentially by a significant factor.

As in the case of low density winds, the model X-ray spectra show much higher variability than is observed. However, this difference is probably not significant. Besides the effect of assuming that each shock extends over all 4π steradians, as discussed in Section 7.2, the sudden approximation method exaggerates the effect on the X-ray spectrum of a small change in the properties of a shock, since this method always assumes that the postshock cooling region has the form it would have if the shock were in an exact steady state.

7.4 Directions for Future Work

7.4.1 Why is $L_{\mathrm{x}}/L_{\mathrm{bol}}$ nearly constant?

The X-ray luminosities of O and early B stars are approximately linearly proportional to the bolometric luminosity (Sciortino *et al.* 1990):

$$\log L_{\mathrm{x}} = 1.08^{+0.06}_{-0.22} \log L_{\mathrm{bol}} - 9.38^{+2.32}_{-0.83}, \tag{7.1}$$

or

$$log(L_{\mathrm{x}}/L_{\mathrm{bol}}) \simeq -6.46, \tag{7.2}$$

where L_{x} here is the luminosity integrated over the *Einstein Observatory* IPC bandpass, roughly 0.2–2.5 keV. (However, this relationship does not appear to extend to main sequence stars of types later than about B1, for which $L_{\mathrm{x}}/L_{\mathrm{bol}}/$ decreases to 10^{-9} or less; see CCMSW.)

At least at first glance, this result is surprising, since the mass loss rate $\dot{M}$ varies more rapidly with L_{bol}(Howarth and Prinja 1989):

$$\dot{M} \propto {L_{\mathrm{bol}}}^{1.69}. \tag{7.3}$$

Therefore, if the shocks produced by the wind instability simply heat the same fraction of material, with the same range of temperatures, in all hot star winds, then L_{x} should be proportional to $\dot{M}$, and $L_{\mathrm{x}} \propto \dot{M} \propto {L_{\mathrm{bol}}}^{1.69}$.

On the other hand, a smaller fraction of the emitted X-rays will actually be observed in the denser winds of early-type stars, because attenuation of the X-rays by wind material will be greater. For example, in the low-density wind models discussed in Chapter 5, about 90% or more of the X-rays above 0.5 keV originally emitted by the wind emerge to be observed; in the higher-density models of Chapter 6, the figure is only about 10%. The ratio of bolometric luminosities for the two models is $(L_{\mathrm{bol}})_{\mathrm{high}}/(L_{\mathrm{bol}})_{\mathrm{low}} = 6.9 \times 10^5 L_\odot / 3.3 \times 10^4 L_\odot \simeq 21$.

If we define the fraction $f_{\mathrm{emergent}} \equiv (L_{\mathrm{x}})_{\mathrm{emergent}}/(L_{\mathrm{x}})_{\mathrm{emitted}}$ of emitted X-rays that actually emerge from the wind, the above values suggest a dependence

$$f_{\mathrm{emergent}} \propto {L_{\mathrm{bol}}}^{-0.7}, \tag{7.4}$$

so that

$$\begin{aligned} (L_{\mathrm{x}})_{\mathrm{observed}} &\sim (L_{\mathrm{x}})_{\mathrm{emergent}} && (7.5)\\ &\propto f_{\mathrm{emergent}}\,(L_{\mathrm{x}})_{\mathrm{emitted}} && (7.6)\\ &\propto {L_{\mathrm{bol}}}^{-0.7}{L_{\mathrm{bol}}}^{1.69} && (7.7)\\ &\propto {L_{\mathrm{bol}}}^{0.99}, && (7.8) \end{aligned}$$

in agreement with the roughly linear dependence found by Sciortino *et al.* (1990). So these two data points, at least, are consistent with a simple picture in which X-ray emission is proportional to $\dot{M}$, and the observed X-rays reflect the emitted flux folded through attenuation that depends in a more complicated way on $\dot{M}$.

Because the wind attenuation is very different at different energies, and also because different detectors have different bandpasses, the traditional comparison of an integrated $L_{\rm x}$ to $L_{\rm bol}$ may not be the most useful comparison to make. Instead, or perhaps in addition, it would be useful to report the observed luminosity per eV at each of several energies—*e.g.,* at 0.2, 0.5, and 1.0 keV.

7.4.2 The resolution problem

The techniques I have described to get around the difficulty in resolving postshock cooling regions allow gross estimates of the X-ray emission, but they leave much to be desired. Using either adiabatic models or the sudden approximation requires making strong assumptions about cooling rates. I have argued that the errors thus introduced are not too severe if the wind density is low enough (for adiabatic models), or high enough (for the sudden approximation); but it would clearly be preferable to have a way to resolve the hot postshock regions, while still allowing the cool, dense shells to form.

7.4.2.1 Feldmeier's modification of the radiative cooling function $\Lambda(T)$

Feldmeier (1993, 1994) has developed a promising method to eliminate the numerical part of the resolution problem, so that modeled hot regions can at least be resolved when physical constraints make the cooling length long enough. He argues that the numerical difficulties in properly resolving this region do not stem primarily from numerical interpolation coupled to increased cooling, as I argued in Chapter 3.

Instead, the problem is a result of the global thermal instability of radiating shocks (Section 2.6.2). Feldmeier reports that, when a strong shock advects rapidly across the numerical grid, the postshock cooling region is well resolved from the beginning of the calculation until about one cooling time later. This is when the hot region begins its collapse as a result of the instability, and it does so for the advecting shock. In a model with the same shock stationary on the grid, the cooling region then grows again for one cooling time, then collapses again, and so forth. But with the advecting shock, the numerical code can no longer resolve the (initially) thin layer of hot material next to the dense layer of cooled material, and the hot region never reappears.

To prevent this behavior, Feldmeier modifies the form of the radiative cooling function $\Lambda(T)$ below a "switch" temperature $T_{\rm swi}$ so that

$$\Lambda(T) \propto T^2, \quad T < T_{\rm swi}, \tag{7.9}$$

while $\Lambda(T)$ remains unchanged for $T > T_{\rm swi}$. (Recall that the postshock cooling zone is unstable if $\alpha \lesssim +0.4$, where $\Lambda(T_s) \propto T^\alpha$, and T_s is the immediate postshock temperature.) Feldmeier typically uses $T_{\rm swi} = 15 T_{\rm eff} \simeq 6.3 \times 10^5$ K for models of ζ Pup. This means that α changes from about -0.5 to +2 between about $T = 10^5$ K and $T = T_{\rm swi}$ ($\alpha \simeq +2$ below about $T = 10^5$ K already). Also, the magnitude of $\Lambda(T)$ is reduced by about a factor of 200–250 at temperatures below $T = 10^5$ K, and by smaller factors up to $T_{\rm swi}$.

Models that had unresolved postshock cooling regions with unmodified radiative cooling show the same regions nicely resolved with the new cooling function. Importantly, the dynamical processes in the wind are largely unaffected by using the $T_{\rm swi}$ version: shocks and other structures form at nearly the same locations, with nearly the same magnitudes, as in models with the unaltered cooling function. In contrast, adiabatic models show considerable change in the wind structure compared to models with standard radiative cooling, especially above the first few stellar radii.

These results appear extremely promising, and may make possible substantially improved estimates of X-ray emission and other diagnostics. However, preliminary efforts to duplicate Feldmeier's results with our numerical code have been unsuccessful. Models run so far show little difference from models with $\Lambda(T)$ simply reduced by a factor of 100 or so; they do not achieve the dramatically improved resolution that Feldmeier sees, and the wind structure is altered more (compared to a model with the full cooling function) than in Feldmeier's results. An early priority is to resolve this discrepancy, and to try using the Feldmeier method in our models of X-ray emission.

7.4.2.2 Other possible techniques to improve resolution

At least two other types of numerical techniques might prove useful in improving the resolution of the X-ray emitting regions of the wind.

Perhaps the most common method used to maintain good resolution near shocks—for example, in models of supernova remnants— is to solve the equations of motion in Lagrangian form. In a Lagrangian numerical model, grid points are separated by specified mass intervals, rather than specified distances. So grid points concentrate where the density is high, and the postshock cooling regions and dense shells remain well resolved.

Similarly, adaptive mesh techniques can retain the equations of motion in Eulerian form, but adjust the numerical grid at each step to concentrate grid points in (for example) regions of high density. The grid could also be adjusted according to other criteria, for example to improve resolution in regions with large gradients in temperature or pressure.

We have not yet used either of these techniques, in part because of concern over the corresponding loss of resolution in other parts of the wind. The rarefied preshock acceleration regions, for example, would be represented by correspondingly few points as the points concentrate in the high-density regions. This makes it difficult to accurately follow the velocity gradient, which in turn determines the radiation force. Also, the very complexity of the wind structure will limit the effect of such methods: the number of grid points concentrated near any one shock cannot be too large, simply because there are typically dozens of shocks in the wind.

However, these concerns may prove to be less serious than the limitations of the current Eulerian, fixed-grid models, and I hope to experiment with both methods.

7.4.3 Investigating the ionization state of the wind

We have seen that the emergent X-ray spectrum, particularly at the soft X-ray energies $E_\gamma \lesssim 0.5keV$ where many main sequence stars are brightest, depends strongly on the amount of attenuation by overlying wind material. This attenuation, in turn, depends on the ionization states of the absorbing species, a question that the present models do not address. As a first step toward including ionization balance in the wind models, work is now underway to use the modeled wind structure in a separate (non-time-dependent) calculation of ionization balance.

The approach is similar to that described in MacFarlane *et al.* (1993). They calculate emergent X-ray spectra and ultraviolet line profiles from an assumed smooth wind model, with X-rays originating at several possible locations in the wind. Starting with this model, they calculate ionization balance and full radiative transfer for a large number of transitions. Thus their approach is the natural counterpart of the time-dependent models described in this work, which make a more realistic calculation of the wind state, but lack ionization balance and use only a simple attenuation model for the X-ray radiative transfer.

By combining the two approaches, we hope to get a clearer picture of observable diagnostics for the instability-shock origin of X-rays, while avoiding the very large amounts of computer time that would be needed by a full time-dependent model that also included full radiative transfer.

7.4.4 Other improvements to the physical description in wind models

The smooth source function (SSF) approximation makes it possible to include important physical effects such as the Lucy line drag force in a wind model, within available computer resources. But the primary assumption required by the SSF method—that the source function varies slowly compared to the optical depth—is not always entirely justified, especially near the very shocks that are responsible for X-ray emission. It is not clear how to take this into account without abandoning the SSF framework, but we hope to explore possible modifications.

Chen and White (1991) argued that particle acceleration at shocks can result in a significant population of high-energy particles and of hard X-ray and gamma-ray photons. Conversely, inverse Compton scattering can limit the growth of strong shocks, and thus the emission of moderate-energy (one to a few keV) X-rays. These effects have not been addressed in the models described here, but should be examined in future work.

Another piece of physics missing from the current models is thermal conduction, which for some conditions can substantially alter the structure of shocks, and thus the X-ray spectrum produced. The rate of conduction can be limited by the presence of a transverse magnetic field at a shock, and little is known about hot star magnetic fields aside from upper limits. Another future project, though, is to investigate the effects of conduction on wind models, under a range of reasonable assumptions.

7.5 Conclusions

The line force instability in radiatively driven winds acts to create a highly structured wind, with many shocks, separated by rarefied acceleration regions and dense shells. The shocks have a wide range of amplitudes, and therefore they heat wind material to a wide range of temperatures. Models of thermally emitted X-ray spectra from this heated material match the *shape* of observed spectra fairly well, both for a star with a massive, high-density wind (ζ Pup) and for later-type, main sequence stars with lower-density winds (μ Col and τ Sco).

If no large perturbations are put into the model, shocks that result from the line force instability tend to heat an approximately constant, and small, fraction of wind material to X-ray emitting temperatures.

Since more luminous stars have much more massive winds, this means that the model X-ray luminosity L_{x} for an early type star such as ζ Pup can easily match or exceed the observed L_{x}; in fact, model spectra are typically well above the observed spectrum. The approximation used to calculate the spectrum tends to overestimate L_{x}, and the model is probably consistent with the observation. For later type (and lower luminosity class) O stars, the rapid decrease in mass loss rate is partially offset by a smaller loss to wind attenuation, so that the ratio $L_{\rm x}/L_{\rm bol} \simeq 10^{-6.46}$ remains approximately constant throughout this range.

But beginning with late O main sequence stars, the wind is optically thin above most shocks over an increasing part of the X-ray energy range, so most of the X-rays can escape, and further decreases in wind column density no longer help to compensate for the decrease in the amount of heated material. For these stars, the small fraction of wind material heated strongly by instability-driven shocks is not enough to match the observed X-ray fluxes. In these stars, the emission measure of hot material inferred from observations is a substantial fraction—up to 100% of, and in some cases more than—the total wind emission measure. By itself, the line force instability cannot heat this much of the wind; as a result, model X-ray fluxes are lower than observed by a factor of 10–100.

To reproduce the observed spectrum of μ Col, a star with an X-ray spectrum typical of stars of this type, requires rather large ($\sim$ 25%) perturbations in the density at the base of the wind. The unusually high X-ray flux of τ Sco can result from instability-generated shocks only if a fast wind overtakes a slower one, so that a strong forward shock propagates through the wind and heats a large amount of wind material.

The model spectra vary with much larger amplitudes than observed. However, much of this may be due to the techniques used to calculate the spectra, so that it is not yet clear whether this represents a true disagreement between observations and the underlying models.

REFERENCES

Abbott, D. C. 1978, ApJ, 225, 893

Abbott, D. C. 1980, ApJ, 242, 1183

Abbott, D. C. 1982a, ApJ, 259, 282

Abbott, D. C. 1982b, ApJ, 263, 723

Abbott, D. C., Telesco, C. M., and Wolff, S. C. 1984, ApJ, 279, 225

Baade, D., and Lucy, L. B. 1987, A&A, 178, 213

Bieging, J. H., Abbott, D. C., and Churchwell, E. B. 1989, ApJ, 340, 518

Blondin, J. M. 1992, *VH-1: An Incomplete User's Guide*

Carlberg, R. G. 1980, ApJ, 241, 1131

Cassinelli, J. P. 1979, ARA&A, 17, 275

Cassinelli, J. P., Cohen, D. H., MacFarlane, J. J., Sanders, W. T., and Welsh, B.Y. 1994, ApJ, 421, 705 (CCMSW)

Cassinelli, J. P., Hartmann, L., Sanders, W. T., Dupree, A. K., and Myers, R. V. 1983, ApJ, 268, 205

Cassinelli, J. P., and Olson, G. L. 1979, ApJ, 229, 304

Cassinelli, J. P., and Swank, J. H. 1983, ApJ, 271, 681

Cassinelli, J. P., Waldron, W. L., Sanders, W. T., Harnden, F. R., Rosner, R., and Vaiana, G. S. 1981, ApJ, 250, 677

Castor, J. I. 1974a, ApJ, 189, 273

Castor, J. I. 1974b, MNRAS, 169, 279

Castor, J. I. 1993, in *Massive Stars: Their Lives in the Interstellar Medium*, ed. J. P. Cassinelli and E. B. Churchwell (ASP Conference Series, Vol. 35), p. 297

Castor, J. I. 1991, in *Stellar Atmospheres: Beyond Classical Models*, ed. L. Crivella, I. Hubeny and D. G. Hummer (Kluwer, Dordrecht), p. 221

Castor, J. I., Abbott, D. C., and Klein, R. I. 1975, ApJ, 195, 157 (CAK)

Castor, J. I., and Lamers, H. J. G. L. M. 1979, ApJS, 39, 481

Castor, J. I., and Simon, T. 1983, ApJ, 265, 304

Chen, W., and White, R. L. 1991, ApJ, 366, 512

Chevalier, R. A., and Imamura, J. N. 1982, ApJ, 261, 543

Chlebowski, T., Harnden, F. R., Jr., and Sciortino, S. 1989, ApJ, 341, 427

Cohen, D. H., MacFarlane, J. J., Cooper, R. G., Sanders, W. T., Cassinelli, J. P., Drew, J. E., Vallerga, J. V., and Welsh, B. Y. 1993, BAAS, 25, 1476

Collela, P., and Woodward, P. R. 1984, JCP, 54, 174

Collura, A., Sciortino, S., Serio, S., Vaiana, G. S., Harnden, F. R., Jr., and Rosner, R. 1989, ApJ, 338, 296

Corcoran, M. F., Swank, J. H., Serlemitsos, P. J., Boldt, E., Petre, R., Marshall, F. E., Jahoda, K., Mushotzky, R., Szymkowiak, A., Arnaud, K., Weaver, K., and Holt, S. S. 1993, ApJ, 412, 792

Courant, R., and Friedrichs, K. O. 1948, *Supersonic Flow and Shock Waves* (Interscience, New York; reprinted 1976 by Springer-Verlag, New York)

Cox, D. P., and Raymond, J. C. 1985, ApJ, 298, 651

Drew, J. 1989, ApJS, 71, 267

Feldmeier, A. 1993, Ph. D. Dissertation, University of Munich

Feldmeier, A. 1994, in *Instability and Variability in Hot Star Winds*, ed. A. F. J. Moffat, S. P. Owocki, N. St.-Louis, and A. W. Fullerton (Kluwer, Dordrecht), in press

Friend, D. B., and Abbott, D. C. 1986, ApJ, 311, 701

Friend, D. B., and MacGregor, K. B. 1984, ApJ, 282, 591

Gaetz, T. J., Edgar, R. J., and Chevalier, R. A. 1988, ApJ, 329, 927

Godunov, S. K. 1959, *Matematicheskii Sbornik*, 47, 271

Grillo, F., Sciortino, S., Micela, G., Vaiana, G. S., Harnden, F. R., Jr. 1992, ApJS, 81, 795

Groenewegen, M. A. T., and Lamers, H. J. G. L. M. 1991, A&A, 243, 429

Hearn, A. G. 1975, A&A, 40, 355

Harnden, F. R., Jr., Branduardi, G., Elvis, M., Gorenstein, P., Grindlay, J., Pye, J. P., Rosner, R., Topka, K., and Vaiana, G. S. 1979, ApJ, 234, L51

Hedstrom, G. W. 1979, JCP, 30, 222

Hillier, D. J., Kudritzki, R. P., Pauldrach, A. W., Baade, D., Cassinelli, J. P., Puls, J., and Schmitt, J. H. M. M. 1993, A&A, 276, 117

Howarth, I. D., and Prinja, R. K. 1989, ApJS, 69, 527

Hundhausen, A. J., and Gentry, R. A. 1969, JGR, 74, 6229

Krolik, J. H., and Raymond, J. C. 1985, ApJ, 298, 660

Kudritzki, R. P., and Hummer, D. G. 1990, ARA&A, 28, 303

Lamers, H. J. G. L. M., Gathier, R., and Snow, T. P. 1982, ApJ, 258, 186

Lamers, H. J. G. L. M., and Morton, D. C. 1976, ApJS, 32, 715

Lamers, H. J. G. L. M., and Rogerson, J. B. 1978, A&A, 66, 417

Lamers, H. J. G. L. M., and Snow, T. P. 1978, ApJ, 219, 504

Langer, S. H., Chanmujam, G., and Shaviv, G. 1981, ApJ, 245, L23

Lucy, L. B. 1971, ApJ, 163, 95

Lucy, L. B. 1982a, ApJ, 255, 278

Lucy, L. B. 1982b, ApJ, 255, 286

Lucy, L. B. 1983, ApJ, 274, 372

Lucy, L. B. 1984, ApJ, 284, 351

Lucy, L. B., and Solomon, P. M. 1970, ApJ, 159, 879

Lucy, L. B., and White, R. L. 1980, ApJ, 241, 300

MacFarlane, J. J., and Cassinelli, J. P. 1989, ApJ, 347, 1090

MacFarlane, J. J., Waldron, W. L., Corcoran, M. F., Wolff, M. J., Wang, P., and Cassinelli, J. P. 1993, ApJ, 419, 813

MacGregor, K. B., Hartmann, L., and Raymond, J. 1979, ApJ, 231, 514

Mihalas, D. 1978, *Stellar Atmospheres*, second edition (Freeman, San Francisco)

Miller, W. W., III, and Cox, D. P. 1993, ApJ, 417, 579

Morrison, R., and McCammon, D. 1983, ApJ, 270, 119

Morton, D. C. 1967, ApJ, 147, 1017

Mullan, D. J. 1984, ApJ, 283, 303

Mullan, D. J. 1986, A&A, 165, 157

Nordsieck, K. H., Cassinelli, J. P., and Anderson, C. M. 1981, ApJ, 248, 678

Owocki, S. P. 1991, in *Stellar Atmospheres: Beyond Classical Models*, ed. L. Crivella, I. Hubeny, and D. G. Hummer (Kluwer, Dordrecht), p. 235

Owocki, S. P. 1992, in *The Atmospheres of Early-Type Stars*, ed. C. S. Jeffery and U. Heber (Springer, Berlin), p. 393

Owocki, S. P. 1994, in preparation

Owocki, S. P., Castor, J. I., and Rybicki, G. B. 1988, ApJ, 335, 914 (OCR)

Owocki, S. P., and Rybicki, G. B. 1984, ApJ, 284, 354

Owocki, S. P., and Rybicki, G. B. 1985, ApJ, 299, 265

Owocki, S. P., and Rybicki, G. B. 1986, ApJ, 309, 127

Owocki, S. P., and Rybicki, G. B. 1991, ApJ, 368, 261

Owocki, S. P., and Zank, G. P. 1991, ApJ, 368, 491

Pauldrach, A. 1987, A&A, 183, 295

Pauldrach, A., Puls, J., and Kudritzki, R. P. 1986, A&A, 164, 86

Pauldrach, A. W. A., Kudritzki, R. P., Puls, J., Butler, K., and Hunsiger, J. 1994, A&A, 283, 525

Poe, C. H., Owocki, S. P., and Castor, J. I. 1990, ApJ, 358, 199

Prinja, R. K. 1992, in *Proceedings of STScI Workshop on Nonisotropic and Variable Outflows from Stars*, ed. L. Drissen, C. Leitherer, and A. Nota (ASP Conference Series, Vol. 22), p. 167

Prinja, R. K., Barlow, M. J., and Howarth, I. D. 1990, ApJ, 361, 607

Raymond, J. C. 1988, in *Hot Thin Plasmas in Astrophysics*, ed. R. Pallivicini (Kluwer, Dordrecht), p. 3

Raymond, J. C., Cox, D. P., and Smith, B. W. 1976, ApJ, 204, 290

Raymond, J. C., and Smith, B. W. 1977, ApJS, 35, 419

Rybicki, G. B., and Lightman, A. P. 1979, *Radiative Processes in Astrophysics* (Wiley, New York), p. 44

Rybicki, G. B., Owocki, S. P., and Castor, J. I. 1990, ApJ, 349, 274

Sciortino, S., Vaiana, G. S., Harnden, F. R., Jr., Ramella, M., Morossi, C., Rosner, R., and Schmitt, J. H. H. M. 1990, ApJ, 361, 621

Seward, F. D., Forman, W. R., Giacconi, R., Griffiths, R. E., Harnden, F. R., Jr., Jones, C., and Pye, J. P. 1979, ApJ, 234, L55

Snow, T. P., Jr., and Morton, D. C. 1976, ApJS, 32, 429

Sobolev, V. V. 1960, *Moving Envelopes of Stars* (Harvard University Press, Cambridge)

Sod, G. A. 1978, JCP, 27, 1

Springmann, U. W. E., and Pauldrach, A. W. A. 1992, A&A, 262, 515

Swank, J. H. 1985, in *The Origin of Nonthermal Heating/Momentum in Hot Stars*, ed. A. B. Underhill and A. G. Michalitsionos (NASA Publ. 2358), p. 86

Waldron, W. L. 1984, ApJ, 282, 256

Waters, L. B. F. M., Marlborough, J. M., Geballe, T. R., Oosterbrock, T., and Zaal, P. 1993, A&A, 272, L9

Woodward, P. R., and Collela, P. 1984, JCP, 54, 115

Yang, H. Q., and Przekwas, A. J. 1992, JCP, 102, 139